INVESTIGATING THE BIOLOGY AND GENETIC BASIS OF STRESS ADAPTATION IN *CRYPTOCOCCUS NEOFORMANS*

by

BENJAMIN JAMES CHADWICK

(Under the Direction of Xiaorong Lin)

ABSTRACT

Cryptococcus neoformans is a ubiquitous free-living soil yeast. It is also an opportunistic pathogen that causes about 223,100 cases of cryptococcal meningitis per year, resulting in over 180,000 deaths. The success of this pathogen lies in its ability to adapt to the host physiological conditions. One major obstacle *C. neoformans* needs to overcome to be pathogenic is growth at host temperature levels (>37˚C). The transcription factor Crz1 is known to be important for thermotolerance, and its subcellular trafficking likely contributes to its function. During my graduate study, I investigated the molecular basis of Crz1's function and subcellular localization. I found that Crz1 localization dynamically responds to changes in various environmental conditions, and this is dependent on several intrinsically disordered domains within the protein. Another critical but uninvestigated difference between the natural niche of *C. neoformans* and the mammalian host is the concentration of CO_2: there is 125 times more CO_2 in the host than in the ambient air. We recently found that clinical isolates from patients are generally more tolerant to high levels of CO_2 than isolates from the environment. Much of my dissertation research was focused on determining the genetic basis of CO_2 adaptation and tolerance in *C. neoformans*. By utilizing a forward genetic screen of gene deletion mutants, QTL mapping, congenic strains, and

experimental evolution, I have concluded that: (1) regulation of thermotolerance and CO_2 tolerance is tightly linked, (2) the RAM (Regulator of *ACE2* and morphogenesis) pathway is critical for integrating multiple stress response pathways to regulate both CO_2 tolerance and thermotolerance, (3) CO_2 tolerance is a complex trait controlled by multiple genetic loci and their interactions, (4) response to increased CO_2 levels is likely regulated post-transcriptionally, and (5) CO_2-sensitive *C. neoformans* strains can become CO_2-tolerant after *in vivo* passage or *in vitro* passage through high levels of CO_2. Research to define the molecular and cellular responses induced from host stress is critical for understanding *C. neoformans* pathogenesis and for developing treatments as CO_2 also greatly affects antifungal drug efficacy.

INDEX WORDS: *Cryptococcus neoformans*, calcineurin, Crz1, stress granules, intrinsically disordered regions, genetic screen, RAM pathway, CO_2 tolerance, QTL mapping, experimental evolution, virulence factors, pathogenesis

INVESTIGATING THE BIOLOGY AND GENETIC BASIS OF STRESS ADAPTATION IN *CRYPTOCOCCUS NEOFORMANS*

by

BENJAMIN JAMES CHADWICK

BS, University of Delaware, 2018

A Dissertation Submitted to the Graduate Faculty of The University of Georgia in Partial Fulfillment of the Requirements for the Degree

DOCTOR OF PHILOSOPHY

ATHENS, GEORGIA

2023

INVESTIGATING THE BIOLOGY AND GENETIC BASIS OF STRESS ADAPTATION IN *CRYPTOCOCCUS NEOFORMANS*

by

BENJAMIN JAMES CHADWICK

Major Professor:	Xiaorong Lin
Committee:	Marin Brewer
	Katrien Devos
	Daichi Kamiyama
	Wolfgang Lukowitz

Electronic Version Approved:

Ron Walcott
Vice Provost for Graduate Education and Dean of the Graduate School
The University of Georgia
December 2023

TABLE OF CONTENTS

LIST OF TABLES

Page

LIST OF FIGURES

Page

CHAPTER 1

INTRODUCTION AND LITERATURE REVIEW ON THE USE OF CONGENIC STRAINS IN *CRYPTOCOCCUS* RESEARCH [1]

[1] Benjamin James Chadwick and Xiaorong Lin. 2020. *Pathogens.* Sep; 9(9): 750.

The *Cryptococcus* pathogenic *species complex*

Cryptococcus neoformans is an environmental fungus and a global opportunistic pathogen, responsible for over 180,000 fatalities annually [1]. This fungus enters human lungs through inhalation and can disseminate through the bloodstream when the host is immunocompromised, often due to AIDS or immune-suppressive treatments for cancer or organ transplant [2,3]. The pathogenic *C. neoformans* species complex have been differentiated based on serotypes and molecular types [4]. The major pathogenic *Cryptococcus* species were originally separated into different serotypes (A, B, C, and D, or their hybrids) based on their capsular epitopes or biochemical properties tested by diagnostic media [5,6]. Serotypes A and D correspond to *C. neoformans* var. *grubii* and *C. neoformans* var. *neoformans*, while serotypes B and C refer to *C. gattii*. Different isolates of *C. neoformans* and *C. gattii* are further divided into molecular groups, based on their DNA sequencing information. In general, serotype A isolates have been separated into three molecular types referred to as VNI, VNII, and VNB (only Botswana isolates), and serotype D has been typed as VNIV. Isolates with the molecular type VNIII are serotype AD hybrids. Molecular types VGI, VGII, VGIII, VGIV, and VGV correspond to *C. gattii* isolates (see review [4]).

Significant genetic and phenotypic diversity are reported among the groups (many referenced here [7]). This is not unexpected given that serotype A and serotype D of *C. neoformans* diverged from a common ancestor an estimated 18.5 million years ago, and serotypes B and C of *C. gattii* diverged about 9.5 million years ago based on multi-locus sequence typing [8]. *C. gattii* and *C. neoformans* were estimated to have diverged roughly 37 million years ago. In comparison, humans and chimpanzees diverged about 12.1 million years ago, and humans and gorillas diverged from each other about 15.1 million years ago based on whole genome

sequencing data [9]. Functional divergence of genetic networks between serotypes A and D of *C. neoformans* is not uncommon, as demonstrated in the PKA (protein kinase A) and HOG (high osmolarity glycerol) pathways, the two major stress-sensing pathways [10,11]. Even within the same serotype, great genetic heterogeneity exists. For instance, VNI and VNII of serotype A were estimated to have diverged from each other about 5 million years ago, and different *C. gattii* VG molecular types about 10 million years from each other [12].

The first use of congenic pairs in *Cryptococcus* research

Cryptococcus species are ubiquitous basidiomycetes with a bipolar mating system, defined as either mating type (*MAT*) **a** or α [13]. Unlike *S. cerevisiae*, *Cryptococcus* does not have the ability to switch mating types [14]. Laboratory crosses between **a** and α isolates lead to a 1:1 segregation of the mating types in the progeny. However, in 1978, Kwon-Chung and Bennett found that the α mating type was 30-40 times more prevalent than the **a** mating type among the tested 105 environmental and 233 clinical isolates of *C. neoformans* [5]. Similar findings were later reported based on samples isolated from different locations [15-18]. This raised the question about the impact of the mating type locus on *Cryptococcus* biology and pathogenicity.

Congenic strains differing primarily at the mating type locus in multiple genetic backgrounds would be valuable tools to address such questions. Kwon-Chung and her colleagues developed the first congenic pair [19]. They used progeny of serotype D strains NIH12 and NIH433, a clinical α and an environmental **a** isolate, as the starting strains. These strains, named B-3501 and B-3502, had slightly different karyotypes based on contour-clamped homogenous electric-field (CHEF) electrophoresis. Their cross generated B-4476(**a**), which was used as the parent strain in this congenic pair construction. After 6 backcrosses to B-4476, the karyotype differences were no longer observed between progeny and parent. A total of 10 backcrosses were completed to

create the first congenic pair now known as JEC20**a** and JEC21α, with JEC20**a** as the new alias for B-4476 (Figure 1.1A). The authors found that α progeny from a cross between the congenic pair strains JEC20 and JEC21 were more virulent than **a** progeny in an intravenous infection model of murine cryptococcosis. Because these strains primarily differ in the mating type locus, this suggested that the mating type locus is linked to virulence.

The establishment of this congenic pair also led to the cloning of the mating type locus and the pheromone genes, as well as the discovery of the MAPK (mitogen-activated protein kinase) pheromone sensing and response pathway controlled by the genes encoded by the *MAT* locus [20]. Moore and Edman also showed there was only a single mating type locus in *C. neoformans* [20]. This contrasts with the existence of alternate mating type loci in the same genome as seen in *S. cerevisiae*, which allows the budding yeast to switch mating types [14]. JEC21α later became the first *Cryptococcus* strain to be whole genome sequenced and extensively used in genetic manipulations to study gene function at the molecular level in this organism [21].

Summary of congenic pairs in *Cryptococcus*

The *C. neoformans* species complex is responsible for about 99% of total cryptococcosis cases globally [4], and so it is no surprise that five of the six congenic pairs have been constructed in the *C. neoformans* background (Table 1.1). After the Vancouver Island outbreak caused by *C. gattii* starting from 1999, hundreds of *C. gattii* isolates have been discovered in Canada and the VGII type is now the most frequently reported in Northwest America [22]. The heightened virulence of the Vancouver outbreak strains motivated the construction of the first VGII background congenic pair based on the sequenced strain R265 [23]. The six current *Cryptococcus* congenic pairs are summarized in Table 1.1: JEC20**a**/JEC21α (VNIV), KN99**a**/α (VNI), KN433**a**/α (VNIV), KN3501**a**/α (VNIV), XL280**a**/α (VNIV) and AIR265**a**/α (VGII).

These congenic pairs differ widely in various phenotypes, including capsule production, melanization, filamentation, mating, or their virulence in the murine models of cryptococcosis (Table 1). Congenic pairs KN99**a**/α and AIR265**a**/α are among the most aggressive strains as they kill mice around 3-4 weeks following intranasal infections or about one week following intravenous infection. Inoculum only has modest effects on the median days of survival of infected animals. XL280**a**/α are modestly lower in virulence than KN99**a**/α and AIR265**a**/α strains, but this pair are the most virulent among the serotype D congenic pairs including JEC20**a**/21α, KN3501**a**/α, and KN433**a**/α. The intranasal mouse infection model using JEC20**a**/21α requires high inoculum (e.g. 1x10^7) and months for mortality studies, and even then some mice can survive the infection [24,25]. Thus, the intravenous infection model that bypasses the initial lung infection is often preferred when JEC20**a**/21α or other serotype D congenic pairs such as KN3501**a**/α and KN433**a**/α are used. XL280**a**/α are far more virulent than these related serotype D pairs, and XL280**a**/α are used in both the intranasal and intravenous infection models [26]. Although all the serotype D congenic pairs are excellent maters, XL280**a**/α exhibit the most robust self-filamentation *in vitro* (monokaryotic fruiting or unisexual reproduction), which makes this pair an excellent model for morphogenesis investigation [27]. In contrast, JEC20**a**/21α are the better choice for investigation of bisexual mating due to minimal interference from unisexual reproduction.

There are still 7 molecular types with no corresponding congenic pair. Construction of congenic pairs in these molecular types would provide a platform for functional comparative studies of this species complex to advance our understanding of their biology and pathogenicity.

The impact of mating type on virulence and tissue tropism

Because of the dominance of the α mating type in 99% of cryptococcal natural isolates found in the environment and clinic, a major question of the field is whether the mating type α enhances fitness and virulence. Kwon-Chung and her colleagues took advantage of the first congenic pair to probe this question. They found that α and **a** progeny from a cross between JEC20**a** and JEC21α were comparable in growth *in vitro*, but α progeny were more virulent than their **a** siblings in the intravenous infection murine model [19]. Nielsen found that KN433α was modestly more virulent than its congenic partner KN433**a**, while KN3501α was comparable in virulence to its congenic partner KN3501**a** [28]. These congenic pairs are all related serotype D strains (Figure 1.1), with the α mating type locus originating from NIH12 and the **a** mating type locus originating from NIH433. The difference in virulence between **a** and α in these congenic strains is therefore likely due to the difference in the interaction between the mating type locus and their different genetic backgrounds.

The construction of serotype A congenic strains was not initiated until a decade later due to the lack of serotype A **a** isolates. Although it had been long suspected that serotype A **a** isolates exist given the presence of **a**ADα hybrid isolates, the first serotype A **a** strain, 125.91, was not discovered until 2000 [29]. Fortunately, this **a** strain, isolated from an AIDS patient in Tanzania, was able to mate with another serotype A clinical α strain 8-1 [30]. The progeny of this cross, KNA14**a**, was able to mate robustly with the *crg1*Δ (cryptococcal regulator of G-protein signaling) mutant of the reference serotype A strain H99α. The deletion of *CRG1* rendered H99α hypersensitive to pheromone. The **a** progeny of this cross was then able to mate with the wildtype H99α strain, even after crossing out the *crg1*Δ mutation (Figure 1.1C). Backcrosses with H99α eventually yielded the congenic pair KN99**a**/α. Similar methods could be useful to

generate congenic pairs in strains that mate poorly. The availability of the genetically diverse and highly virulent congenic pairs KN99**a**/α (serotype A), XL280**a**/α (serotype D), and AIR265**a**/α (serotype B) allowed further comparison of overall virulence between the **a** and α strains [23,27,30]. These studies found no difference in virulence between **a** and cognate α strains.

The **a** and α coinfection has been used to directly compare the virulence of congenic strains in murine models. In the study performed by Nielsen *et al.*, the mixture of KN99**a** and KN99α cells was used to infect mice intranasally [31]. To easily distinguish **a** from α cells, the strains carried drug markers inserted into the mating type locus at intergenic regions. They concluded that a higher proportion of KN99**a** cells colonize the spleen in a shorter time frame, while KN99α cells colonize the brain more rapidly. One caveat of this study is that the drug marker used was inserted in the *MAT*α locus at a different region compared to the insertion in the *MAT***a** locus due to the idiomorphic nature of the two mating types. To avoid potential complications of using mating-type locus marked strains, Zhai *et al*. used unmarked wildtype XL280 congenic strains in their coinfection experiments [27]. Given that dissemination from lungs to the brain varies widely among individual mice in the intranasal infection model, they infected one group of mice with the **a**-α mixture intranasally and another group intravenously. They determined the mating type of cryptococcal cells recovered from infected mice through mating with reference strains. At the termination of the intranasal infection group, a significantly higher proportion of α cells were recovered from the lungs, and a higher proportion of **a** cells were recovered from the brain. In contrast, no significant differences were found in colonization of the spleen or kidney. The data from this experiment indicates that the α cells of XL280 may preferentially colonize the lungs. In the intravenous coinfection model, a slightly higher proportion of XL280α cells were recovered from the brain and kidney than XL280**a** cells, and no

clear difference was observed in colonization of the spleen when mice were terminated at day 5. A similar coinfection study performed using the AIR265 congenic strains in both intravenous and intranasal models, however, revealed no relationship between the mating type and virulence or tissue tropism [23].

Taken together, subtle differences in tissue tropism may exist in the XL280**a**/α and KN99**a**/α congenic pairs. Because there is no clear correlation between mating type and virulence, it is most likely that the genetic background of individual strains has a significant influence on overall virulence and tissue tropism. The most clear evidence supporting this is the drastic difference in virulence between XL280**a**/α and JEC20**a**/21α, which are sister strains sharing identical mating type loci (Figure 1.1A-B)[27].

The impact of mating type on morphogenesis

While *C. neoformans* is known to undergo **a**-α bisexual reproduction which leads to production of recombinant basidiospores [13], single isolates can undergo monokaryotic fruiting (or unisexual reproduction) without the participation of the other mating type and yield spores of only one mating type [32]. Monokaryotic fruiting has primarily been reported in serotype D strains, but it also occurs in other serotypes [33-35]. Given the sharply skewed distribution of mating types, it has been proposed that a difference in the ability of **a** and α to produce spores during monokaryotic fruiting might have given rise to the dominance of the α mating type. However, monokaryotic fruiting has been observed in isolates of either the **a** or α mating type [36]. Interestingly, among the congenic pairs, α strains showed enhanced ability to undergo self-fruiting compared to the cognate **a** strains, which supports the hypothesis. For instance, JEC21α has the ability to undergo monokaryotic fruiting while its congenic partner JEC20**a** does not [37]. The α mating type of the self-filamentous congenic pair XL280, as well as α progeny of the

different backcross generations, showed more robust self-filamentation than the **a** congenic strain and **a** progeny [27]. XL280**a** and XL280α are otherwise phenotypically similar, including virulence in the mouse model, capsule production, melanin synthesis, and resistance to hydrogen peroxide and sodium chloride [27].

Further evidence supporting the contribution of the mating type locus to self-filamentation comes from a QTL (quantitative trait loci) mapping study in 2006 [38]. In this study, Lin *et al.* isolated an inbred population of 94 serotype D progeny and genotyped them using restriction fragment length polymorphism markers (RFLP). Analysis of the sequence polymorphisms across the genome and the quantitative differences in self-filamentation of these progeny led to the identification of two significant QTLs that highly influence the hyphal length during monokaryotic fruiting. Not surprisingly, the most significant QTL lies in the mating type locus, revealing a positive association of the α mating type with increased hyphal growth. Another significant QTL identified resides in chromosome 9, supporting that self-filamentation is controlled by both genes inside and outside of the mating type locus. Due to the limited number of markers and progeny used, the genes with allelic difference involved in hyphal elongation were not defined in this study. Now with advanced and cheaper genome sequencing technology, higher resolution mapping with a larger population size could help identify the quantitative trait genes located outside of the mating type locus. A bulk segregant analysis strategy that sequences a pool of the filamentous progeny to compare with a pool of the non-filamentous progeny could also be applied to determine the alleles that control self-filamentation. Thus far, the mechanistic difference in monokaryotic fruiting between the **a** and α mating type, along with how the mating type locus interacts with other loci in the genome, has yet to be determined. One potential regulator of self-filamentation encoded in the mating type locus is the

transcription factor Ste12. In the congenic pair JEC20**a**/21α, the *ste12***a**Δ or the *ste12*αΔ mutant can undergo bisexual mating but not monokaryotic fruiting, and overexpression of either *STE12***a** or *STE12*α induces self-filamentation [39,40]. In comparison, deletion of the *STE12* gene in hyper filamentous strain XL280α reduces self-filamentation, but does not abolish it [41]. Because XL280α and JEC21α both share the same mating type locus, factors outside of the mating type locus must be influencing the ability to self-filament, echoing the findings from the QTL study.

Determining the genetic factors contributing to uniparental mitochondrial inheritance

Unlike Mendelian segregation of the nuclear genome where meiotic progeny inherits 50% from each parent, mitochondrial DNA (mtDNA) inheritance during sexual reproduction in *C. neoformans* is uniparental, with most progeny receiving mtDNA from only the **a** parent [42]. Uniparental mitochondrial inheritance was first revealed in inter-varietal crosses between the serotype D JEC20**a** and serotype A α strains because of the ease to distinguish mitochondrial DNA of different serotypes based on sequence polymorphisms. The congenic pairs JEC20**a**/21α, KN3501**a**/α, KN433**a**/α, and XL280**a**/α all should have identical mtDNA inherited from NIH433**a** (Figure 1.1). Zhun and Xu later made congenic JEC20**a** and JEC21α strains with different mtDNA, by outcrossing them to strains with different mtDNA and isolating blastospores [43]. The progeny of these strains also showed uniparental inheritance of mtDNA from the **a** parent strain, indicating that uniparental mitochondrial inheritance is not an artifact of inter-varietal mating. The investigations into the molecular control of mitochondrial inheritance have revealed the importance of cooperation between genes located outside of the mating type locus and those inside: The transcription factor Mat2 and regulator Crg1 encoded by genes outside of the mating type locus control multiple genes residing within the mating type locus. The products of these mating type genes are involved in the pheromone-response pathway that

drives the formation of the zygote, and the formation of the Sxi1α-Sxi2**a** homeodomain complex that dictates dikaryotic hyphal growth during bisexual mating [44-46]. The cooperation between Mat2 and the Sxi1α-Sxi2**a** complex enables strict inheritance of the **a** mitochondria during bisexual reproduction [47]. Uniparental mitochondrial inheritance is demonstrated in crosses of *C. neoformans* isolates and of the *Cryptococcus gattii* VGII congenic pair [23]. However, increased leakage of α mtDNA inheritance was reported in crosses between natural *Cryptococcus gattii* isolates, many of the VGIII lineage [48]. It would be useful to compare mtDNA inheritance patterns among congenic strains constructed in other genetic backgrounds. So far, the evidence suggests that mitochondrial DNA inheritance is controlled by multiple genetic loci, and that difference in their interaction with the mating type locus could be an important source of variation. Detailed discussion on this topic can be found in a separate chapter by Matha and Lin in this special issue [49].

Limitations and improvement of congenic pair construction

By design, congenic pairs cannot be 100% genetically identical even though they show the same genotype and karyotype based on limited RFLP markers and CHEF electrophoresis. After 10 backcrosses, the progeny in theory are 99.95% identical to the parental backcrossing strain excluding the mating type locus. With a genome size of about 20 Mb, that means a possibility of total regions of the size of 10,000bp with polymorphisms between the congenic pairs, which could cause phenotypic variations. The observation that progeny of JEC20**a** and JEC21α differed in growth at high temperature, melanization, and capsule production with no clear connection to mating type [50] likely reflects the existence of genetic differences present in other loci. Consistently, comparative analyses of the whole genome sequences of strains JEC20**a** and JEC21α revealed two SNP dense regions other than the mating type locus [50]. One way to

prevent misinterpretation of phenotypic differences between the congenic pairs is to include multiple progeny of the congenic pair for phenotypic analyses. Sequencing the genomes of multiple isolates from the 10th backcross could also help pick progeny that are most genetically similar to the backcrossing parent or interpret the observed phenotypic variations. Genome sequencing should become a standard practice to ensure genetic similarity of the congenic pair. The technical challenge of microdissection of the meiotic basidiospores could cause some issues during congenic pair construction in *Cryptococcus*, particularly in strains where mating is poor. Improving the mating efficiency of *Cryptococcus* through genetic mutations of the mating pathway in the backcrosses could be implemented as in the construction of the congenic pair KN99**a**/α [30]. As long as the mutation is not present in both strains used in a cross, the mutation can be crossed out and will not be present in the final congenic pair. Further study of filamentation and sporulation pathways, therefore, may provide useful tools for this practical purpose.

Another complicating factor in constructing congenic pairs in *Cryptococcus* is the heterogenous nature of mating. Only a small subset of the population is engaged in sexual reproduction and the vast majority of cells amplify mitotically. The meiotic basidiospores are often near mitotically generated yeast cells. Non-recombinant small yeast cells could be mistaken for meiotic progeny either by microdissection or differential centrifugation. If a strain derived from mitotic division from the parents were selected as a progeny and used for the next backcrossing, it would effectively reduce the real number of generations of backcrossing and lead to a higher than expected level of genetic difference among the final congenic strains. Advancement in separating meiotic spores from yeasts would be useful for the construction of congenic pairs, as well as for other applications using any laboratory crosses.

Conclusion

Congenic pairs are vital tools in genetics research, and they boost the use of *Cryptococcus* as a model organism for basic eukaryotic biology and microbial pathogenesis studies. The current congenic pairs facilitate genetic linkage analyses and the creation of mutants. Their application to *Cryptococcus* research has allowed for the elaboration of the components of the mating type locus and its roles in different aspects of pathogenesis. Mechanisms behind how the mating type locus influences virulence, neurotropism, filamentation, and uniparental inheritance of mtDNA remain to be delineated, and congenic strains may play a crucial role in their elucidation in the future. Construction of congenic pairs in molecular types besides VNI, VNIV, and VGII will help embrace the genetic diversity represented in this species complex and further the investigation of the fundamental biology and pathogenesis in *Cryptococcus*.

Funding Statement

This work was supported by National Institutes of Health (http://www.niaid.nih.gov) (R01AI147541 to XL) and startup fund (to XL) from the University of Georgia. The funders had no role in study design, data collection, and interpretation, or the decision to submit the work for publication.

Acknowledgements

We thank all Lin lab members for their helpful suggestions.

References

1. Rajasingham, R. *et al.* Global burden of disease of HIV-associated cryptococcal meningitis: an updated analysis. *The Lancet Infectious Diseases* **17**, 873-881 (2017).
2. Casadevall, A. & Perfect, J.R. *Cryptococcus Neoformans*, (ASM Press, 1998).
3. Zhao, Y., Lin, J., Fan, Y. & Lin, X. Life cycle of *Cryptococcus neoformans*. *Annual Review of Microbiology* **73**, null (2019).

4. Cogliati, M. Global molecular epidemiology of *Cryptococcus neoformans* and *Cryptococcus gattii*: an atlas of the molecular types. *Scientifica* **2013**, 675213-675213 (2013).
5. Bennett, J.E., Kwon-Chung, K.J. & Theodore, T.S. Biochemical differences between serotypes of Cryptococcus neoformans. *Sabouraudia* **16**, 167-74 (1978).
6. Kwon-Chung, K.J., Polacheck, I. & Bennett, J.E. Improved diagnostic medium for separation of *Cryptococcus neoformans* var. *neoformans* (serotypes A and D) and *Cryptococcus neoformans* var. *gattii* (serotypes B and C). *Journal of clinical microbiology* **15**, 535-537 (1982).
7. Hagen, F. *et al.* Recognition of seven species in the *Cryptococcus gattii*/*Cryptococcus neoformans* species complex. *Fungal Genet Biol* **78**, 16-48 (2015).
8. Xu, J., Vilgalys, R. & Mitchell, T.G. Multiple gene genealogies reveal recent dispersion and hybridization in the human pathogenic fungus Cryptococcus neoformans. *Molecular Ecology* **9**, 1471-1481 (2000).
9. Moorjani, P., Amorim, C.E.G., Arndt, P.F. & Przeworski, M. Variation in the molecular clock of primates. *Proceedings of the National Academy of Sciences* **113**, 10607-10612 (2016).
10. Hicks, J.K. & Heitman, J. Divergence of protein kinase A catalytic subunits in Cryptococcus neoformans and Cryptococcus gattii illustrates evolutionary reconfiguration of a signaling cascade. *Eukaryot Cell* **6**, 413-20 (2007).
11. Bahn, Y.-S., Kojima, K., Cox, G.M. & Heitman, J. Specialization of the HOG Pathway and Its Impact on Differentiation and Virulence of Cryptococcus neoformans. *Molecular Biology of the Cell* **16**, 2285-2300 (2005).
12. Ngamskulrungroj, P. *et al.* Genetic diversity of the *Cryptococcus* species complex suggests that *Cryptococcus* gattii deserves to have varieties. *PLOS ONE* **4**, e5862 (2009).
13. Kwon-Chung, K.J. Morphogenesis of Filobasidiella neoformans, the sexual state of Cryptococcus neoformans. *Mycologia* **68**, 821-33 (1976).
14. Herskowitz, I. Life cycle of the budding yeast Saccharomyces cerevisiae. *Microbiological reviews* **52**, 536-553 (1988).
15. Levitz, S.M. Cryptococcus neoformans by Casadevall, Arturo & Perfect, John R. (1998) ASM Press, Washington, DC. Hardcover. 542 pp. $89.95. (ASM Member price: $79.95). *Medical Mycology* **37**, 371-371 (1999).
16. Litvintseva, A.P., Kestenbaum, L., Vilgalys, R. & Mitchell, T.G. Comparative analysis of environmental and clinical populations of Cryptococcus neoformans. *Journal of clinical microbiology* **43**, 556-564 (2005).
17. Lin, X., Patel, S., Litvintseva, A.P., Floyd, A., Mitchell, T.G. & Heitman, J. Diploids in the Cryptococcus neoformans serotype A population homozygous for the alpha mating type originate via unisexual mating. *PLoS pathogens* **5**, e1000283-e1000283 (2009).
18. Cogliati, M. *et al.* Environmental distribution of Cryptococcus neoformans and C. gattii around the Mediterranean basin. *FEMS yeast research* **16**, fow045 (2016).
19. Kwon-Chung, K.J., Edman, J.C. & Wickes, B.L. Genetic association of mating types and virulence in *Cryptococcus neoformans*. *Infection and immunity* **60**, 602-605 (1992).
20. Moore, T.D. & Edman, J.C. The alpha-mating type locus of Cryptococcus neoformans contains a peptide pheromone gene. *Mol Cell Biol* **13**, 1962-70 (1993).
21. Loftus, B.J. *et al.* The genome of the basidiomycetous yeast and human pathogen Cryptococcus neoformans. *Science (New York, N.Y.)* **307**, 1321-1324 (2005).

22. Hoang, L.M.N., Maguire, J.A., Doyle, P., Fyfe, M. & Roscoe, D.L. *Cryptococcus neoformans* infections at Vancouver Hospital and Health Sciences Centre (1997–2002): epidemiology, microbiology and histopathology. *Journal of Medical Microbiology* **53**, 935-940 (2004).
23. Zhu, P., Zhai, B., Lin, X. & Idnurm, A. Congenic strains for genetic analysis of virulence traits in Cryptococcus gattii. *Infection and immunity* **81**, 2616-2625 (2013).
24. Barchiesi, F. *et al.* Comparative analysis of pathogenicity of Cryptococcus neoformans serotypes A, D and AD in murine cryptococcosis. *J Infect* **51**, 10-6 (2005).
25. Lin, X. *et al.* alpha AD alpha hybrids of *Cryptococcus neoformans*: evidence of same-sex mating in nature and hybrid fitness. *PLoS Genet* **3**, 1975-90 (2007).
26. Feretzaki, M., Hardison, S.E., Wormley, F.L., Jr. & Heitman, J. Cryptococcus neoformans hyperfilamentous strain is hypervirulent in a murine model of cryptococcal meningoencephalitis. *PloS one* **9**, e104432-e104432 (2014).
27. Zhai, B., Zhu, P., Foyle, D., Upadhyay, S., Idnurm, A. & Lin, X. Congenic strains of the filamentous form of Cryptococcus neoformans for studies of fungal morphogenesis and virulence. *Infection and immunity* **81**, 2626-2637 (2013).
28. Nielsen, K. *et al.* Interaction between genetic background and the mating-type locus in *Cryptococcus neoformans* virulence potential. *Genetics* **171**, 975-983 (2005).
29. Lengeler, K.B., Wang, P., Cox, G.M., Perfect, J.R. & Heitman, J. Identification of the MATa mating-type locus of *Cryptococcus neoformans* reveals a serotype A MATa strain thought to have been extinct. *Proceedings of the National Academy of Sciences* **97**, 14455-14460 (2000).
30. Nielsen, K., Cox, G.M., Wang, P., Toffaletti, D.L., Perfect, J.R. & Heitman, J. Sexual Cycle of Cryptococcus neoformans var. grubii and Virulence of Congenic a and α Isolates. *Infection and Immunity* **71**, 4831-4841 (2003).
31. Nielsen, K. *et al.* Cryptococcus neoformans {alpha} strains preferentially disseminate to the central nervous system during coinfection. *Infection and immunity* **73**, 4922-4933 (2005).
32. Lin, X., Hull, C.M. & Heitman, J. Sexual reproduction between partners of the same mating type in Cryptococcus neoformans. *Nature* **434**, 1017 (2005).
33. Fu, J., Morris, I.R. & Wickes, B.L. The Production of Monokaryotic Hyphae by Cryptococcus neoformans Can Be Induced by High Temperature Arrest of the Cell Cycle and Is Independent of Same-Sex Mating. *PLOS Pathogens* **9**, e1003335 (2013).
34. Ren, P., Chaturvedi, V. & Chaturvedi, S. Carbon Dioxide is a Powerful Inducer of Monokaryotic Hyphae and Spore Development in Cryptococcus gattii and Carbonic Anhydrase Activity is Dispensable in This Dimorphic Transition. *PLOS ONE* **9**, e113147 (2014).
35. Xu, X. *et al.* Glucosamine stimulates pheromone-independent dimorphic transition in *Cryptococcus neoformans* by promoting Crz1 nuclear translocation. *PLOS Genetics* **13**, e1006982 (2017).
36. Tscharke, R.L., Lazera, M., Chang, Y.C., Wickes, B.L. & Kwon-Chung, K.J. Haploid fruiting in *Cryptococcus neoformans* is not mating type alpha-specific. *Fungal Genet Biol* **39**, 230-7 (2003).
37. Wickes, B.L., Mayorga, M.E., Edman, U. & Edman, J.C. Dimorphism and haploid fruiting in Cryptococcus neoformans: association with the alpha-mating type. *Proceedings of the National Academy of Sciences* **93**, 7327-7331 (1996).

38. Lin, X., Huang, J.C., Mitchell, T.G. & Heitman, J. Virulence Attributes and Hyphal Growth of C. neoformans Are Quantitative Traits and the MATα Allele Enhances Filamentation. *PLOS Genetics* **2**, e187 (2006).
39. Chang, Y.C., Penoyer, L.A. & Kwon-Chung, K.J. The second STE12 homologue of Cryptococcus neoformans is MATa-specific and plays an important role in virulence. *Proceedings of the National Academy of Sciences of the United States of America* **98**, 3258-3263 (2001).
40. Wickes, B.L., Edman, U. & Edman, J.C. The Cryptococcus neoformans STE12α gene: a putative Saccharomyces cerevisiae STE12 homologue that is mating type specific. *Molecular Microbiology* **26**, 951-960 (1997).
41. Lin, X., Jackson, J.C., Feretzaki, M., Xue, C. & Heitman, J. Transcription Factors Mat2 and Znf2 Operate Cellular Circuits Orchestrating Opposite- and Same-Sex Mating in Cryptococcus neoformans. *PLOS Genetics* **6**, e1000953 (2010).
42. Xu, J. *et al.* Uniparental Mitochondrial Transmission in Sexual Crosses in Cryptococcus neoformans. *Current Microbiology* **40**, 269-273 (2000).
43. Yan, Z. & Xu, J. Mitochondria are inherited from the MATa parent in crosses of the basidiomycete fungus *Cryptococcus neoformans*. *Genetics* **163**, 1315-1325 (2003).
44. Yan, Z., Hull, C.M., Sun, S., Heitman, J. & Xu, J. The mating type-specific homeodomain genes SXI1 alpha and SXI2a coordinately control uniparental mitochondrial inheritance in *Cryptococcus neoformans*. *Curr Genet* **51**, 187-95 (2007).
45. Gyawali, R. & Lin, X. Prezygotic and Postzygotic Control of Uniparental Mitochondrial DNA Inheritance in Cryptococcus neoformans. *mBio* **4**, e00112-13 (2013).
46. Sun, S., Fu, C., Ianiri, G. & Heitman, J. The Pheromone and Pheromone Receptor Mating-Type Locus Is Involved in Controlling Uniparental Mitochondrial Inheritance in Cryptococcus. *Genetics* **214**, 703-717 (2020).
47. Gyawali, R. & Lin, X. Mechanisms of uniparental mitochondrial DNA inheritance in *Cryptococcus neoformans*. *Mycobiology* **39**, 235-242 (2011).
48. Wang, Z., Wilson, A. & Xu, J. Mitochondrial DNA inheritance in the human fungal pathogen Cryptococcus gattii. *Fungal Genetics and Biology* **75**, 1-10 (2015).
49. Matha AR, L.X. Current perspectives on uniparental mitochondrial inheritance in Cryptococcus neoformans. *Pathogens*,
(2020).
50. Hua, W., Vogan, A. & Xu, J. Genotypic and phenotypic analyses of two "isogenic" strains of the human fungal pathogen *Cryptococcus neoformans* var. *neoformans*. *Mycopathologia* **184**, 195-212 (2019).

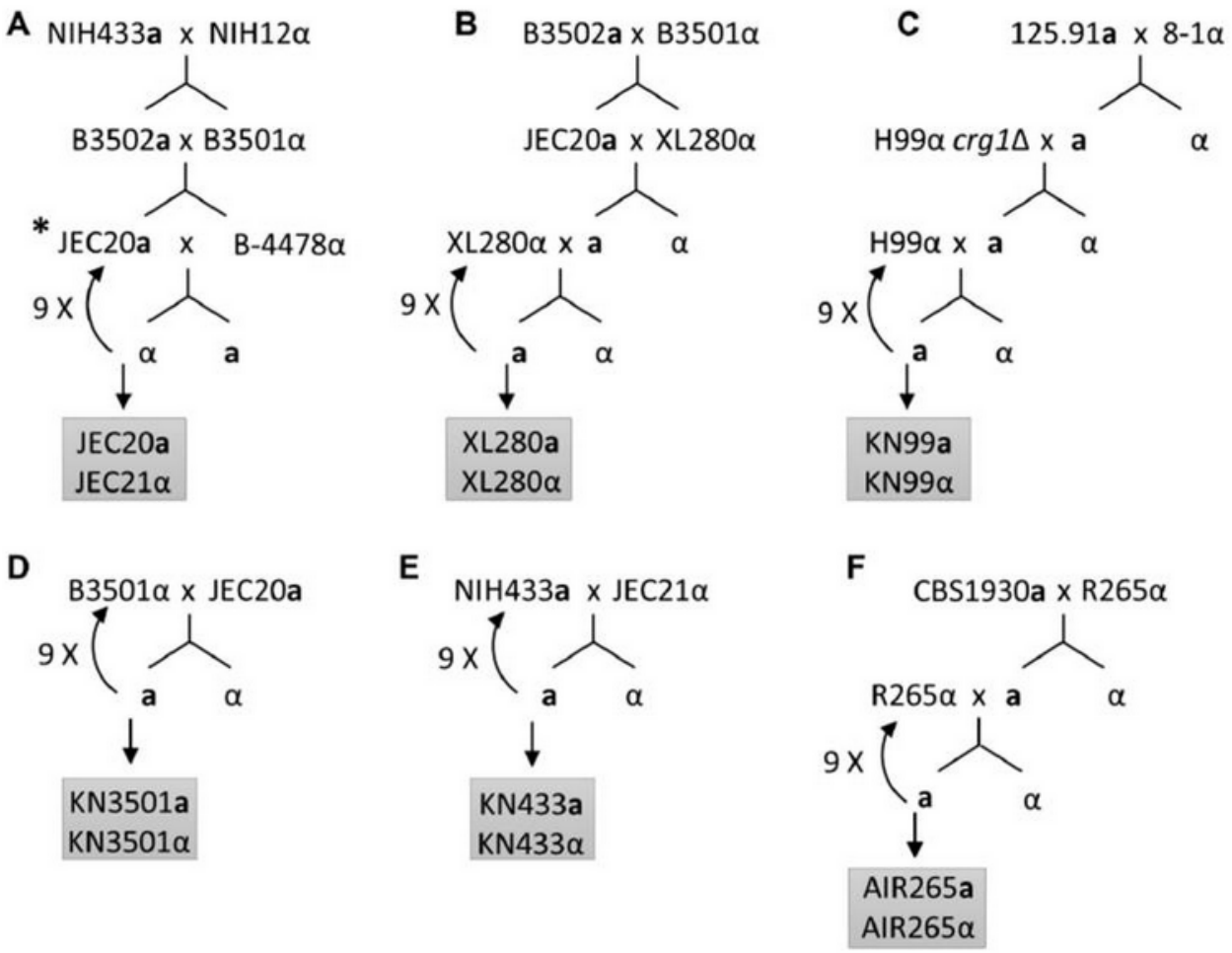

Figure 1.1. Schemes of current Cryptococcus congenic pairs. (**A**) NIH433**a** and NIH12α were crossed to generate B3502**a** and B3501α. B3502**a** and B3501α were crossed to generate JEC20**a** and B-4478α. These strains were crossed, and an α progeny was selected and backcrossed to JEC20**a**. Backcrossing was repeated for a total of 10 times to create the congenic pair JEC20**a**/21α. * B3502**a** may be identical to JEC20**a** based on two previous studies [34,35]. (**B**) JEC20**a** and XL280α, progeny of B3502**a** and B3501α, were crossed, and an **a** progeny was selected and backcrossed to XL280α. Backcrossing was repeated for a total of 10 times to create congenic pair XL280**a**/XL280α. (**C**) 125.91**a** and 8-1α were crossed, and an **a** progeny was selected to mate with H99α *crg1*Δ. An **a** progeny without the *CRG1* mutation was then crossed with H99α. Backcrosses were continued for a total of 10 times to create congenic strains KN99**a**

and KN99α. (**D**) B3501α was crossed with JEC20**a**, and an **a** progeny was selected to backcross to B3501α. Backcrosses were repeated for a total of 10 times to generate congenic strains KN3501**a** and KN3501α. (**E**) NIH433**a** and JEC21α were crossed, and an **a** progeny was selected to backcross to NIH433**a**. Backcrosses were repeated for a total of 10 times to generate congenic strains KN433**a** and KN433α. (**F**) CBS1930**a** was crossed with R265α. An **a** progeny was selected to backcross to R265α, and backcrosses were repeated for a total of 10 times to yield AIR265**a** and AIR265α.

Table 1.1. The current *Cryptococcus* congenic pairs

Pair Name	JEC20/21		KN99		KN3501		KN433		XL280		AIR265	
Recipient Parent	B3502		H99		B3501		NIH433		XL280		R265	
Serotype	D		A		D		D		D		B	
Mating Type	**a**	α	**a**	α	**a**	α	**a**	α	**a**	α	**a**	α
Molecular Type	VNIV	VNIV	VNI	VNI	VNIV	VNIV	VNIV	VNIV	VNIV	VNIV	VGII	VGII
Self-filamentation	-	+	-	-	-	-	-	-	++	+++	-	-
Bisexual Mating	+++	+++	++	++	+++	+++	+++	+++	+++	+++	+	+
Virulence (i.n.)	⊣	⊣	+++	+++	n/a	n/a	n/a	n/a	++	++	+++	+++
Virulence (i.v.)	+	+⊣	+++	+++	+	+	+	+⊣	+++	+++	+++	+++
Reference	[19]	[19]	[29]	[29]	[27]	[27]	[27]	[27]	[30]	[30]	[23]	[23]

+: relatively robust ability, ⊣: modest ability, -: no ability.

CHAPTER 2

MOLECULAR DISSECTION OF CRZ1 AND ITS DYNAMIC SUBCELLULAR LOCALIZATION IN *CRYPTOCOCCUS NEOFORMANS* [2]

[2] Benjamin James Chadwick, Brittain Elizabeth Ross, and Xiaorong Lin. 2023. *J. Fungi*, 9(2), 252

Abstract

Across lower eukaryotes, the transcription factor Crz1 (calcineurin-responsive zinc finger) is dephosphorylated by calcineurin, which facilitates Crz1 translocation to the nucleus to regulate gene expression. In the fungal pathogen *Cryptococcus neoformans*, calcineurin-Crz1 signaling maintains calcium homeostasis, thermotolerance, cell wall integrity, and morphogenesis. How Crz1 distinguishes different stressors and differentially regulates cellular responses is poorly understood. Through monitoring Crz1 subcellular localization over time, we found that Crz1 transiently localizes to granules after exposure to high temperature or calcium. These granules also host the phosphatase calcineurin and Pub1, the ribonucleoprotein stress granule marker, suggesting a role of stress granules in modulating calcineurin-Crz1 signaling. Additionally, we constructed and analyzed an array of Crz1 truncation mutants. We identified the intrinsically disordered regions in Crz1 which contribute to proper stress granule localization, nuclear localization, and function. Our results provide the groundwork for further determination of the mechanisms behind the complex regulation of Crz1.

Introduction

Crz1 is an important downstream transcription factor in calcineurin signaling in lower eukaryotes [1]. Deletion of the *CRZ1* gene in pathogenic fungi has pleiotropic effects, with increased sensitivity to calcium and cell wall stress and attenuated virulence being common phenotypes. This has been observed in the rice blast fungus *Magnaporthe oryzae* [2] and in the opportunistic human fungal pathogens *Aspergillus fumigatus* [3,4], *Candida* species [5,6], and *Cryptococcus neoformans* [7-10]. In *C. neoformans*, the calcineurin-Crz1 pathway is also critical for the yeast to hypha transition induced by glucosamine [11].

Crz1 translocates from the cytosol to the nucleus after calcineurin-dependent dephosphorylation in the model yeast *Saccharomyces cerevisiae* [12]. This phosphorylation-dependent regulation of Crz1's subcellular localization appears conserved across lower eukaryotes. In *C. neoformans*, Crz1 may translocate to the nucleus in response to 37˚C, glucosamine, or calcium stress. In addition to trafficking between the cytosol and the nucleus, a punctate localization of Crz1 has been observed in response to high salt or high temperature shock [8,11]. How the subcellular localization of Crz1 and its function are differentially regulated in response to different stresses is poorly understood. *C. neoformans* Crz1 protein is ~1100 amino acids in length with a C-terminal DNA binding domain of ~90 amino acid long. The remaining ~1000 amino acids of the protein are mostly predicted to exist in an unfolded or disordered state. Disordered protein sequences have been shown to contribute to phase separation as well as transcription factor DNA binding activity [13-16]. It was recently demonstrated in the fungal pathogen *Candida albicans*, that the intrinsically disordered regions of the phosphatase Ptc2 allow it to phase separate in response to host CO_2 levels [17]. Because Crz1 contains many regions of intrinsic disorder with unknown function, we decided to investigate the molecular basis of Crz1 function and its subcellular localization by creating and examining Crz1 mutant proteins with truncations of different regions. Here, we report our systematic characterization of these mutant Crz1s' localization in response to calcium, glucosamine, heat, and salt stress, and their ability to complement the phenotypes of the *crz1*Δ mutant.

Materials and Methods

Strains and Media

All *C. neoformans* strains used are listed in Table 2.2. Cryptococcal cells were freshly thawed from 15% glycerol stocks stored at -80°C and cultured on YPD medium (1% yeast

extract, 2% BactoPeptone, and 2% dextrose) unless specified otherwise. For all growth assays involving comparisons of different strains, cells were firstly adjusted to the same optical density (OD) by quantification of the OD_{600} with a spectrophotometer or with the Biotek plate reader Epoch 2. For the spotting assays testing growth in hypoxia, an environment of 37°C, 0.1% O_2, and 5% CO_2 was maintained with a biospherix C chamber with a Pro-Ox controller and a Pro-CO_2 controller to maintain O_2/CO_2 levels (Biospherix, Lacona, NY, USA).

Genetic Manipulation

Plasmids and primers used in this study are listed in the Table 2.2. To overexpress and fluorescently label Crz1, the open reading frame of *CRZ1* was first PCR amplified and cloned into the vectors with mCherry and mNeonGreen for tagging after restriction enzyme digestion. The vectors contain the *GPD1* promoter for constitutive overexpression and a neomycin (NEO) drug selection marker. Internally truncated *CRZ1* mutant alleles were generated by overlap PCR (or fusion PCR). The primers used for each construct are listed in the Table 2.2. All mutant *CRZ1* allele constructs and the wild-type allele construct were cloned into the same plasmid backbone, pUC19, with expression controlled by the *GPD1* promoter and with a C-terminal mNeonGreen tag. The constructs were introduced into *C. neoformans crz1*Δ mutant genome by TRACE (transient CRISPR-Cas9 coupled with electroporation) [18,19] and transformants were selected on 100 μg/ml of G418. All constructs in the selected transformants were integrated into the "safe haven" locus *SH2* [19,20].

Microscopy

C. neoformans strains were observed under a Zeiss Imager M2 microscope, and all images were acquired by an AxioCam MRm camera and processed with Zen pro software (Carl Zeiss Microscopy). For heat shock experiments, cells grown overnight at 22˚C were prepared for

microscopy on a 42˚C pre-heated glass slide and incubated at 42˚C for 15-20 minutes. For high calcium and salt shock experiments, cells were suspended in water containing 1M NaCl or 100mM $CaCl_2$ for 15-20 minutes. The cells were then immediately examined under the microscope. For timelapse experiments involving heating, cells were prepared on a pre-warmed slide and examined on the same Zeiss Imager M2 microscope equipped with a heated stage (PE120 Linkam stage, McCrone Microscopes & Accessories). For timelapse experiments testing response to $CaCl_2$, cells were suspended in 1mM $CaCl_2$ on a microscope slide and immediately imaged.

Results

The *crz1*Δ mutant displays pleiotropic growth defects

We first tested the growth of the *crz1*Δ mutant in various stressful conditions. The *crz1*Δ mutant grew poorly at 39˚C or under the hypoxia condition (Figure 2.1A). In addition, the *crz1*Δ mutant was sensitive to SDS (membrane disrupting detergent), Congo Red (cell wall stressor), and high calcium (Figure 2.1A). Our observation is consistent with previous findings that, deletion of the *CRZ1* gene in *C. neoformans* led to increased sensitivity to cell wall stresses, high temperature, calcium, and hypoxia [7,8,10,21]. However, the *crz1*Δ mutant showed no growth defects in 1M NaCl and it grew noticeably better than the WT strain on the filamentation-inducing media YP + Glucosamine. This is likely due to the fact that the *crz1*Δ mutant grows in the yeast form on this medium while H99 can grow filamentously and filamentous growth rate is slower relative to yeast growth rate in *C. neoformans* [11].

As previously described, the *crz1*Δ mutant grew similarly as the wild type at 30˚C but poorly at 39˚C after two days of incubation on plates at the constant temperature, indicating that Crz1 is important for thermotolerance. To test if Crz1 is important for adaptation after a brief

heat-shock, we tested the recovery growth of both WT H99 and the *crz1*Δ mutant at 30°C after 20 minutes of incubation at 42°C in liquid culture. When cultured at the constant temperature of 30°C without heat shock, there was a slight growth defect of the *crz1*Δ mutant compared to the WT strain (left graph, Figure 2.1B). However, with the short heat shock at 42°C, the growth defect of the *crz1*Δ mutant was exacerbated (Figure 2.1B). These results indicate that Crz1 is important for heat shock adaptation even after a short exposure to high temperature.

Crz1 co-localizes to stress granules with Pub1 and calcineurin in response to heat or salt stress

Under non-stimulating conditions, Crz1 showed diffused cytoplasmic localization in most cells and enriched nuclear localization in a small proportion of the population (Figure 2.2A), as we expected based on our previous study [11]. In response to heat (42˚C) or salt (1 M NaCl) shock, we found that both an N-terminal mCherry tagged Crz1 fusion protein (mCh-Crz1) and a C-terminal mNeonGreen tagged Crz1 fusion protein (Crz1-mNG) localized to granules in all cells (Figure 2.2A). Previously, Kozubowski et al. found that calcineurin (Cna1) co-localizes with the polyA-binding protein Pub1 in stress granules at 37°C [22]. Pub1 is a known marker for stress granules in response to starvation, heat shock, or acidification [23]. Because Crz1 is a known downstream target of calcineurin, we decided to test if Crz1 co-localizes with calcineurin catalytic subunit Cna1 or Pub1 at high temperatures or in high salt. To that end, we introduced the Crz1-mNG into a strain harboring Pub1-mCherry and the mCh-Crz1 into a strain harboring Cna1-GFP. Under the non-stimulating control condition (22°C), Crz1 and Pub1 were mostly diffused in the cytoplasm with some cells showing enrichment in the nucleus (Figure 2.2B, top left images). By contrast, calcineurin Cna1 was in the cytoplasm and likely excluded from the nucleus (Figure 2.2C, top right images). In response to 42°C or salt shock, we found that Crz1

localized to granules and these granules co-localized with Pub1 (Figure 2.2B) and calcineurin Cna1 (Figure 2.2C). Taking these observations into consideration, we hypothesize that co-localization of Crz1 and the phosphatase calcineurin to stress granules may be a mechanism to promote their interaction and facilitate dephosphorylation of Crz1 and its subsequent translocation to the nucleus.

Crz1 localizes to stress granules at host physiological conditions

Crz1 was previously found to localize to the nucleus when cells were grown overnight at the mammalian host temperature of 37°C or after being exposed to 100mM $CaCl_2$ [8,11]. Here we found that Crz1 localizes to stress granules after a short exposure to high temperature and salt. We wondered if the seemingly conflicting localizations of Crz1 is due to dynamic trafficking of Crz1 and the differences in the timing of observation in previous studies and this study. We therefore monitored Crz1-mNeonGreen localization in the same cells over time in response to a temperature shift from 22°C to 37°C. Interestingly, after 5 minutes of 37°C heat shock, Crz1 was found in puncta of some cells (Figure 2.3A). Crz1 of the same cells then later localized to the nucleus after 30 minutes (arrow heads in Figure 2.3A). This result further supports our hypothesis that stress granule localization facilitates Crz1 translocation to the nucleus, likely by promoting interaction between Crz1 and calcineurin. This punctate-to-nucleus translocation was not observed when cells were exposed to 100mM $CaCl_2$. Because *Cryptococcus* is likely exposed to much lower concentrations of calcium in the host than 100mM $CaCl_2$ used in earlier studies (e.g. $CaCl_2$ concentration in serum is ~2.2-2.6mM), we then tested Crz1 localization in response to 1mM $CaCl_2$. We noticed that some cells displayed nuclear localized Crz1 in less than 1 minute of exposure to exogenous calcium at 1mM, while a majority of cells displayed punctate Crz1 localization after 5 minutes (Figure 2.3B, Supplemental video S1, Supplemental video S2). We

monitored Crz1 localization in response to 1mM $CaCl_2$ for up to 30 minutes and found the puncta localization was stable for the whole duration. We observed similar puncta localization of Crz1 after exposure to 10 mM $CaCl_2$. Thus, it seems that granular localization of Crz1 likely occurs in the host.

Crz1 localizes to the mother-daughter bud neck in response to stress conditions

While subjecting cryptococcal cells to a variety of stresses, we noticed localization of Crz1-mNeonGreen to the bud neck of replicating cells (mother cells with daughter buds). At room temperature without any added stress, Crz1 localization to the bud neck was not observed. To examine the dynamics of this bud neck localization, we monitored Crz1-mNeonGreen over time after exposure to a 1mM $CaCl_2$ shock (Figure 2.4A, Supplemental video S3). For a period of 12 minutes, gradual accumulation of Crz1-mNeonGreen signal in both the nucleus and the bud neck was observed. We further tested bud neck localization of Crz1 in response to 37°C, 1M NaCl, 1mM $CaCl_2$, and 42°C heat shock. For each condition, we analyzed over 100 mother-daughter pairs and categorized them as showing Crz1 bud neck localization or not. We further measured the diameter of the budding daughter cells to test if Crz1's bud neck localization correlates with the size of buds. Interestingly, Crz1's bud neck localization was observed in response to each stress tested, and it was primarily observed in a subset of the cells which have larger buds (Figure 2.4B). The median bud length measured for all conditions was ~2.6μm, with the minimum and maximum lengths found being 0.5μm and 4.0μm respectively. Over 20% of all budding cells and over 60% of cells with a diameter over 3μm displayed the bud neck localization of Crz1. Because we only captured images at a single timepoint, it is likely that these percentages are an underestimate of cells where Crz1 localizes to the bud neck. These data suggest that Crz1 likely localizes to the bud neck prior to cell separation.

Crz1 truncation analysis reveals functionally critical regions

The Crz1 protein contains a C-terminal DNA binding domain (DBD) which makes up less than 10% of the protein sequence, and several intrinsically disorder regions (IDRs) predicted by PONDR [24] (Figure 2.5A). Consistent with this domain prediction, AlphaFold software predicts one defined domain in the Crz1 protein sequence which corresponds to the DBD, and no other inter-protein interactions in the remaining sequence [25,26](Figure 2.5B,C). The near N-terminal disordered sequence also contains a poly glutamine (polyQ) track which may contribute to granular localization [27,28]. In addition, 7 serine phosphorylation sites which are known to be dephosphorylated by calcineurin add an additional layer of Crz1 regulation [21]. To identify what regions of the Crz1 protein sequence are important for its localization and function in response to different stresses, we created 10 internal (Δ) and N-terminal (ΔN) truncated Crz1 mutant alleles, as well as a polyQ mutant Crz1$^{(polyQ\rightarrow A)}$ (Figure 2.5D). We also utilized the existing phosphorylation site mutant Crz1$^{(7S\rightarrow A)}$ [21]. We then tagged these mutant proteins with mNeonGreen and introduced them into the *crz1*Δ mutant background to test for functional complementation. To minimize variations on gene expression caused by positional effects, we integrated all the constructs into the same "safe haven" *SH2* genetic locus [19,20]. For comparison, we also introduced the WT Crz1 protein sequence tagged with mNeonGreen into the *crz1*Δ mutant background using the same procedure. All Crz1 WT and mutant alleles were tested for 1) their ability to compensate for the loss of Crz1 in terms of growth in high temperatures, hypoxia, and media supplemented with calcium, Congo red, SDS, and glucosamine (Figure 2.5E) and 2) their subcellular localization in response to various stresses (Table 2.1). For subcellular localization, a total of 100 cells were counted for each condition, and the percent of cells

showing nuclear localization (as opposed to cytosolic), or granular localization are recorded in Table 2.1.

As expected, the WT Crz1 construct was able to rescue all defects of the *crz1*Δ mutant examined (Figure 2.5E). To our surprise, mutations of the polyQ did not compromise functional complementation or granular localization. The Crz1$^{(polyQ\rightarrow A)}$ mutant protein showed reduced localization to the nucleus in response to 37˚C (32% vs. 99% in the nucleus, Table 2.1), but there was no discernable growth defect of this mutant strain even at 39˚C (Figure 2.5E). Similarly, mutation of the seven phosphorylation sites did not compromise complementation in any of the growth assays (Figure 2.5E). The Crz1$^{(7S\rightarrow A)}$ mutant expectedly displayed increased localization in the nucleus at 22˚C (37% vs. 13% in WT) and after a 42˚C heat shock (100% of cells displayed nuclear localization vs. granular localization of the wildtype). In response to 1M NaCl, 100% of cells showed Crz1$^{(7S\rightarrow A)}$ in granules, indicating these seven phosphorylation sites are not required for granular localization.

Deletions of the different intrinsically disordered regions had various impacts on the function and subcellular localization of Crz1. Interestingly, deletion of the first 257 amino acids, which includes part of IDR1 and the polyQ site, did not affect Crz1's function in the conditions tested. However, the Crz1$^{(\Delta N\ 1\text{-}257)}$ mutant showed decreased granular localization in response to 42˚C heat shock (36% versus 100% in WT). Deletion of the second part of IDR1 (ΔN 263-451) had a negative effect on the ability of Crz1 to restore cell wall stress, but not other stresses (Figure 2.5E). Truncation of the first 368 amino acids (ΔN 1-368), which includes the entire IDR1 region, caused a total loss of function because the Crz1$^{(\Delta N\ 1\text{-}368)}$ mutant behaved exactly like the *crz1*Δ mutant in our spotting assays. The Crz1$^{(\Delta N\ 1\text{-}368)}$ protein was constitutively found in the nucleus, indicating that this region contains a possible nuclear exporting signal. Not

surprisingly, the larger N-terminal truncation mutants, namely the Crz1$^{(\Delta N\ 1\text{-}451)}$ mutant, the Crz1$^{(\Delta N\ 1\text{-}705)}$ mutant, the Crz1$^{(\Delta N\ 1\text{-}802)}$ mutant, and the Crz1$^{(\Delta N\ 1\text{-}823)}$, mutant had the same phenotype as the *crz1*Δ mutant.

Deletion of the IDR2 region (Δ625-665) in the middle of the protein did not have any compromising effects in these growth assays, although its deletion abolished granular localization in response to 42˚C shock (0%) and slightly reduced granular localization in response to 1M NaCl (84% vs. 99% in the WT. Strikingly, deletion of the IDR3 region (Δ833-926) caused constitutive nuclear localization as well as loss of function in spotting assays. Likewise, the DBD mutant, Crz1$^{(\Delta N\ 946\text{-}1030)}$, displayed similar localization and loss of function as the IDR3 region mutant Crz1$^{(\Delta N\ 833\text{-}926)}$. The IDR3 region is located directly upstream of the DBD and may play a critical role in its function. Notably, the IDR3 mutant allele Crz1$^{(\Delta N\ 833\text{-}926)}$, the DBD mutant allele, and the N-terminal truncated allele Crz1$^{(\Delta N\ 1\text{-}368)}$ were all not functional and were constitutively localized to the nucleus, indicating these regions may all contribute to proper DNA binding and/or transcriptional activity.

Discussion

Lev et al. [8] first demonstrated that Crz1 localizes to granules in response to high salt or heat shock, and additionally, that Crz1 does not co-localize with polyA-binding protein Pab1 granules. Here, we found that Crz1 does co-localize with Pub1 granules. Our finding is consistent with previous findings in *S. cerevisiae* that Pab1 and Pub1 localize with different RNA binding proteins and/or stress granule components, indicating that the cytosol contains various types of RNP granules which may serve different functions [29,30].

Intrinsically disordered regions (IDRs) within proteins have been implicated as the drivers of granular assembly (or phase separation) [15,16]. For example, interactions between the 3

IDRs of the human stress granule assembly factor G3BP1 are regulated by phosphorylation, which will toggle the protein between closed and open states, the latter of which leads to stress granule assembly [15]. We identified three IDRs in the Crz1 protein sequence (Figure 2.5A), and individual Crz1 IDR truncations caused partial loss of stress granule localization (Figure 2.5B, Table 2.1). However, neither mutating the seven known phosphorylation sites (mimicking a dephosphorylated state) nor inhibiting the phosphatase calcineurin with FK506 (mimicking an enhanced phosphorylated state) prevented granular localization of Crz1, indicating a mechanism different from phosphorylation for regulation of phase separation. IDRs have been demonstrated to mediate transcription factor activity through liquid phase separation, DNA binding, or protein-protein interactions [13,14]. In our study, disruption of IDRs had deleterious effects on Crz1 function. For example, deletion of the IDR 3 region located upstream of the DBD abolished Crz1 function in all assays (Figure 2.5B), indicating its critical role in mediating Crz1's transcription factor activity.

It was previously known that Crz1 translocates to the nucleus in response to increasing temperature from room temperature to 37˚C. By examining cells expressing Crz1-mNeonGreen over time, we found that Crz1 may first localize to granules before nuclear translocation after the temperature shift (Figure 2.3A). Furthermore, Crz1 localizes to stress granules in addition to the nucleus in response to exogenous calcium at the near host serum levels (Figure 2.3B). These data, together with our observations that Crz1 co-localizes with the phosphatase calcineurin to stress induced granules, suggest that Crz1 localization to stress granules facilitates its translocation to the nucleus due to enhanced dephosphorylation by calcineurin. As multiple known targets of calcineurin localize to RNP granules [21], we suspect that granular localization of

these proteins, including Crz1, may be a general mechanism to facilitate their dephosphorylation by calcineurin.

We also observed that Crz1 localizes to the bud neck under stress granule inducing conditions, specifically in cells with larger buds (Figure 2.4). Interestingly, calcineurin also localizes to the bud neck and may play a critical role in coordinating cytokinesis and septation in *C. neoformans* under these stressful conditions through affecting its various substrate protein targets [22,31,32]. Like Crz1, another calcineurin substrate protein Cts1 co-localizes with calcineurin and Pub1 to cytoplasmic puncta and localizes to the bud neck of large budded cells [31,32]. Additionally, deletion of the *CTS1* gene caused defects in budding at 37˚C [32]. Calcineurin's involvement in septation has also been demonstrated in *A. fumigatus* [33-35] and *Schizosaccharomyces pombe* [36]. Whether or not Crz1 plays an active role in septation or budding, either alone or in collaboration with other factors targeted by calcineurin, should be investigated in future studies.

Interestingly, loss of Crz1 does not confer any obvious growth defects in some of the conditions which induce granules (Figure 2.1). This is not surprising, as loss of Crz1 also does not clearly hamper cryptococcal growth at 37˚C or in the presence of 400mM calcium [8] even though both conditions induce Crz1 nuclear translocation and activate its transcriptional activity [10]. While growth of the *crz1*Δ mutant does not appear to be sensitive at 37˚C, it is sensitive at 39˚C (Figure 2.5C). Moreover, double mutants of Crz1 and other calcineurin target proteins localized to granules caused thermosensitivity at 37˚C [21]. These observations suggest robust redundancy of calcineurin substrate protein function in ensuring cell separation and growth at higher temperature.

Supplementary Materials

The following supporting information can be downloaded at: https://www.mdpi.com/article/10.3390/jof9020252/s1, Video S1: Crz1 response to 1 mM Calcium, Video S2: Crz1 response to 1 mM Calcium; Video S3: Crz1 dynamic localization to the bud neck.

Author Contributions

Conceived and designed the experiments: B.J.C., X.L; Performed the experiments: B.J.C., B.E.R; Wrote the manuscript: B.J.C.; Edited the manuscript: B.J.C. and X.L. All authors have read and agreed to the published version of the manuscript.

Funding

This work was supported by National Institutes of Health (http://www.niaid.nih.gov) (R01AI140719 to X.L.). The funder had no role in study design, data collection, and interpretation, or the decision to submit the work for publication.

Acknowledgments

We thank all Lin lab members for their helpful suggestions. We are grateful to Dr. Lukasz Kozubowski for the gift of the plasmids LKB39, LKB60, LKB61, and LKB88.

Conflicts of Interest

The authors declare no competing interests.

References

1. Thewes, S. Calcineurin-Crz1 signaling in lower eukaryotes. *Eukaryot Cell* **13**, 694-705 (2014).
2. Choi, J., Kim, Y., Kim, S., Park, J. & Lee, Y.H. MoCRZ1, a gene encoding a calcineurin-responsive transcription factor, regulates fungal growth and pathogenicity of Magnaporthe oryzae. *Fungal Genet Biol* **46**, 243-54 (2009).
3. Cramer, R.A., Jr. *et al.* Calcineurin target CrzA regulates conidial germination, hyphal growth, and pathogenesis of Aspergillus fumigatus. *Eukaryot Cell* **7**, 1085-97 (2008).
4. Shwab, E.K. *et al.* Calcineurin-dependent dephosphorylation of the transcription factor CrzA at specific sites controls conidiation, stress tolerance, and virulence of Aspergillus fumigatus. *Mol Microbiol* **112**, 62-80 (2019).

5. Chen, Y.L. *et al.* Calcineurin controls hyphal growth, virulence, and drug tolerance of Candida tropicalis. *Eukaryot Cell* **13**, 844-54 (2014).
6. Santos, M. & de Larrinoa, I.F. Functional characterization of the Candida albicans CRZ1 gene encoding a calcineurin-regulated transcription factor. *Curr Genet* **48**, 88-100 (2005).
7. Moranova, Z. *et al.* The CRZ1/SP1-like gene links survival under limited aeration, cell integrity and biofilm formation in the pathogenic yeast Cryptococcus neoformans. *Biomed Pap Med Fac Univ Palacky Olomouc Czech Repub* **158**, 212-20 (2014).
8. Lev, S., Desmarini, D., Chayakulkeeree, M., Sorrell, T.C. & Djordjevic, J.T. The Crz1/Sp1 transcription factor of Cryptococcus neoformans is activated by calcineurin and regulates cell wall integrity. *PLoS One* **7**, e51403 (2012).
9. Adler, A. *et al.* A novel specificity protein 1 (SP1)-like gene regulating protein kinase C-1 (Pkc1)-dependent cell wall integrity and virulence factors in Cryptococcus neoformans. *J Biol Chem* **286**, 20977-90 (2011).
10. Chow, E.W. *et al.* Elucidation of the calcineurin-Crz1 stress response transcriptional network in the human fungal pathogen Cryptococcus neoformans. *PLoS Genet* **13**, e1006667 (2017).
11. Xu, X. *et al.* Glucosamine stimulates pheromone-independent dimorphic transition in *Cryptococcus neoformans* by promoting Crz1 nuclear translocation. *PLOS Genetics* **13**, e1006982 (2017).
12. Stathopoulos-Gerontides, A., Guo, J.J. & Cyert, M.S. Yeast calcineurin regulates nuclear localization of the Crz1p transcription factor through dephosphorylation. *Genes Dev* **13**, 798-803 (1999).
13. Brodsky, S., Jana, T. & Barkai, N. Order through disorder: The role of intrinsically disordered regions in transcription factor binding specificity. *Current Opinion in Structural Biology* **71**, 110-115 (2021).
14. Brodsky, S. *et al.* Intrinsically Disordered Regions Direct Transcription Factor In Vivo Binding Specificity. *Molecular Cell* **79**, 459-471.e4 (2020).
15. Yang, P. *et al.* G3BP1 Is a Tunable Switch that Triggers Phase Separation to Assemble Stress Granules. *Cell* **181**, 325-345.e28 (2020).
16. Protter, D.S.W. *et al.* Intrinsically Disordered Regions Can Contribute Promiscuous Interactions to RNP Granule Assembly. *Cell Reports* **22**, 1401-1412 (2018).
17. Zhang, M. *et al.* The intrinsically disordered region from PP2C phosphatases functions as a conserved CO_2 sensor. *Nature Cell Biology* **24**, 1029-1037 (2022).
18. Fan, Y. & Lin, X. Multiple Applications of a Transient CRISPR-Cas9 Coupled with Electroporation (TRACE) System in the *Cryptococcus neoformans* Species Complex. *Genetics* **208**, 1357-1372 (2018).
19. Lin, J., Fan, Y. & Lin, X. Transformation of *Cryptococcus neoformans* by electroporation using a transient CRISPR-Cas9 expression (TRACE) system. *Fungal genetics and biology : FG & B* **138**, 103364-103364 (2020).
20. Upadhya, R. *et al.* A fluorogenic *C. neoformans* reporter strain with a robust expression of m-cherry expressed from a safe haven site in the genome. *Fungal Genet Biol* **108**, 13-25 (2017).
21. Park, H.-S. *et al.* Calcineurin Targets Involved in Stress Survival and Fungal Virulence. *PLOS Pathogens* **12**, e1005873 (2016).

22. Kozubowski, L., Aboobakar, E.F., Cardenas, M.E. & Heitman, J. Calcineurin colocalizes with P-bodies and stress granules during thermal stress in *Cryptococcus neoformans*. *Eukaryot Cell* **10**, 1396-402 (2011).
23. Kroschwald, S. *et al.* Different Material States of Pub1 Condensates Define Distinct Modes of Stress Adaptation and Recovery. *Cell Reports* **23**, 3327-3339 (2018).
24. Romero, P., Obradovic, Z., Li, X., Garner, E.C., Brown, C.J. & Dunker, A.K. Sequence complexity of disordered protein. *Proteins* **42**, 38-48 (2001).
25. Jumper, J. *et al.* Highly accurate protein structure prediction with AlphaFold. *Nature* **596**, 583-589 (2021).
26. Varadi, M. *et al.* AlphaFold Protein Structure Database: massively expanding the structural coverage of protein-sequence space with high-accuracy models. *Nucleic Acids Res* **50**, D439-d444 (2022).
27. Lee, C., Occhipinti, P. & Gladfelter, A.S. PolyQ-dependent RNA-protein assemblies control symmetry breaking. *J Cell Biol* **208**, 533-44 (2015).
28. Marcelo, A., Koppenol, R., de Almeida, L.P., Matos, C.A. & Nóbrega, C. Stress granules, RNA-binding proteins and polyglutamine diseases: too much aggregation? *Cell Death Dis* **12**, 592 (2021).
29. Buchan, J.R., Muhlrad, D. & Parker, R. P bodies promote stress granule assembly in *Saccharomyces cerevisiae*. *J Cell Biol* **183**, 441-55 (2008).
30. Mitchell, S.F., Jain, S., She, M. & Parker, R. Global analysis of yeast mRNPs. *Nat Struct Mol Biol* **20**, 127-33 (2013).
31. Fox, D.S., Cox, G.M. & Heitman, J. Phospholipid-binding protein Cts1 controls septation and functions coordinately with calcineurin in *Cryptococcus neoformans*. *Eukaryot Cell* **2**, 1025-35 (2003).
32. Aboobakar, E.F., Wang, X., Heitman, J. & Kozubowski, L. The C2 domain protein Cts1 functions in the calcineurin signaling circuit during high-temperature stress responses in *Cryptococcus neoformans*. *Eukaryot Cell* **10**, 1714-23 (2011).
33. Juvvadi, P.R. & Steinbach, W.J. Calcineurin Orchestrates Hyphal Growth, Septation, Drug Resistance and Pathogenesis of *Aspergillus fumigatus*: Where Do We Go from Here? *Pathogens* **4**, 883-93 (2015).
34. Juvvadi, P.R., Fortwendel, J.R., Rogg, L.E., Burns, K.A., Randell, S.H. & Steinbach, W.J. Localization and activity of the calcineurin catalytic and regulatory subunit complex at the septum is essential for hyphal elongation and proper septation in *Aspergillus fumigatus*. *Mol Microbiol* **82**, 1235-59 (2011).
35. Juvvadi, P.R., Fortwendel, J.R., Pinchai, N., Perfect, B.Z., Heitman, J. & Steinbach, W.J. Calcineurin localizes to the hyphal septum in *Aspergillus fumigatus*: implications for septum formation and conidiophore development. *Eukaryot Cell* **7**, 1606-10 (2008).
36. Lu, Y. *et al.* Calcineurin is implicated in the regulation of the septation initiation network in fission yeast. *Genes Cells* **7**, 1009-19 (2002).
37. Nielsen, K., Cox, G.M., Wang, P., Toffaletti, D.L., Perfect, J.R. & Heitman, J. Sexual cycle of *Cryptococcus neoformans* var. *grubii* and virulence of congenic a and alpha isolates. *Infect Immun* **71**, 4831-41 (2003).

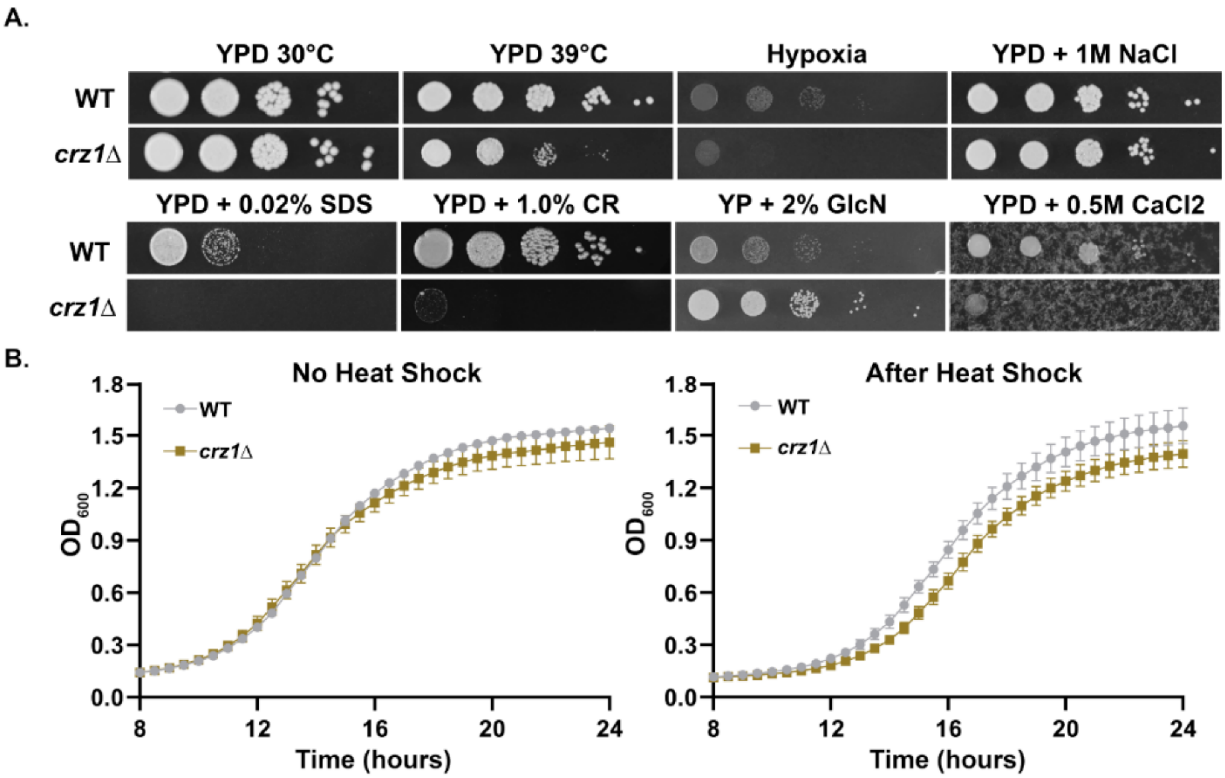

Figure 2.1. Growth assays of the *crz1*Δ mutant under various stress conditions. (**A**) The WT strain H99 and the *crz1*Δ mutant were grown overnight in liquid YPD at 30 °C, washed, adjusted to the same cell concentration, serially diluted, and spotted onto the media and incubated under the indicated conditions. Images were taken two days after incubation. (**B**) The overnight cultures of H99 and the *crz1*Δ mutant were split into two groups and diluted to OD_{600} = 0.1 in YPD medium. Three replicates of each strain were included per group. One group was inoculated into a 24-well microplate and incubated at 30 °C with double orbital shaking in a Biotek Epoch 2plate reader. Growth was monitored every 30 min by measuring OD_{600}. The second group was heat shocked by incubation at 42 °C for 20 min in a thermocycler prior to monitoring growth at 30 °C in the Epoch 2.

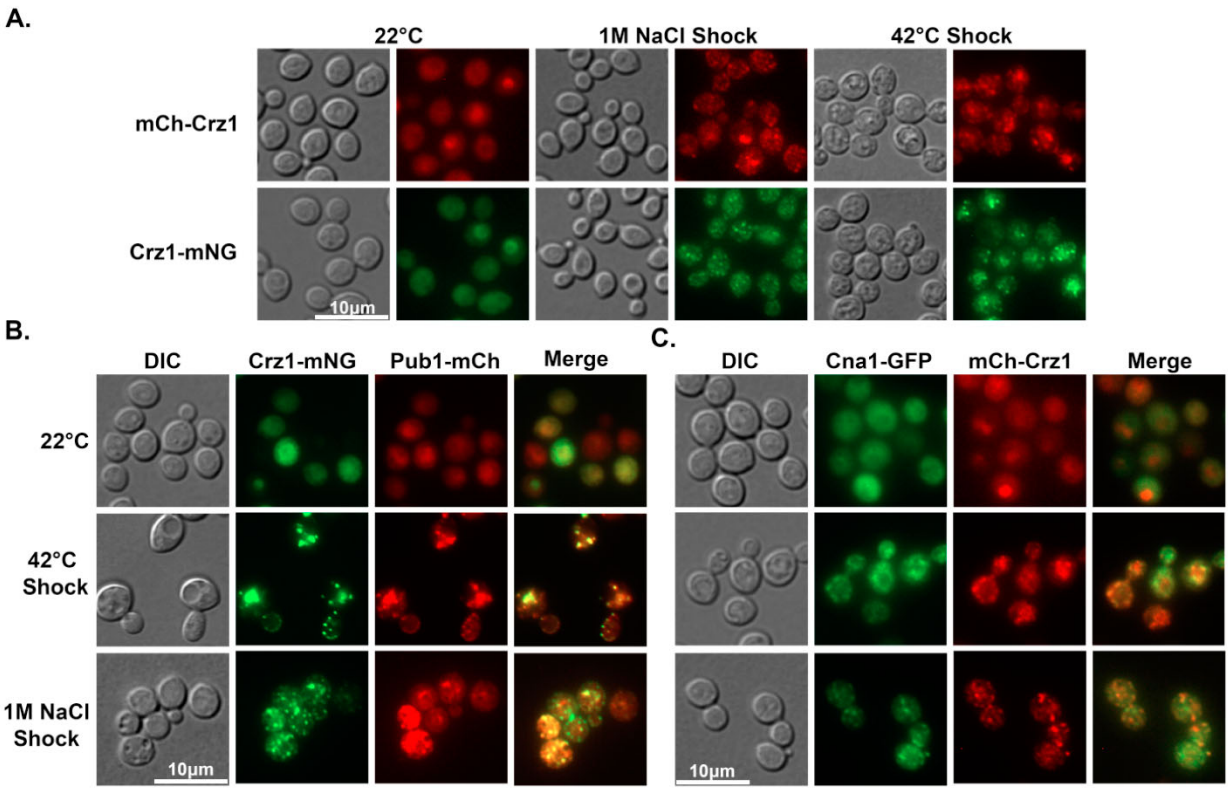

Figure 2.2. Crz1 co-localizes to stress granules with Pub1 and calcineurin in response to heat or salt shock. (**A**) mCherry-Crz1- or Crz1-mNeonGreen-expressing cells were incubated at 22 °C overnight and fluorescence was observed. To test the effects of salt and heat shock, cells were suspended in 1 M NaCl or exposed to 42 °C for 15–20 min prior to microscopic examination. (**B**) The same procedure was done with cells expressing both Crz1-mNeonGreen and Pub1-mCherry and (**C**) cells expressing both mCherry-Crz1 and Cna1-GFP. The scale of all images in each panel is the same.

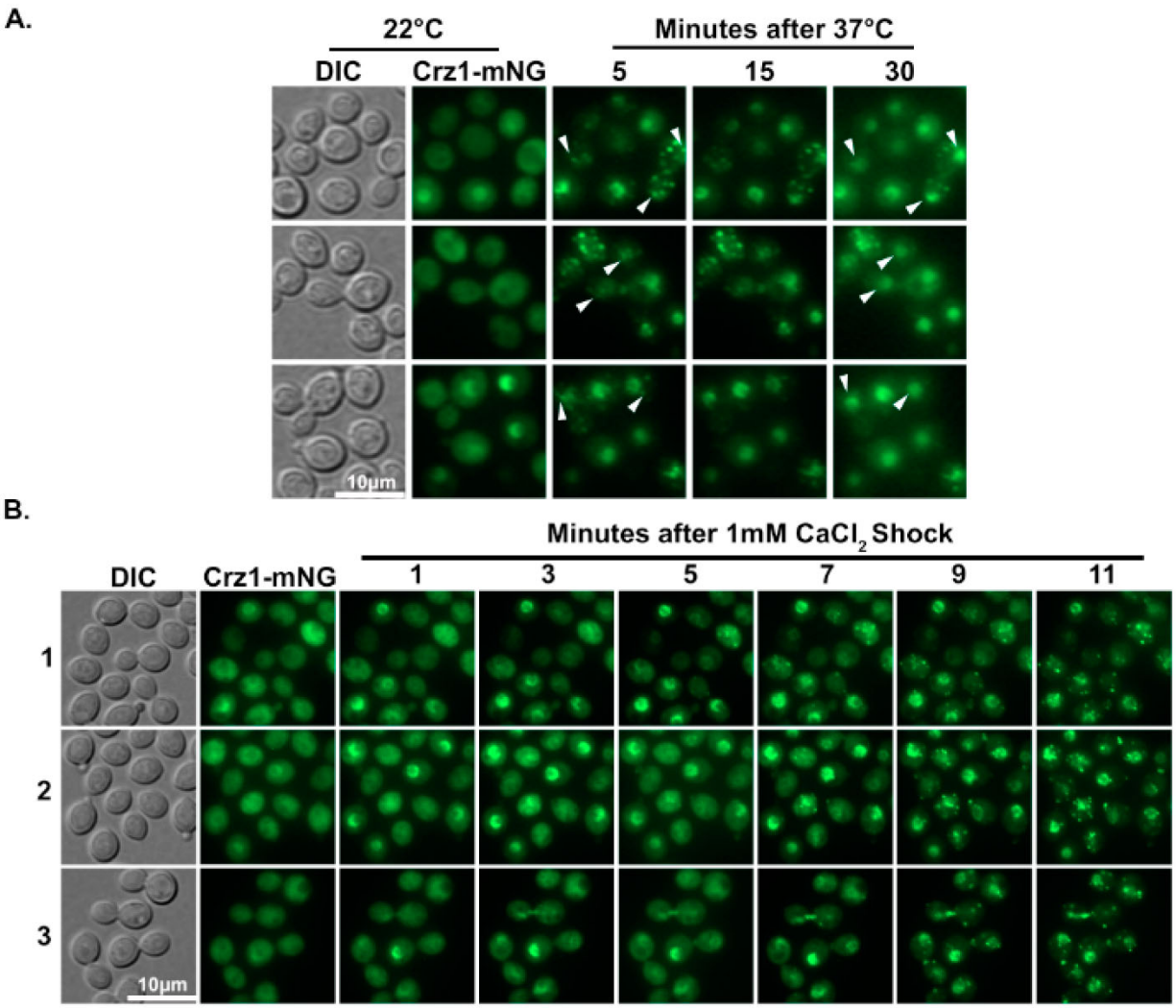

Figure 2.3. Crz1 localizes to granules at conditions relevant to host physiology. (**A**) Cells expressing Crz1-mNeonGreen were initially grown overnight at 22 °C. The cells were then prepared for microscopy on a 37 °C pre-heated glass slide and examined on a microscope equipped with a heated stage set to 37 °C. White arrowheads indicate examples of cells where Crz1 localized to granules first before typical nuclear localization in response to 37 °C. (**B**) The same cells grown overnight at 22 °C were suspended in 1 mM $CaCl_2$ on a microscope slide and immediately imaged (Crz1-mNG). Images were taken of the same field of view at the indicated times. The scale is the same for all images in the same panel.

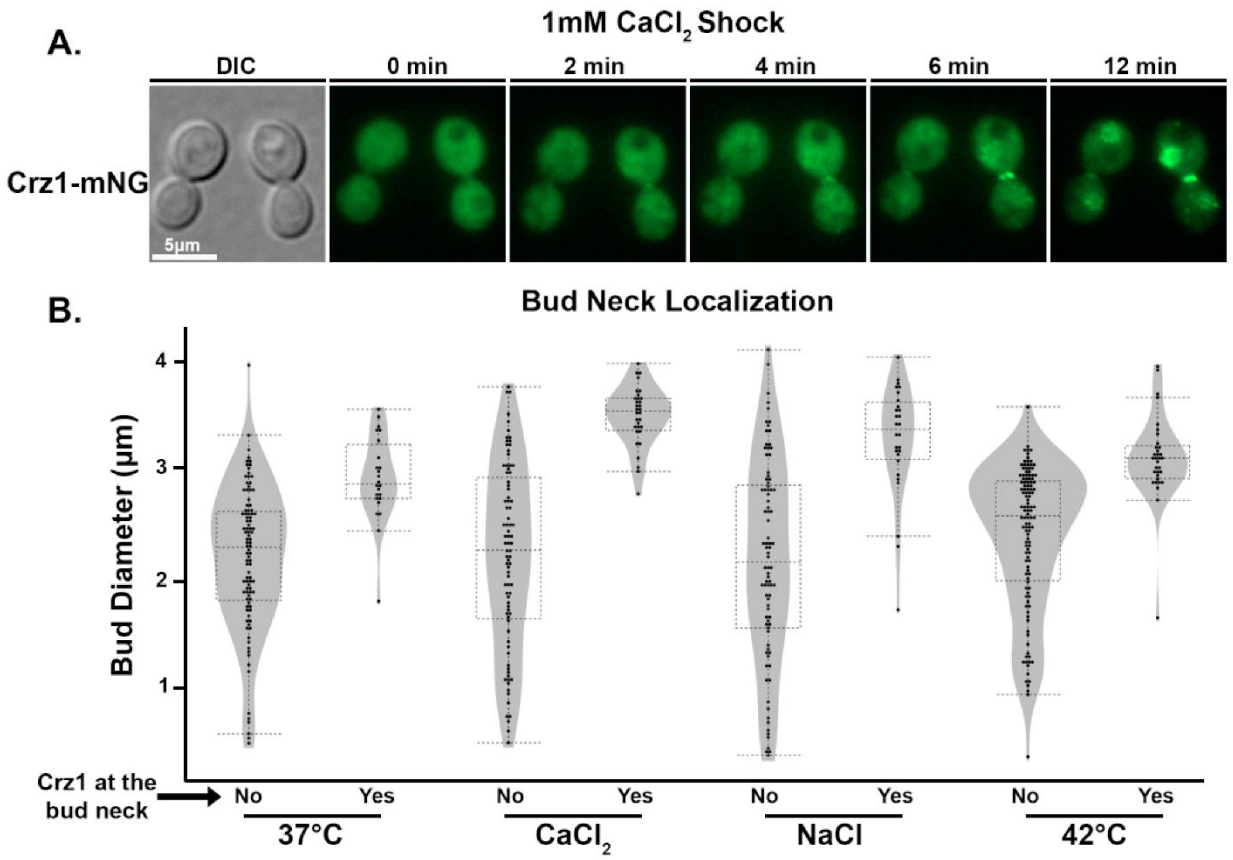

Figure 2.4. Crz1 localizes to the bud neck in response to stress. (**A**) Cells expressing Crz1-mNeonGreen were suspended in 1 mM $CaCl_2$ on a microscope slide and immediately imaged. The same field of view was captured at the indicated times and representative images are shown. (**B**) Cells with buds were characterized as having Crz1-mNG localization at the bud neck or not. The diameter of each bud was measured using ZEN 3.1 software. Over 100 cells were quantified per condition tested.

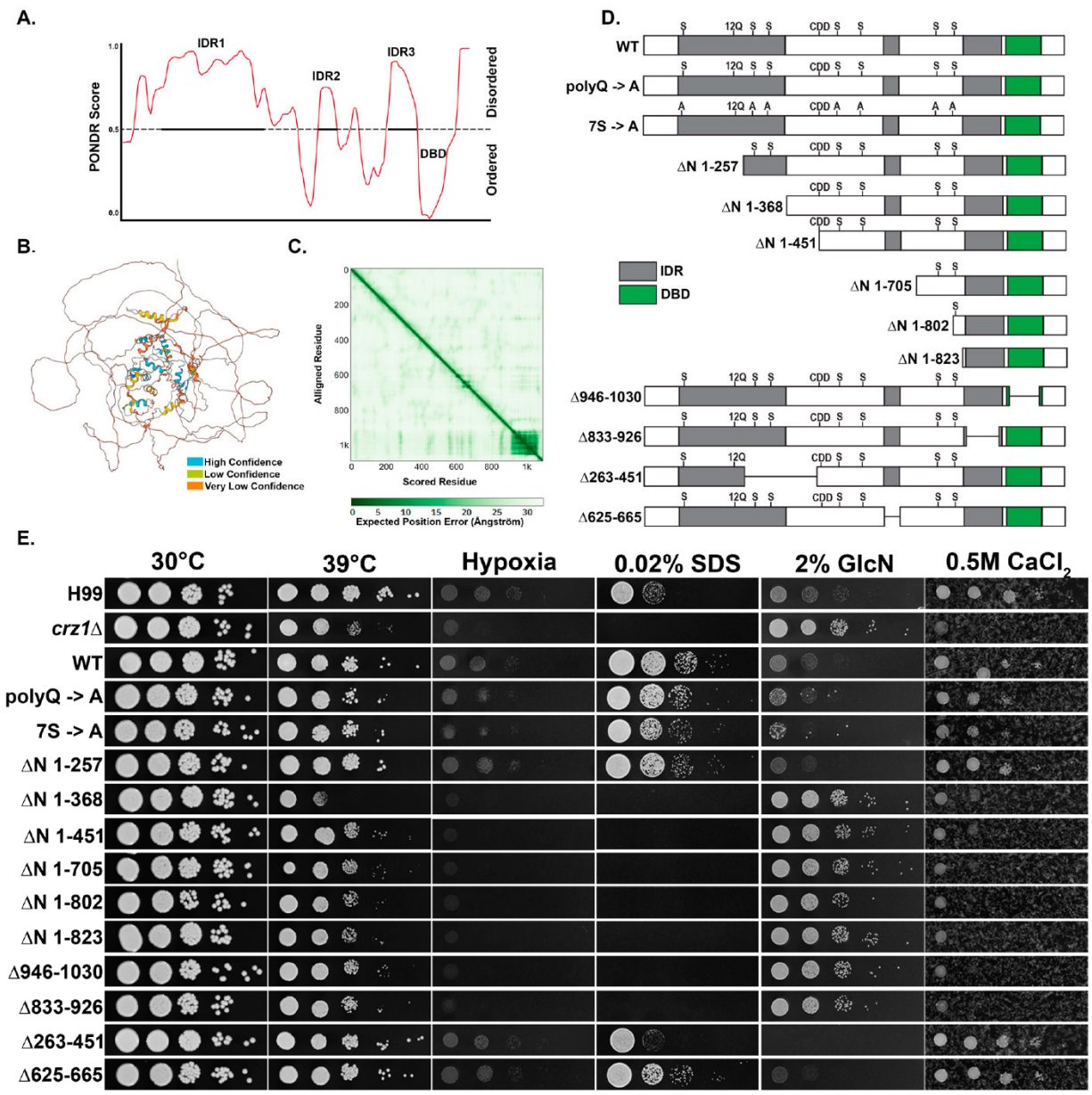

Figure 2.5. Mutational analysis of the Crz1 protein. (**A**) Results of PONDR (Predictor of Natural Disordered Regions) analysis of Crz1. A higher score correlates with higher disorder in the protein sequence. (**B**) AlphaFold prediction of Crz1 protein structure. The color pattern indicates the confidence level of the prediction. (**C**) The AlphaFold predicted aligned error plot shows dark green patches indicative of inter-protein interactions. (**D**) Protein diagrams of Crz1 mutant alleles used in this study. Green indicates the DNA binding domain (DBD) and grey

indicates regions of intrinsic disorder (IDRs). The putative calcineurin-docking domain (CDD) [10], phosphorylation sites (S) [21], and polyQ region (12Q) are labeled. (**E**) The WT strain H99, the crz1Δ mutant, and mutant alleles in the *crz1*Δ mutant background were grown overnight in YPD, serially diluted, and spotted onto the media and incubated for two days as indicated.

Table 2.1. Localization of Crz1 mutants

	22°C	37°C	GlcN	NaCl		$CaCl_2$	FK506		42°C		42°C + FK506	
Strain	N	N	N	N	G	N	N	G	N	G	N	G
WT	13%	99%	78%	1%	99%	97%	0%	5%	0%	100%	0%	100%
7S -> A	37%	100%	96%	0%	100%	100%	1%	0%	100%	0%	0%	100%
polyQ -> A	11%	32%	94%	0%	100%	98%	2%	2%	0%	100%	0%	92%
ΔN 1-257	74%	95%	99%	10%	90%	100%	0%	4%	51%	36%	1%	57%
ΔN 1-368	92%	100%	97%	100%	90%	97%	95%	0%	97%	0%	99%	0%
ΔN 1-451	100%	100%	100%	15%	85%	98%	2%	0%	100%	0%	13%	87%
ΔN 1-705	54%	87%	87%	100%	23%	100%	91%	0%	100%	0%	100%	0%
ΔN 1-802	100%	100%	62%	100%	100%	98%	94%	0%	100%	0%	95%	0%
ΔN 1-823	97%	100%	100%	97%	94%	100%	85%	0%	91%	0%	100%	0%
ΔN 946-1030	85%	94%	52%	100%	0%	98%	84%	0%	100%	0%	96%	0%
ΔN 833-926	73%	98%	100%	100%	100%	100%	100%	0%	100%	0%	100%	0%
ΔN 625-665	23%	82%	97%	5%	84%	85%	0%	23%	17%	0%	0%	20%

% Different from WT

0-20
>20
>40
>60
>80
100

N: nuclear, G: Granular

Table 2.2. Strains, plasmids, and primers used

***C. neoformans* strain name**	**Identifier**	**Reference**
H99α	H99α	[37]
crz1Δ	H99α, *CRZ1*::*NAT*^{r}	FGSC deletion set Plate 5 Well A7
BC402	H99α, *CRZ1*::*NAT*^{r}, P$_{GPD1}$-*CRZ1*-mNeonGreen-*NEO*^{r}	This Study
XX510	H99α, *CRZ1*::*NAT*^{r}, P$_{GPD1}$-mCherry-*CRZ1*-*NEO*^{r}	[11]
BC948	H99α, *CRZ1*::*NAT*^{r}, P$_{GPD1}$-*CRZ1*(7S -> A)-mNeonGreen-*NEO*^{r}	This Study
BC979	H99α, *CRZ1*::*NAT*^{r}, P$_{GPD1}$-*CRZ1*(polyQ -> A)-mNeonGreen-*NEO*^{r}	This Study
BC982	H99α, *CRZ1*::*NAT*^{r}, P$_{GPD1}$-*CRZ1*(ΔN 1-257)-mNeonGreen-*NEO*^{r}	This Study
BC1212	H99α, *CRZ1*::*NAT*^{r}, P$_{GPD1}$-*CRZ1*(ΔN 833-926)-mNeonGreen-*NEO*^{r}	This Study
BC1245	H99α, *CRZ1*::*NAT*^{r}, P$_{GPD1}$-*CRZ1*(ΔN 625-665)-mNeonGreen-*NEO*^{r}	This Study
BC1249	H99α, *CRZ1*::*NAT*^{r}, P$_{GPD1}$-*CRZ1*(ΔN 946-1030)-mNeonGreen-*NEO*^{r}	This Study
BC1252	H99α, *CRZ1*::*NAT*^{r}, P$_{GPD1}$-*CRZ1*(ΔN 1-802)-mNeonGreen-*NEO*^{r}	This Study
BC1256	H99α, *CRZ1*::*NAT*^{r}, P$_{GPD1}$-*CRZ1*(ΔN 1-451)-mNeonGreen-*NEO*^{r}	This Study
BC1258	H99α, *CRZ1*::*NAT*^{r}, P$_{GPD1}$-*CRZ1*(ΔN 1-705)-mNeonGreen-*NEO*^{r}	This Study

BC1259	H99α, *CRZ1*::*NAT*^{r}, P$_{GPD1}$-*CRZ1*(ΔN 1-823)-mNeonGreen-*NEO*^{r}	This Study
BC1273	H99α, *CRZ1*::*NAT*^{r}, P$_{GPD1}$-*CRZ1*(ΔN 1-368)-mNeonGreen-*NEO*^{r}	This Study
BC1310	H99α, *CRZ1*::*NAT*^{r}, P$_{GPD1}$-*CRZ1*(ΔN 263-451)-mNeonGreen-*NEO*^{r}	This Study
Plasmid name	**Identifier**	**Reference**
pXL1-mCherry-*CRZ1*	P$_{GPD1}$-mCherry-*CRZ1-NEO*^{r}	[11]
pUC19-*CRZ1*-mNeonGreen	P$_{GPD1}$-*CRZ1*-mNeonGreen-*NEO*^{r}	This Study
LKB39	P$_{H3}$-GFP-*CNA1-NAT*^{r}	[22]
LKB61	P$_{GPD1}$-mCherry-*CNA1-HYG*^{r}	[22]
LKB88	P$_{GPD1}$-mCherry-*PUB1-HYG*^{r}	[22]
Primer name	**Sequence (5'-> 3')**	**Purpose**
linlab3397/XX	taatggccggccatggcagatccagcctcacc	Cloning WT *CRZ1* open reading frame
linlab3398/XX	taatgcgatcgcatcctcttcactcgtttcactcttc	Cloning WT *CRZ1* open reading frame
Linlab7530/BC	agcggcagcggcagcggcagcggcagcggcagctggtggctgaccctcacttgc	Generate polyQ mutant
Linlab7953/BC	tgtcctggtgagtcaccctgtggtcaagaatgtgctatcaca	Generate DBD mutant
Linlab7954/BC	acagggtgactcaccaggaca	Generate DBD mutant
Linlab7761/BC	cacttctgtcgctacgctggtgcaagaactcggcgctg	Generate Δ833-926 mutant
Linlab7762/BC	cagcgtagcgacagaagtg	Generate Δ833-926 mutant
Linlab7765/BC	ataggccggccggcttccacagttaaccaaacg	Generate Δ1-257 mutant
Linlab7955/BC	ataggccggccatgaccaaccctaactctccc	Generate Δ1-368 mutant
Linlab7956/BC	ataggccggccatgggcaggggactatttgacgc	Generate Δ1-451 mutant
Linlab7959/BC	ataggccggccatggggttatatcctcatgcg	Generate Δ1-705 mutant
Linlab7957/BC	ataggccggccgctggtggttcaacgtgag	Generate Δ1-823 mutant
Linlab7961/BC	caatcaaatgggatggaggatatgatctgtatccagcccagt	Generate Δ263-451 mutant

Linlab7958/BC	atcctccatcccatttgattg	Generate Δ263-451 mutant
Linlab7962/BC	gttgagctcgccttctcc	Generate Δ625-665 mutant
Linlab7963/BC	ggagaaggcgagctcaacttgcatcagctcactcaatta	Generate Δ625-665 mutant

CHAPTER 3

BIOLOGICAL ROLES OF CO_2 ON FUNGAL METABOLISM AND MORPHOLOGY

Benjamin J. Chadwick, Xiaorong Lin, to be submitted to Current Opinions in Microbiology, March, 2024

Abstract

Carbon dioxide is the 4th most abundant gas in the Earth's atmosphere. It supplies carbon for plants to harvest and is a major product of respiration. Inside the human body where CO_2 is constantly produced as a by-product of the TCA cycle, the percent CO_2 is ~5%. In the ambient atmosphere CO_2 only makes up ~.04% of the air. Through exhalation, CO_2 diffuses into the air causing gradients which can be sensed by other organisms including insects and microbes. CO_2 has beneficial impacts on the metabolism and behavior of all life. However, different organisms can tolerate different CO_2 levels to various degrees, and experiencing higher CO_2 than normally tolerated can be toxic and lead to death. The kingdom of fungi is notably a great model for studying variation in responses to CO_2 as CO_2 effects on growth rate, morphology, sporulation and germination, metabolism, and virulence have all been observed and vary in degree depending on the organism and species. There are a great number of studies and observations on CO_2 effects in fungi from different researchers and time periods, but limited connections have been made between them which could help infer new hypotheses and conclusions. This literature review focuses on the effects of CO_2 on metabolism and morphology. CO_2 tolerance and its role in *Cryptococcus neoformans* pathogenesis will be addressed in the final chapter.

Effect of CO_2 on metabolism

CO_2 has appeared essential for the growth of both prokaryotic and eukaryotic microbes, but the effects of CO_2 are difficult to differentiate from its indirect effects, such as reducing oxygen pressure, altering environment pH, or enhancing moisture retention. Until Wood and Werkman first reported the fixation of CO_2 by a heterotrophic microbe, it was thought that CO_2 fixation was specific to photosynthetic organisms[1]. In 1918, it was observed that growth of *Mycobacterium tuberculosis* was inhibited in the absence of CO_2, and entered a nonreproductive

but viable state [2]. Similar observations of a CO_2 requirement have been made for fungal organisms. For example, it was observed that CO_2 containing air is critical for the growth of the filamentous fungus *Aspergillus niger*, and by using C14 radiolabeled CO_2, researchers found carbon from CO_2 is incorporated into organic acids and this process is dependent on trace elements such as magnesium or manganese[3-5]. This observation that carbon from CO_2 is incorporated into organic acids in the cell, such as citrate, oxalacetate, fumarate, and succinate has been numerously reported [4,6-13]. A common observation from these studies was oxalic acid commonly being the major product from assimilated CO_2. Oxalacetate and the other organic acids found to be produced from CO_2 are important compounds for supplying the TCA cycle. In multiple studies, inclusion of a nitrogen source for the fungi resulted in additional incorporation of carbon from CO_2 into amino acids glutamate, aspartate, arginine, and isoleucine, which are known amino acids to be synthesized from TCA intermediates. Additionally, carbon from radiolabeled bicarbonate (HCO_3^-, a product of CO_2) assimilates into primarily amino acids [14]. Taken together, fungi may utilize CO_2 as a vital energy source for both supplying the TCA cycle and amino acid biosynthesis.

Interestingly, while *A. niger* conidia assimilated CO_2 into organic acids, the germinated spores were found to mostly incorporate the carbon into ATP and nucleic acids with preference for adenine, cytosine, and uracil [15]. Similarly, in the bean rust pathogen *Uromyces phaseoli*, CO_2 was found to be consistently incorporated into nucleic acids, with the greatest rate being 30 minutes after germination on host tissue [16]. These observations indicate there are multiple pathways for CO_2 assimilation, and preference for which pathway to utilize depends on the developmental status and culturing condition of the fungus.

Some hints for how CO_2 may be incorporated into nucleic acids come from genetic studies in *Neurospora crassa*. In the 1960s, *N. crassa* mutants which require high CO_2 for growth were characterized by H.P. Charles [17-20]. When testing the growth of these mutants under various nutrient conditions, it was found they behave like auxotrophic strains on minimal media but could show some growth when supplemented with nutrients like arginine, uridine, or succinate. Interestingly, these are all nutrients previously found to be assimilated from carbon in CO_2. One of these mutants was a pyrimidine mutant *pyr-3*, which on minimal media could grow with uridine supplementation, or surprisingly with supplementation of 20-30% CO_2. Curiously, when arginine was supplemented in the media, CO_2 was not able to rescue growth of the mutant. An arginine mutant, *arg-3*, displayed the opposite phenotype. It was able to grow on minimal media supplemented with arginine, or with 20-30% CO_2, but inhibited by uridine. Based on studies discussed above, CO_2 may be utilized for synthesis of pyrimidine nucleic acids including uracil, which is known to be catalyzed by the enzyme carbamoyl phosphate synthetase. Interestingly, carbamoyl phosphate is also a precursor for arginine. By adding exogenous CO_2 to the fungal cultures, carbamoyl phosphate synthetase may be able to help synthesize uridine required by the pyrimidine mutant. However, supplementing the pyrimidine mutant with arginine, another product downstream of carbamoyl phosphate, is possibly inhibiting growth through negative feedback or repressing carbamoyl phosphate synthetase. The opposite would also explain the phenotypes of the *arg-3* mutant.

A similar study was performed for mutants of the *ad-3* locus, which appear purple on solid media. The *ad-3* locus contained genes *ad-3A* and *ad-3B*, known to be responsible for the two step process of converting 5-aminoimidazole ribonucleotide (AIR) to 4-carboxy-5-aminoimidazole ribonucleotide (CAIR) to phosphoribosylaminoimidazole succinocarboxamide

(SAICAIR), essential for purine biosynthesis. However, it was unknown at the time which gene was responsible for which step of the AIR -> SAICAIR reaction. Interestingly, it was found that the adenine mutant, *ad-3B*, but not *ad-3A* required high levels of CO_2 for growth [21]. Because the reaction of AIR to CAIR involves CO_2, it was determined that *ad-3B* likely encodes for the enzyme synthesizing CAIR. This was later confirmed in biochemical studies of the same *ad-3A* and *ad-3B* mutants [22].

Similar high CO_2 requiring (HCR) mutants were identified in other species, including fungi and bacteria [23-25]. The most well-known HCR mutation is a loss of function of carbonic anhydrase (CA), which has been observed in multiple organisms [26-32]. Conversion of CO_2 to HCO_3^- is essential for cells, emphasizing the importance of CO_2 for growth in general. However, in high CO_2 environments this reaction sufficiently occurs spontaneously to support growth. Many organisms contain more than one CA gene, including the fungi *Cryptococcus* and *Aspergillus*. In these organisms, only one CA is the major enzyme which is essential for growth at ambient air [30,31]. Interestingly, in *A. nidulans*, the minor carbonic anhydrase, CA1, was found to be significantly differentially expressed when grown on different levels of potassium sources, but not CA2 which specifically responded to CO_2 levels [31]. Why some fungi have multiple carbonic anhydrases and what their different biological functions are remain open questions. While HCR mutants have been identified previously, there has since been no study aimed to identify and characterize high CO_2 requiring mutants. With increasing numbers of genetically tractable organisms and strategies for genetic screens, studies to identify and characterize high CO_2 requiring mutants would be a powerful strategy for further understanding the effect of CO_2 on fungal metabolism and biology.

Effect of CO_2 on Morphology

Besides effecting growth, early observations of CO_2 effects on fungi include influence on differentiation and morphological development. For example, researchers found that corn rot pathogen *Basiporium gallarum* would sporulate in the presence of plant tissue but not *in vitro* [33]. They hypothesized that the CO_2 from plant tissue may stimulate sporulation and found this to be the case after testing supplementing air with 1-5% CO_2. Consistently, sporulation was inhibited in this environment when barium hydroxide was added, which reacts with the CO_2 to produce carbonate. The effect of CO_2 on sporulation has been observed numerous times since then [34-38]. For different fungal strains, there is likely an optimal concentration of CO_2 which induces sporulation. In *N. crassa*, which displays a circadian rhythm in conidiation, conidiation is inhibited in CO_2 levels over 0.125% [39]. However, conidiation in the mutant called *band* (*bd*, named after conidial bands observed in a race tube assay to display circadian rhythm)[40] is not inhibited unless 25% of the air is CO_2. The mutation in the *bd* strain was later found to be a single nucleotide polymorphism (SNP) in ras-1, a widely conserved G-protein involved in mating, cell cycle regulation, and other signaling cascades [41-43]. This SNP led to a dominant form of ras-1 which is slightly increased for GTP exchange and likely enhances signal transduction. The mechanism behind the *bd* mutant's altered CO_2 sensing remains unknown. Because the *bd* mutant is more resistant to CO_2's inhibition of conidiation, it is possible that Ras1 signaling is antagonistic to the effect of CO_2.

In dimorphic fungi CO_2 may greatly impact the morphological transition between yeast and hyphae. In the 1800s, researchers had observed dimorphism of *Mucor* species, finding filamentous cells in aerobic conditions and yeast cells under low air conditions. It was thought that this was due to low oxygen concentrations [44]. However, in 1961 Bartnicki-Garcia and Nickerson et al., showed that *Mucour rouxii*'s yeast-like growth was stimulated by CO_2 and not

low oxygen [44]. When oxygen was replaced with CO_2, *M. rouxii* grew as spherical cells 10-50µm in diameter. When oxygen was replaced with N_2, *M. rouxii* grew as mycelium. The researchers found that this CO_2 effect on morphology was present for several other species of *Mucor*, but not for the *Rhizopus* species they tested (both members of the *Mucormycota* phylum). Similar to the effect of CO_2 observed in many mushrooms, yeast-like growth induced by CO_2 also inhibits fruiting body development (a result of filamentous growth) [45-49].

CO_2/HCO_3^- sensing impacts morphological developments

The model basidiomycete and dimorphic fungus *Cryptococcus neoformans* is normally observed as a yeast when grown in laboratory conditions, and filamentous growth is associated with cell fusion and mating. Interestingly, high CO_2/HCO_3^- was shown to completely inhibit mating by blocking cell fusion between opposite mating type cells leading to yeast cell growth [30]. Loss of the major carbonic anhydrase Can2 was able to rescue cell fusion and filamentation, but not fruiting body development and sporulation. Because cell fusion is controlled by pheromone signaling, the authors tested if their observations were due to altered regulation of pheromone. Indeed, they found that high CO_2 represses pheromone expression which is restored by loss of Can2. Additionally, a mutant known to overproduce pheromone, *hog1*Δ, was also able to mate in high CO_2. A possible explanation for these results is that CO_2/ HCO_3^- inhibition of pheromone inhibits mating, and loss of Can2 is able to reduce the amount of intracellular bicarbonate enough to allow for cell fusion and hyphal growth but not enough for fruiting. Further research is needed to determine the exact roles of HCO_3^- in mating. Whether or not CO_2/HCO_3^- inhibits the later stages of mating in WT crosses could be determined by shifting cells into a high CO_2 environment after cell fusion has already taken place. In another study, CO_2 was also found to inhibit mating of *Cryptococcus gattii*, a species closely related to *C. neoformans* [50]. However, the

mating defect could not be rescued by deletion of *CAN2*. However, it was also found that CO_2 stimulates filamentous growth of *C. gattii* when a mating partner is not present. Further research is needed to explain this combination of results, which involves complex interactions between CO_2, filamentation, and pheromone signaling pathways.

Multiple interacting pathways have been identified to regulate CO_2 induced morphological transitions. Klengel et al. provided the first evidence that bicarbonate mediated activation of the adenylyl cyclase-cAMP pathway induces hyphal growth in *C. albicans*. They showed that the catalytic domain of adenylyl cyclase is activated by HCO_3^- and this domain alone is sufficient to drive filamentation [51]. The researchers found that *C. neoformans* adenylyl cyclase is activated by HCO_3^- as well. Regulation of adenylyl cyclase by HCO_3^- and the presence of a putative bicarbonate binding site was originally identified in studies of cyanobacteria soluble adenylyl cyclase [52,53]. Mutation of the same binding site in *C. albicans* adenylyl cyclase leads to inability to respond to HCO_3^-, suggesting that the fungal adenylyl cyclase is also of the soluble type related to cyanobacteria [54]. This differs from most mammalian adenylyl cyclase enzymes which are membrane bound and do not interact with bicarbonate. For example, the Human genome encodes for 10 adenylyl cyclases, 9 of which are membrane bound [55]. The single Human soluble adenylyl cyclase indeed has similarity to cyanobacteria adenylyl cyclase, and is active in sperm cells and essential for cell fusion of gametes [31,55,56]. *S. cerevisiae*, *C. albicans*, and *C. neoformans* only contain one adenylyl cyclase. Current evidence suggests that the adenylyl cyclase in these organisms localizes mainly to membrane compartments [57-59]. Thus, it appears that the fungal adenylyl cyclases are intermediates, sharing the bacterial feature of a bicarbonate binding site while associated with membranes as the majority of adenylyl cycalses in mammals do. Further research on the evolution of adenylyl cyclase in fungi and

implications for their function would be valuable for understanding how fungi can differentiate $CO_2/HCO3^-$ from other stresses.

Additional research on bicarbonate signaling focused on identifying downstream effectors of the pathway. To identify genes regulated by carbonic anhydrase, one study in *C. neoformans* used the inducible promoter of *CTR4* to induce or repress *CAN2* expression for comparative transcriptomics [60]. The researchers identified many candidate genes regulated by *CAN2* involved in various stress response pathways, including the Gβ-subunit of the pheromone pathway important for sexual reproduction. However, there was not further investigation into the connection between CO_2 and the pheromone pathway. Another gene regulated by *CAN2* is the transcription factor Atf1. Atf1 is important for growth under oxidative stress, antifungals, and multiple other stresses. Whether this transcription factor is related to pheromone or CO_2 signaling has not been determined.

Through screening deletion mutants in *C. albicans*, a bZIP transcription factor termed Rca1 was found to negatively regulate transcript and protein expression of carbonic anhydrase in response to high CO_2 (regulator of carbonic anhydrase 1) [61], similar to the *S. cerevisiae* ortholog Cst6. Rca1 binds to the promoter of the carbonic anhydrase gene, *NCE103*, in response to high CO_2. Additionally, *RCA1* deletion reduces filamentation in 5% CO_2. These results suggest that Rca1 is a critical factor in a negative feedback loop to downregulate carbonic anhydrase in response to high CO_2, allowing for filamentous growth. While expression of *RCA1* in *C. albicans* is upregulated in high CO_2, expression of the *Candida glabrata RCA1* ortholog is not, despite the fact that it also regulates carbonic anhydrase [62]. In contrast to *C. albicans*, *C. glabrata* is mostly only found in the yeast form and only pseudohyphae is weakly induced by high CO_2 [63].

It is possible that differences between the two species in this aspect are partially due to Rca1 regulation.

Sch9 in *S. cerevisiae* is a potential kinase of Cst6 (Rca1 ortholog). It co-immunoprecipitates with and phosphorylates Cst6 *in vitro* [64].Deletion of *SCH9* causes loss of carbonic anhydrase repression in high CO_2 and Sch9 regulation of carbonic anhydrase is conserved in both *Saccharomyces* and *Candida* species. In response to changes in sphingolipid composition in membranes, Sch9 itself is regulated through phosphorylation by TOR and Pkh1/2 [65,66]. In response to high CO_2, deletion of TOR and especially Pkh1/2, or mutation of Pkh1/2's known phosphorylation sites on Sch9, reduces regulation of carbonic anhydrase [64]. How CO_2 initially activates this signaling pathway remains unknown. As bicarbonate is a known precursor for lipid biosynthesis, it is likely that high CO_2 changes membrane lipid composition and activates Pkh1/2 in this way. As no Cts6/Rca1 ortholog has been identified outside of *Candida* and *Saccharomyces*, it is currently unclear how CO_2 sensing by carbonic anhydrase is regulated in other organisms.

The role of CO_2 in *Candida albicans* morphological development

Most of the genetics and mechanistic studies on the effects of CO_2 on fungal biology comes from research on the human gut commensal and opportunistic fungal pathogen *Candida albicans*. In contrast to other fungi, CO_2 stimulates filamentous growth of *C. albicans*. Varying CO_2 levels impact *C. albicans* morphology likely because this fungus could be isolated from the high CO_2 environment of the gastrointestinal tract (possibly >20% CO_2), from blood and organs in a disseminated infection (~5% CO_2), or from skin in a superficial infection (closer to ambient air CO_2). In 20% CO_2, researchers have identified at least 12 different morphologies of *C. albicans*, and differentiation into these morphologies depends on the nutrient availability [67].

Regulation of Ume6 mediated filamentation and a new CO_2 sensing pathway

The transition from yeast to hypha in *C. albicans* is dependent on numerous environmental factors, including temperature, pH, nutrition availability, oxygen levels, and CO_2 levels [68]. Once filamentation is established, Ume6 is a key transcription factor which responds to changes in environmental conditions and maintains hyphal elongation [69]. In filamentation inducing conditions, such as low temperature and nutrient availability, Ume6 binds to its own promoter and positively regulates itself. When there is high nutrient availability or temperature, cAMP and TOR signaling pathways allow for expression of the repressor Nrg1 to repress *UME6* transcription [70,71]. *NRG1* is regulated by transcription factor Brg1, which induces chromatin remodeling initiated by the histone deacetylase Hda1 [71]. Consistent with the idea that Ume6 is downstream of these factors in maintaining filamentation, overexpression of Ume6 is able restore defects in hyphal elongation in *brg1* and *hda1* knockout mutants.

Interestingly, disrupting the chromatin remodeling pathway does not inhibit hyphal elongation when cells are cultured in hypoxia + 5% CO_2 [72]. Furthermore, deletion of *UME6* blocked hyphal elongation in the same conditions. Apparently, low oxygen and high CO_2 levels stabilize Ume6 protein and the G1 cyclin Hgc1, which is essential for filamentation and is unstable in normal air conditions[73]. The conserved regulator for hypoxia response in fungi is Sre1, homolog of mammalian sterol regulatory element binding protein (SREBP)[74] that resides on the ER membrane. In response to low oxygen levels, the N-terminal domain is proteolytically cleaved and translocates to the nucleus to act as a transcription factor. In fission yeast, Sre1N is degraded by the 2-OG-Fe(II) dioxygenase Ofd1 when cells are shifted from a hypoxic to aerobic environment [75]. Like Sre1, Ume6 was stabilized even in normal oxygen conditions when *OFD1* was deleted. However, the role of Ofd1 in Ume6 degradation is only relevant to oxygen levels

and not CO_2 levels. In 2019, Lu et al., identified two E3 ubiquitin ligases responsible for Ume6 and Hgc1 degradation: oxygen-responsive Ubr1 and CO_2-responsive Grr1. While Ubr1 degradation of Ume6 is mediated by Ofd1, how Grr1 degradation of Ume6 is regulated by CO_2 remains unknown. To identify how CO_2 leads to stabilization of Ume6, the authors screened ~3,000 knockout mutants for genes important for hyphal growth under hypoxia and 5% CO_2. They identified a phosphatase encoding gene *PTC2*. Interestingly, the *ptc2*Δ mutant cannot filament in 5% CO_2, but can filament in 5% CO_2 + hypoxia. Furthermore, Ume6 is not as stable in the *ptc2*Δ mutant under these filamentation inducing conditions. In the same screen of kinase mutants, the authors also found Ssn3. Phosphorylation of Ume6 by Ssn3 is required for degradation of Ume6 in atmospheric CO_2, and Ssn3 activity itself was regulated by Ptc2 phosphatase activity.

A remaining question from these studies was how CO_2 is sensed to start signal transduction of this pathway. In 2022, the same research group found that Ptc2 dynamically aggregates in cells in response to 5% CO_2 [76]. Ptc2 protein aggregates *in vitro* in response to CO_2, but not $HCO3^-$, suggesting CO_2 itself is causing the aggregation of Ptc2. The intrinsic disordered region (IDR) within Ptc2 accounts for the ability to form aggregates and these features of Ptc2, including phase separation in response to CO_2, are conserved for Ptc2 homologs found in *C. neoformans*, *S. cerevisiae*, and *Arabidopsis thaliana.* In addition to regulation of Ume6, the researchers also showed that Ptc2 dephosphorylates a regulator of the white-to-opaque switch, Wor1, in response to 5% CO_2. The authors further showed that CO_2 induction of the morphological switch and CA expression in *C. neoformans*, *C. albicans*, and *S. cerevisiae* were all dependent on the IDR of Ptc2. Together, these results implicate Ptc2 as a key regulator of CO_2 responses in fungi and other organisms as well. Whether or not Ptc2 condensates are

required to regulate stability of Ume6 has yet to be determined. An additional question is how CO_2 sensing through Ptc2 is balanced with CO_2 sensing through HCO_3^-. Do the CO_2 induced aggregates *in vivo* contain Ptc2 alone or additional proteins, such as CA?. As CO_2 interaction with Ptc2 is likely through a serine/threonine-rich sequence within the IDR, it would be interesting to test if IDRs containing this sequence are in other proteins and are also CO_2 responsive. The *S. cerevisiae* GFP collection would be a potential resource to test this hypothesis[77].

The effect of CO_2 on white-to-opaque switching in *Candida albicans*

CO_2 also regulates the white-to-opaque switch in *C. albicans*, a morphological transition associated with mating. 5% CO_2 enhances the frequency of the switch to the opaque state by close to 16-fold, and 20% CO_2 induces the switch by up to 105-fold [78]. Interestingly, CO_2 induction of the white-to-opaque switch is independent of the known CO_2 sensing pathway involving adenylyl cyclase activation and cAMP production [78,79]. Similar to the *bd* mutation in *N. crassa*, mutation of *RAS1* reduced sensitivity to CO_2 of the white-to-opaque switch, suggesting Ras1 is a conserved element in CO_2 signaling [78]. Later, the transcription factor Flo8 was found to be required for the white-to-opaque switch in 5% CO_2. Expression of Flo8 was induced by 5% CO_2, and constitutive overexpression of Flo8 caused hypersensitivity, with only 1% CO_2 needed for a 100% switch to the opaque state [79]. The upstream signaling in this pathway has yet to be determined. In the previously identified CO_2 sensing pathway, the conversion of CO_2 to bicarbonate is a critical step to activate adenylyl cyclase. This reaction could also lead to intracellular acidification, which. may explain the CO_2 effect on white-to-opaque differentiation. Consistent with this idea, keeping cells on low pH media (4-5) induces switching while high pH media (6-8) reduces it [80]. Additionally, the effect of pH on the morphological switch was

partially dependent on Rim101, a transcription factor known to be involved in alkaline stress response [81]. Regardless of the media pH, however, the addition of CO_2 had a dramatic influence on the white-to-opaque switch, suggesting intracellular acidification by CO_2 is just one factor responsible for inducing this morphological transition.

Conclusions

Here I described the numerous effects of CO_2 on fungal metabolism and morphology, and how CO_2 is sensed in fungal cells. To conclude, I have created a model to summarize what is known about how CO_2 is sensed in fungal cells (Figure 3.1). First, CO_2 diffuses across biological membranes through passive diffusion. There is evidence for the existence of CO_2 transporters in other organisms, including aquaporins and rhesus membrane proteins, but this has not been shown in fungi [82,83]. Notably, knockout of aquaporins in *C. neoformans* did not affect viability in 5% CO_2 (unpublished results from myself and Y-S Bahn [82]). However, the role of potential CO_2 transporters may be best to test in *C. albicans*, where different levels of CO_2 have different and more defined quantitative effects on filamentation. Additionally, membrane and cell wall components may influence CO_2 diffusion through cells, and this may alter the concentration needed to observe CO_2 effects [83]. Second, CO_2 is converted to bicarbonate with the help of CA, causing intracellular acidification. Third, HCO_3^- activates adenylyl cyclase leading to cAMP production. Fourth, HCO_3^- is utilized to produce malonyl-CoA, critical for fatty acid biosynthesis. Fifth, high concentrations of CO_2 directly interfere with metabolic reactions in the cell, such as those in the TCA cycle and pyrimidine biosynthesis. Sixth, CO_2 directly interacts with proteins such as Ptc2, causing aggregates to form and stimulates signaling transduction possibly through controlling protein localization. In conclusion, CO_2 has many physiological

effects on fungal cells which is reflected in the diversity of responses to CO_2 observed in the kingdom of fungi.

References

1. Wood, H.G., Werkman, C.H., Hemingway, A. & Nier, A.O. Heavy Carbon as a tracer in hetertrophic carbon dioxide assimilation *Journal of Biological Chemistry* **139**, 365-376 (1941).
2. Wherry, W.B. & Ervin, D.M. The Necessity of Carbon Dioxid for the Growth of *B. Tuberculosis*. *The Journal of Infectious Diseases* **22**, 194-197 (1918).
3. Woronick, C.L. & Johnson, M.J. Carbon Dioxide Fixation by Cell-free Extracts of *Aspergillus niger*. *Journal of Biological Chemistry* **235**, 9-15 (1960).
4. Lewis, K.F. & Weinhouse, S. Assimilation of Carbon Dioxide in Oxalate and Citrate by *Aspergillus Niger*. *Journal of the American Chemical Society* **73**, 2906-2909 (1951).
5. Steinberg, R.A. Influence of Carbon Dioxide on Response of *Aspergillus niger* to Trace Elements. *Plant Physiology* **17**, 129-132 (1942).
6. Harley, J.L. Incorporation of Carbon Dioxide into Excised Beech Mycorrhizas in the Presence and Absence of Ammonia. *The New Phytologist* **63**, 203-208 (1964).
7. Heplar, J.Q. & Tatum, E.L. Some factors affecting carbon dioxide metabolism in *neurospora crassa*. *J Biol Chem* **208**, 489-94 (1954).
8. Keen, R.E.H.a.N.T. Enzymes Catalyzing Anaplerotic Carbon Dioxide Fixation in *Verticillium albo-atrum*. *Phytopathology*, 947-953 (1973).
9. Rick, P.D. & Mirocha, C.J. Fixation of Carbon Dioxide in the Dark by the Malic Enzyme of Bean and Oat Stem Rust Uredospores. *Plant Physiology* **43**, 201-207 (1968).
10. Staples, R.C. & Weinstein, L.H. Dark carbon dioxide fixation by uredospores of rust fungi. *Contrib. Boyce Thompson Inst* **20**, 71-82 (1959).
11. Gitterman, C.O. & Knight, S.G. Carbon dioxide fixation into amino acids of *penicillium chrysogenum*. *J Bacteriol* **64**, 223-31 (1952).
12. Bachofen, R. & Rast, D. Carboxylierungsreaktionen in *Agaricus bisporus* III. Pyruvat und Phosphoenolpyruvat als CO2-Acceptoren. *Archiv für Mikrobiologie* **60**, 217-234 (1968).
13. Hartman, R.E., Keen, N.T. & Long, M. Carbon Dioxide Fixation by *Verticillium albo-atrum*. *Microbiology* **73**, 29-34 (1972).
14. Budd, K. The assimilation of bicarbonate by *Neocosmospora vasinfecta*. *Canadian Journal of Microbiology* **15**, 389-398 (1969).
15. Yanagita, T. Carbon dioxide fixation in germinating conidiospores of *Aspergillus niger The Journal of General and Applied Microbiology* **9**, 343-351 (1963).
16. Stallknecht, G. & Mirocha, C. Fixation and incorporation of CO2 into ribonucleic acid by germinating uredospores of *Uromyces phaseoli*. *Phytopathology* **61**, 400-405 (1971).
17. Charles, H.P. Response of *Neurospora* Mutants to Carbon Dioxide. *Nature* **195**, 359-360 (1962).
18. Charles, H.P. & Broadbent, J.A. Carbon Dioxide Mutants in *Neurospora*. *Nature* **201**, 1004-1006 (1964).

19. Charles, H.P. RELATIONSHIPS BETWEEN CERTAIN PYRIMIDINE AND ARGININE MUTANTS OF *NEUROSPORA*, AS REVEALED BY THEIR RESPONSE TO CARBON DIOXIDE. *J Gen Microbiol* **34**, 131-42 (1964).
20. BROADBENT, J.A. & CHARLES, H.P. Some Carbon-Dioxide Requiring Mutants of *Neurospora crassa*. *Microbiology* **39**, 63-74 (1965).
21. De Serres, F.J. Carbon dioxide stimulation of the AD-3 mutants of *Neurospora crassa*. *Mutat Res* **3**, 420-5 (1966).
22. Fisher, C.R. Phosphoribosyl-aminoimidazole-succinocarboxamide synthetase from *Neurospora crassa*: I. Partial purification and properties. *Biochimica et Biophysica Acta (BBA) - Enzymology* **178**, 380-388 (1969).
23. Charles, H.P. & Roberts, G.A. Carbon Dioxide as a Growth Factor for Mutants of *Escherichia coli*. *Microbiology* **51**, 211-224 (1968).
24. Roberts, G.A. & Charles, H.P. Mutants of *Neurospora crassa, Escherichia coli* and *Salmonella typhimurium* Specifically Inhibited by Carbon Dioxide. *Microbiology* **63**, 21-27 (1970).
25. Vivian, A. & Charles, H.P. The Occurrence and Genetics of Some CO2 Mutants in *Streptomyces coelicolor*. *Microbiology* **61**, 263-271 (1970).
26. Funke, R.P., Kovar, J.L. & Weeks, D.P. Intracellular carbonic anhydrase is essential to photosynthesis in *Chlamydomonas reinhardtii* at atmospheric levels of CO2. Demonstration via genomic complementation of the high-CO2-requiring mutant ca-1. *Plant Physiol* **114**, 237-44 (1997).
27. Götz, R., Gnann, A. & Zimmermann, F.K. Deletion of the carbonic anhydrase-like gene NCE103 of the yeast *Saccharomyces cerevisiae* causes an oxygen-sensitive growth defect. *Yeast* **15**, 855-864 (1999).
28. Kusian, B., Sültemeyer, D. & Bowien, B. Carbonic anhydrase is essential for growth of *Ralstonia eutropha* at ambient CO(2) concentrations. *J Bacteriol* **184**, 5018-26 (2002).
29. Mitsuhashi, S., Ohnishi, J., Hayashi, M. & Ikeda, M. A gene homologous to β-type carbonic anhydrase is essential for the growth of C*orynebacterium glutamicum* under atmospheric conditions. *Applied Microbiology and Biotechnology* **63**, 592-601 (2004).
30. Bahn, Y.-S., Cox, G.M., Perfect, J.R. & Heitman, J. Carbonic Anhydrase and CO_2 Sensing during *Cryptococcus neoformans* Growth, Differentiation, and Virulence. *Current Biology* **15**, 2013-2020 (2005).
31. Xiao, L., Lian, B., Dong, C. & Liu, F. The selective expression of carbonic anhydrase genes of *Aspergillus nidulans* in response to changes in mineral nutrition and CO2 concentration. *Microbiologyopen* **5**, 60-9 (2016).
32. Pérez-Etayo, L. *et al.* The CO(2)-dependence of *Brucella ovis* and *Brucella abortus* biovars is caused by defective carbonic anhydrases. *Vet Res* **49**, 85 (2018).
33. Durrell, L.W. Stimulation of Spore Germination by CO2. *Science* **60**, 499-499 (1924).
34. Vakil, J.R., Rao, M.R. & Bhattacharyya, P.K. Effect of CO2 on the germination of conidiospores of *Aspergillus niger*. *Arch Mikrobiol* **39**, 53-7 (1961).
35. Klironomos, J.N., Rillig, M.C., Allen, M.F., Zak, D.R., Pregitzer, K.S. & Kubiske, M.E. Increased levels of airborne fungal spores in response to *Populus tremuloides* grown under elevated atmospheric CO2. *Canadian Journal of Botany* **75**, 1670-1673 (1997).
36. Hayashi, M., Ohkuni, K. & Yamashita, I. An extracellular meiosis-promoting factor in *Saccharomyces cerevisiae*. *Yeast* **14**, 617-22 (1998).

37. Ohkuni, K., Hayashi, M. & Yamashita, I. Bicarbonate-mediated social communication stimulates meiosis and sporulation of *Saccharomyces cerevisiae*. *Yeast* **14**, 623-31 (1998).
38. Wolf, J., O'Neill, N.R., Rogers, C.A., Muilenberg, M.L. & Ziska, L.H. Elevated atmospheric carbon dioxide concentrations amplify *Alternaria alternata* sporulation and total antigen production. *Environ Health Perspect* **118**, 1223-8 (2010).
39. Sargent, M.L. & Kaltenborn, S.H. Effects of medium composition and carbon dioxide on circadian conidiation in *neurospora*. *Plant Physiol* **50**, 171-5 (1972).
40. Sargent, M.L. & Woodward, D.O. Genetic determinants of circadian rhythmicity in *Neurospora*. *J Bacteriol* **97**, 861-6 (1969).
41. Pentland, D.R., Piper-Brown, E., Mühlschlegel, F.A. & Gourlay, C.W. Ras signalling in pathogenic yeasts. *Microb Cell* **5**, 63-73 (2017).
42. Tamanoi, F. Ras signaling in yeast. *Genes Cancer* **2**, 210-5 (2011).
43. Mitin, N., Rossman, K.L. & Der, C.J. Signaling Interplay in Ras Superfamily Function. *Current Biology* **15**, R563-R574 (2005).
44. Bartnicki-Garcia, S. & Nickerson Walter, J. INDUCTION OF YEASTLIKE DEVELOPMENT IN MUCOR BY CARBON DIOXIDE. *Journal of Bacteriology* **84**, 829-840 (1962).
45. Baars, J.J.P., Scholtmeijer, K., Sonnenberg, A.S.M. & van Peer, A.V. Critical Factors Involved in Primordia Building in *Agaricus bisporus*: A Review. *Molecules* **25**(2020).
46. Sakamoto, Y. Influences of environmental factors on fruiting body induction, development and maturation in mushroom-forming fungi. *Fungal Biology Reviews* **32**, 236-248 (2018).
47. Eastwood, D.C., Herman, B., Noble, R., Dobrovin-Pennington, A., Sreenivasaprasad, S. & Burton, K.S. Environmental regulation of reproductive phase change in Agaricus bisporus by 1-octen-3-ol, temperature and CO2. *Fungal Genetics and Biology* **55**, 54-66 (2013).
48. Jang, K.-Y. *et al.* Characterization of Fruitbody Morphology on Various Environmental Conditions in *Pleurotus ostreatus*. *Mycobiology* **31**, 145-150 (2003).
49. Yan, J.J. *et al.* Comparative Transcriptomics of *Flammulina filiformis* Suggests a High CO(2) Concentration Inhibits Early Pileus Expansion by Decreasing Cell Division Control Pathways. *Int J Mol Sci* **20**(2019).
50. Ren, P., Chaturvedi, V. & Chaturvedi, S. Carbon dioxide is a powerful inducer of monokaryotic hyphae and spore development in *Cryptococcus gattii* and carbonic anhydrase activity is dispensable in this dimorphic transition. *PLoS One* **9**, e113147 (2014).
51. Klengel, T. *et al.* Fungal adenylyl cyclase integrates CO_2 sensing with cAMP signaling and virulence. *Current biology : CB* **15**, 2021-2026 (2005).
52. Cann, M.J., Hammer, A., Zhou, J. & Kanacher, T. A Defined Subset of Adenylyl Cyclases Is Regulated by Bicarbonate Ion. *Journal of Biological Chemistry* **278**, 35033-35038 (2003).
53. Steegborn, C., Litvin, T.N., Levin, L.R., Buck, J. & Wu, H. Bicarbonate activation of adenylyl cyclase via promotion of catalytic active site closure and metal recruitment. *Nat Struct Mol Biol* **12**, 32-7 (2005).
54. Hall, R.A. *et al.* CO(2) acts as a signalling molecule in populations of the fungal pathogen Candida albicans. *PLoS Pathog* **6**, e1001193 (2010).

55. Buffone, M.G., Wertheimer, E.V., Visconti, P.E. & Krapf, D. Central role of soluble adenylyl cyclase and cAMP in sperm physiology. *Biochimica et Biophysica Acta (BBA) - Molecular Basis of Disease* **1842**, 2610-2620 (2014).
56. Chen, Y. *et al.* Soluble adenylyl cyclase as an evolutionarily conserved bicarbonate sensor. *Science* **289**, 625-8 (2000).
57. Yee-Seul, S., Dong-Hoon, Y., Kwang-Woo, J. & Won-Ki, H. Molecular Characterization of Adenylyl Cyclase Complex Proteins Using Versatile Protein-Tagging Plasmid Systems in *Cryptococcus neoformans*. *Journal of Microbiology and Biotechnology* **27**, 357-364 (2017).
58. Belotti, F., Tisi, R., Paiardi, C., Rigamonti, M., Groppi, S. & Martegani, E. Localization of Ras signaling complex in budding yeast. *Biochimica et Biophysica Acta (BBA) - Molecular Cell Research* **1823**, 1208-1216 (2012).
59. Zeng, G. *et al.* Comprehensive Interactome Analysis for the Sole Adenylyl Cyclase Cyr1 of *Candida albicans*. *Microbiol Spectr* **10**, e0393422 (2022).
60. Kim, M.S., Ko, Y.J., Maeng, S., Floyd, A., Heitman, J. & Bahn, Y.S. Comparative transcriptome analysis of the CO2 sensing pathway via differential expression of carbonic anhydrase in *Cryptococcus neoformans*. *Genetics* **185**, 1207-19 (2010).
61. Cottier, F. *et al.* The bZIP transcription factor Rca1p is a central regulator of a novel CO_2 sensing pathway in yeast. *PLoS Pathog* **8**, e1002485 (2012).
62. Cottier, F. *et al.* Carbonic anhydrase regulation and CO2 sensing in the fungal pathogen *Candida glabrata* involves a novel Rca1p ortholog. *Bioorganic & Medicinal Chemistry* **21**, 1549-1554 (2013).
63. Sasani, E., Khodavaisy, S., Agha Kuchak Afshari, S., Darabian, S., Aala, F. & Rezaie, S. Pseudohyphae formation in *Candida glabrata* due to CO(2) exposure. *Curr Med Mycol* **2**, 49-52 (2016).
64. Pohlers, S. *et al.* Lipid Signaling via Pkh1/2 Regulates Fungal CO2 Sensing through the Kinase Sch9. *mBio* **8**(2017).
65. Yabuki, Y., Ikeda, A., Araki, M., Kajiwara, K., Mizuta, K. & Funato, K. Sphingolipid/Pkh1/2-TORC1/Sch9 Signaling Regulates Ribosome Biogenesis in Tunicamycin-Induced Stress Response in Yeast. *Genetics* **212**, 175-186 (2019).
66. Liu, K., Zhang, X., Lester, R.L. & Dickson, R.C. The Sphingoid Long Chain Base Phytosphingosine Activates AGC-type Protein Kinases in *Saccharomyces cerevisiae* Including Ypk1, Ypk2, and Sch9. *Journal of Biological Chemistry* **280**, 22679-22687 (2005).
67. Daniels, K.J., Pujol, C., Srikantha, T. & Soll, D.R. The "finger," a unique multicellular morphology of *Candida albicans* induced by CO2 and dependent upon the Ras1-cyclic AMP pathway. *Eukaryot Cell* **11**, 1257-67 (2012).
68. Chow, E.W.L., Pang, L.M. & Wang, Y. From Jekyll to Hyde: The Yeast-Hyphal Transition of *Candida albicans*. *Pathogens* **10**(2021).
69. Villa, S. *et al.* Transcriptional control of hyphal morphogenesis in *Candida albicans*. *FEMS Yeast Res* **20**(2020).
70. Lu, Y., Su, C., Wang, A. & Liu, H. Hyphal development in *Candida albicans* requires two temporally linked changes in promoter chromatin for initiation and maintenance. *PLoS Biol* **9**, e1001105 (2011).

71. Lu, Y., Su, C. & Liu, H. A GATA transcription factor recruits Hda1 in response to reduced Tor1 signaling to establish a hyphal chromatin state in *Candida albicans*. *PLoS Pathog* **8**, e1002663 (2012).
72. Lu, Y., Su, C., Solis, N.V., Filler, S.G. & Liu, H. Synergistic regulation of hyphal elongation by hypoxia, CO(2), and nutrient conditions controls the virulence of *Candida albicans*. *Cell Host Microbe* **14**, 499-509 (2013).
73. Wang, A., Lane, S., Tian, Z., Sharon, A., Hazan, I. & Liu, H. Temporal and spatial control of HGC1 expression results in Hgc1 localization to the apical cells of hyphae in *Candida albicans*. *Eukaryot Cell* **6**, 253-61 (2007).
74. Hughes, A.L., Todd, B.L. & Espenshade, P.J. SREBP pathway responds to sterols and functions as an oxygen sensor in fission yeast. *Cell* **120**, 831-42 (2005).
75. Hughes, B.T. & Espenshade, P.J. Oxygen-regulated degradation of fission yeast SREBP by Ofd1, a prolyl hydroxylase family member. *Embo j* **27**, 1491-501 (2008).
76. Zhang, M. *et al.* The intrinsically disordered region from PP2C phosphatases functions as a conserved CO_2 sensor. *Nature Cell Biology* **24**, 1029-1037 (2022).
77. Huh, W.K. *et al.* Global analysis of protein localization in budding yeast. *Nature* **425**, 686-91 (2003).
78. Huang, G., Srikantha, T., Sahni, N., Yi, S. & Soll, D.R. CO(2) regulates white-to-opaque switching in *Candida albicans*. *Curr Biol* **19**, 330-4 (2009).
79. Du, H. *et al.* The transcription factor Flo8 mediates CO_2 sensing in the human fungal pathogen *Candida albicans*. *Mol Biol Cell* **23**, 2692-701 (2012).
80. Sun, Y., Cao, C., Jia, W., Tao, L., Guan, G. & Huang, G. pH Regulates White-Opaque Switching and Sexual Mating in *Candida albicans*. *Eukaryot Cell* **14**, 1127-34 (2015).
81. Davis, D., Wilson, R.B. & Mitchell, A.P. RIM101-dependent and-independent pathways govern pH responses in *Candida albicans*. *Mol Cell Biol* **20**, 971-8 (2000).
82. Bahn, Y.S. & Mühlschlegel, F.A. CO_2 sensing in fungi and beyond. *Curr Opin Microbiol* **9**, 572-8 (2006).
83. Endeward, V., Arias-Hidalgo, M., Al-Samir, S. & Gros, G. CO_2 Permeability of Biological Membranes and Role of CO_2 Channels. *Membranes (Basel)* **7**(2017).

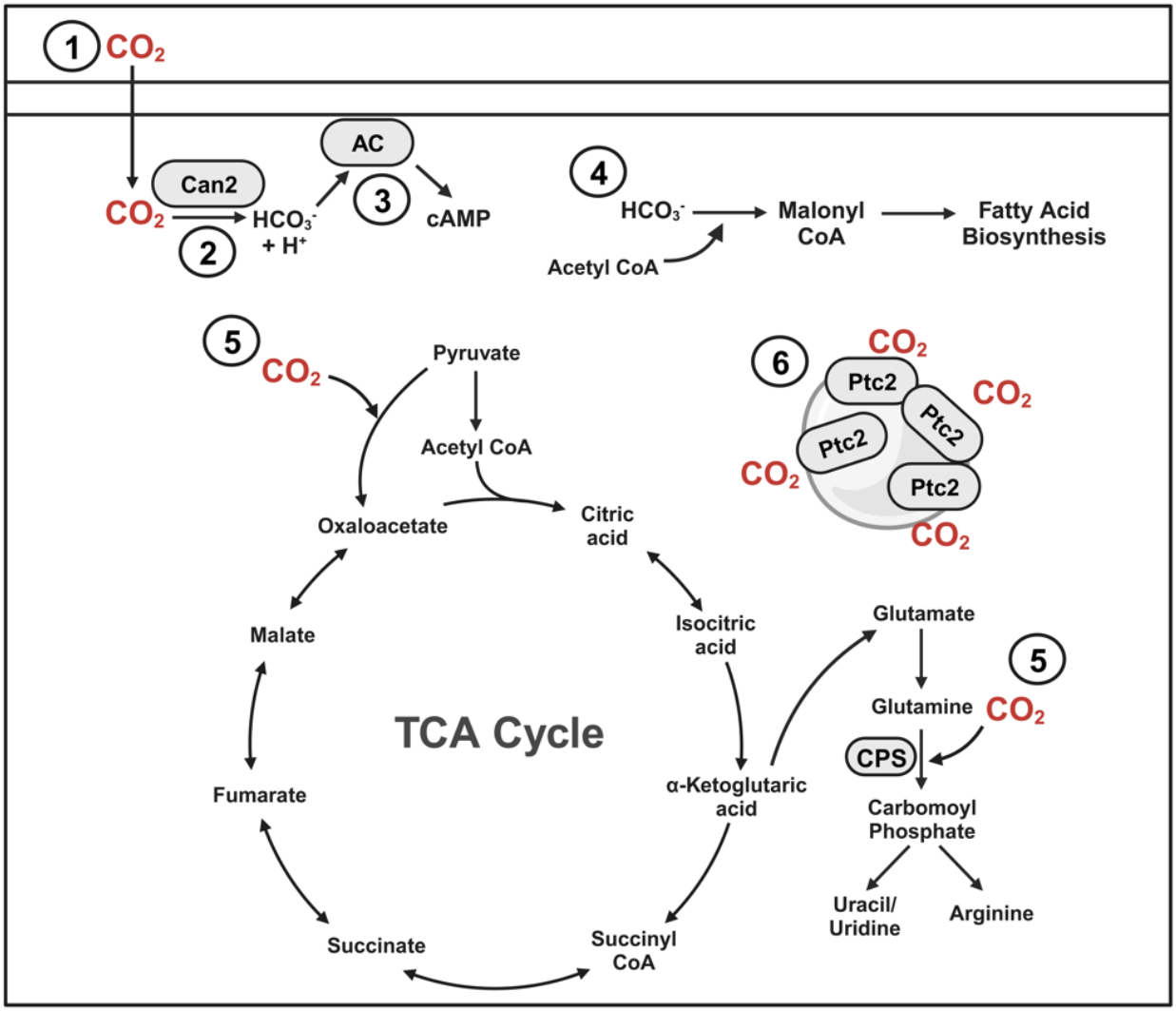

Figure 3.1. Schematic of CO_2 effects of fungal cells

1) CO_2 diffuses across biological membranes through passive diffusion. 2) CO_2 is converted to bicarbonate with the help of carbonic anhydrase, causing intracellular acidification through generating hydrogen ions. 3) HCO_3^- activates adenylyl cyclase leading to cAMP production. 4) HCO_3^- is utilized to produce malonyl-CoA, critical for fatty acid biosynthesis. 5) high concentrations of CO_2 directly interfere with metabolic reactions in the cell, such as those in the TCA cycle and pyrimidine biosynthesis. 6) CO_2 directly interacts with proteins such as Ptc2, causing aggregates to form and stimulates signaling transduction possibly through controlling protein localization.

CHAPTER 4

THE RAM PATHWAY LINKS MORPHOLOGY, THERMOTOLERANCE, AND CO_2 TOLERANCE IN THE GLOBAL FUNGAL PATHOGEN CRYPTOCOCCUS NEOFORMANS [3]

[3] Benjamin J. Chadwick, Tuyetnhu Pham, Xiaofeng Xie, Laura C. Ristow, Damian J. Krysan, and Xiaorong Lin. 2022. *eLife*, 11, e82563

Reprinted here with permission of the publisher.

Abstract

The environmental pathogen *Cryptococcus neoformans* claims over 180,000 lives each year. Survival of this basidiomycete at host CO_2 concentrations has only recently been considered an important virulence trait. Through screening gene knockout libraries constructed in a CO_2-tolerant clinical strain, we found mutations leading to CO_2 sensitivity are enriched in pathways activated by heat stress, including calcineurin, Ras1-Cdc24, cell wall integrity, and Regulator of Ace2 and Morphogenesis (RAM). Overexpression of Cbk1, the conserved terminal kinase of the RAM pathway, partially restored defects of these mutants at host CO_2 or temperature levels. In ascomycetes such as *Saccharomyces cerevisiae* and *Candida albicans*, transcription factor Ace2 is an important target of Cbk1, activating genes responsible for cell separation. However, no Ace2 homolog or any downstream component of the RAM pathway has been identified in basidiomycetes. Through *in vitro* evolution and comparative genomics, we characterized mutations in suppressors of *cbk1*Δ in *C. neoformans* that partially rescued defects in CO_2 tolerance, thermotolerance, and morphology. One suppressor is the RNA translation repressor Ssd1, which is highly conserved in ascomycetes and basidiomycetes. The other is a novel ribonuclease domain-containing protein, here named *PSC1*, which is present in basidiomycetes and humans but surprisingly absent in most ascomycetes. Loss of Ssd1 in *cbk1*Δ partially restored cryptococcal ability to survive and amplify in the inhalation and intravenous murine models of cryptococcosis. Our discoveries highlight the overlapping regulation of CO_2 tolerance and thermotolerance, the essential role of the RAM pathway in cryptococcal adaptation to the host condition, and the potential importance of post-transcriptional control of virulence traits in this global pathogen.

Introduction

There are over 278,000 cases of cryptococcal meningitis every year, causing over 180,000 deaths [1]. Cryptococcal meningitis is primarily caused by the ubiquitous environmental fungus *Cryptococcus neoformans.* Airborne spores or desiccated yeast cells of *C. neoformans* are inhaled into the lungs, where they are cleared or remain dormant until reactivation upon host immunosuppression [2,3].

Litvintseva et al. found that most environmental *Cryptococcus* isolates cannot cause fatal disease in mouse models of cryptococcosis, despite having similar genotypes and *in vitro* phenotypes to known virulent isolates, including thermotolerance, melanization, and capsule production [4]. Mukaremera et al. also observed that *in vitro* phenotype assays for thermotolerance, capsule production, titan cell formation, or fluconazole heteroresistance, could not differentiate high-virulence strains from low-virulence strains [5]. These observations raise the possibility that other, unidentified virulence traits are important for *Cryptococcus* pathogenesis. Tolerance to host levels of CO_2 (~5% CO_2 in the host vs. ~0.04% in ambient air) is likely a significant factor separating the potentially virulent natural isolates from the non-pathogenic environmental isolates that Litvintseva et al. tested [4,6].

The ability to adapt to host conditions is a prerequisite for cryptococcal pathogenesis. For instance, the ability of *C. neoformans* to replicate at human body temperature (≥37˚C) has been extensively investigated. Many genes have been shown to be essential for thermotolerance [7-9], including calcineurin which is currently being explored for antifungal drug development [10]. By contrast, the underlying mechanisms or genes that play a role in CO_2 tolerance have yet to be identified. Here, we set out to identify CO_2-sensitive mutants and to gain the first insight into the genetic components involved in CO_2 tolerance in *C. neoformans*.

Results

CO_2 sensitivity is independent of pH

Our previous work indicates that many *C. neoformans* environmental strains are sensitive to 5% CO_2 when grown on buffered RPMI media, commonly used for mammalian cell cultures and testing antifungal susceptibility [6]. CO_2 at host concentrations also acts synergistically with the commonly used antifungal drug fluconazole in inhibiting cryptococcal growth on buffered RPMI media. Because CO_2 lowers the pH of aqueous environments, it is possible that the CO_2 growth inhibitory effect or its synergy with fluconazole is simply due to lower medium pH. To address this question, we tested sensitivity to fluconazole of wild-type strain H99 using E-test on buffered RPMI media of either pH 6 or pH 7, with or without 5% CO_2. In this E-test, the size of halo (clearance zone) reflects fungal susceptibility to fluconazole. As shown in Figure 4.1A, clearance zones were much larger in 5% CO_2 relative to those in ambient air at both pH 6 and pH 7, indicating that CO_2 sensitizes cryptococcal susceptibility to fluconazole. Furthermore, CO_2 inhibits the growth of H99 at both pH 6 and pH 7 (smaller colony size in 5% CO_2 relative to that in ambient air). Additionally, growth of CO_2-sensitive environmental strain A7-35-23 [6] was severely inhibited by 5% CO_2 at both pH 6 and pH 7 (Figure 4.1B). In general, *C. neoformans* grows better at acidic pH (can grow well in pH 3), and both A7-35-23 and H99 grew better at pH 6 than at pH 7 in ambient air (Figure 4.1B). Taken together, these results suggest that cryptococcal growth inhibition by CO_2 is not simply due to lowered pH.

Identifying genes important for CO_2 tolerance

To identify genes involved in CO_2 tolerance in *C. neoformans*, we screened gene deletion mutants constructed in the CO_2-tolerant clinical reference strain H99. For large-scale screening, we used the nutrient rich YPD medium on which *C. neoformans* grows well. Accordingly, we

tested the growth of two CO_2-sensitive environmental strains and the CO_2-tolerant H99 strain in different levels of CO_2 when cultured on YPD. As expected, relative to H99, the CO_2-sensitive strains A7-35-23 and A1-38-2 grew poorly at 5% CO_2 and worse at 20% CO_2 (Figure 4.2A). Using this approach, the following deletion mutant libraries were screened at 20% CO_2 on YPD media: a set of strains previously constructed in our lab, the collections constructed by the Madhani lab, and a set generated in the Lodge Lab [11]. As some mutants are known to be temperature sensitive, we carried out the screens at 30˚C rather than 37˚C. From over 5,000 gene knockout mutants screened (~7000 protein coding genes in the H99 genome), 96 were found to be sensitive to CO_2 by visual observation (Table 3.1). We noticed that knockout mutants for multiple pathways known to be activated by heat stress are CO_2 sensitive, including the Ras1-Cdc24 pathway, calcineurin, cell wall integrity (CWI), and Regulator of Ace2 and Morphogenesis (RAM). This finding indicates an overlapping nature of these two traits.

In *Candida albicans*, the adenylyl cyclase pathway is crucial for the yeast-hypha transition in response to host levels of CO_2 [12]. This pathway has also been proposed to play an important role for *Cryptococcus* to sense CO_2, and the carbonic anhydrase Can1 is required for growth at low concentrations of CO_2 [13,14]. However, we found that adenylyl cyclase pathway mutants showed no growth defects at host levels CO_2, including the adenylyl cyclase mutant *cac1*Δ, the adenylyl cyclase associated protein mutant *aca1*Δ, the alpha G protein subunit mutant *gpa1*Δ, and the cAMP-dependent protein kinase mutant *pkr1*Δ (Figure S4.1). This indicates that growth defects in response to host levels of CO_2 are likely independent of bicarbonate activation of adenylyl cyclase. This is not unexpected given that bicarbonate is not a limiting factor under the high level of CO_2 used in our screen.

Because the calcineurin, Ras1-Cdc24, CWI, and RAM pathways are all activated at host temperature and were identified in our screen for CO_2-sensitive mutants, we reasoned their downstream effectors may be related or genetically interact. As the RAM pathway effector kinase mutant *cbk1*Δ showed the most severe defect in thermotolerance and CO_2 tolerance compared to the mutants of the other pathways, we first overexpressed the gene *CBK1* in the following mutants, *cdc24*Δ (Ras1-Cdc24), *mpk1*Δ (CWI), *cna1*Δ (Calcineurin), and the *cbk1*Δ mutant itself, and observed their growth at host temperature and host CO_2 (Figure 4.2B). Overexpression was achieved by placing the *CBK1* open reading frame after the inducible *CTR4* promoter, which is highly activated in YPD media [15-17]. The *CBK1* overexpression construct was specifically integrated into the "safe haven" locus *SH2* [18,19] in each mutant strain background to avoid complications due to positional effects. We additionally confirmed overexpression of *CBK1* by RT-PCR (Figure S4.2). As expected, the growth defects of the *cbk1*Δ mutant at 37˚C with and without 5% CO_2 were largely restored by *CBK1* overexpression. At 30˚C, overexpression of *CBK1* restored the growth of the *mpk1*Δ mutant, the *cna1*Δ mutant, and the *cdc24*Δ mutant in the CO_2 condition. In terms of thermotolerance, overexpression of *CBK1* restored growth of *mpk1*Δ but not *cna1*Δ, while the growth defect of *cdc24*Δ at 37˚C was exacerbated. *CBK1* overexpression failed to rescue growth of any of these mutants when both stressors were present (37˚C + 5% CO_2). We found that overexpression of *CBK1* in the WT H99 background caused a modest growth defect at 37˚C + 5% CO_2. Thus, the detrimental effects from *CBK1* overexpression under this growth condition may partially explain its inability to fully rescue growth of these tested CO_2-sensitive mutants. The reciprocal overexpression of *CDC24*, *MPK1*, or *CNA1* in the *cbk1*Δ mutant background did not restore growth under 37˚C and/or 5%

CO_2 (Figure S4.3). These results support a hypothesis that Cbk1 integrates multiple stress response pathways to regulate both CO_2 tolerance and thermotolerance.

To determine the extent of Cbk1's role in CO_2 tolerance, we conducted NanoString gene expression profiling of the WT H99 and *cbk1*Δ mutant cultured in ambient air and in 5% CO_2 at 30˚C (Figure 4.2C). Transcript levels of 118 genes were measured and those genes were chosen based on RNA sequencing results from a separate study (Ristow et al., in preparation). In that study, these genes were differentially expressed in CO_2 vs ambient air conditions in either two CO_2-sensitive or two CO_2-tolerant natural strains (source data 1). Out of these 118 CO_2-associated genes, 81 were found to be significantly differentially expressed in the *cbk1*Δ mutant in both ambient air and in 5% CO_2, indicating they are intrinsically dysregulated in the *cbk1*Δ mutant. 57/81 of these genes are downregulated and 24/81 upregulated compared to the WT H99 strain (Figure 4.2D). Interestingly, 16/57 of the downregulated genes were also hits in our deletion set screening. We picked four of these deletion mutants which showed high sensitivity in our screen, to assay their sensitivity to host CO_2 conditions by spotting assay (Figure 4.2E). Taken together, this transcriptomic profiling shows that loss of Cbk1 significantly affects the expression of CO_2-related genes.

The RAM signaling pathway is critical for normal morphology, thermotolerance, and CO_2 tolerance

The RAM pathway effector kinase Cbk1 is part of the NDR/LATS family of kinases, which is conserved from yeast to humans and affects a wide range of cellular functions including cell-cycle regulation. In *C. neoformans*, various virulence factors are impacted by deletion of *CBK1*, including urease activity and thermotolerance [20]. Through our genetic screen for CO_2-sensitive mutants, we found that all tested *Cryptococcus* RAM pathway mutants are extremely

sensitive to 5% CO_2 and high temperature, and they show no growth at 37˚C + 5% CO_2 (Figure 4.3A). In ascomycetes such as *S. cerevisiae* and *C. albicans*, RAM pathway mutants are defective in cytokinesis and exhibit loss of polarity, resulting in enlarged round cells that cluster together [21](Figure S4.4A). In contrast, though defective in cytokinesis [22,23], *Cryptococcus* RAM pathway mutants are hyper-polarized and constitutively form clusters of elongated pseudohyphal cells (Figure S4.4B). Moreover, we found that while the *C. albicans* homozygous *cbk1*ΔΔ mutant exhibits a general growth defect compared to the wild-type control, it shows no apparent specific growth defect at 37˚C with or without 5% CO_2 (Figure S4.4C). These results suggest that, although the RAM pathway is conserved in its role in cytokinesis, the effects of its downstream targets are divergent between ascomycetes and basidiomycetes.

Suppressors of the *cbk1*Δ mutant show improved growth at host conditions

In ascomycetes, Ace2 is a key downstream transcription factor of the RAM pathway (hence in the name of RAM – Regulator of Ace2 and Morphogenesis), which is important for the activation of genes responsible for cell separation as well as a large number of genes with other functions [24,25]. However, no homolog to Ace2 has been identified in *Cryptococcus* or other basidiomycetes. Furthermore, no downstream targets of the RAM pathway have been identified in any basidiomycetes. To investigate potential downstream effectors of the RAM pathway in *Cryptococcus*, we screened for spontaneous suppressor mutants of *cbk1*Δ. To do so, *cbk1*Δ mutant cells from an overnight culture in liquid YPD at 30˚C were plated onto solid YPD media and incubated for two days at 37˚C + 5% CO_2. Out of $>1x10^8$ cells plated and cultured under this condition that is inhibitory for growth of the original *cbk1*Δ mutant, 11 suppressor colonies were isolated for further examination and sequencing. All the suppressor isolates showed dramatically improved growth over the original *cbk1*Δ mutant at 37˚C and modestly improved growth at 37˚C

+ 5% CO_2 (Figure 4.4C). Based on their distinctive phenotypes, the 11 suppressors were classified into two groups: *sup1* (2/11) and *sup2* (9/11). Shorter chains of cells in both groups indicate a partial restoration in cytokinesis (Figure 4.4D). The *sup2* group has slightly improved growth at 37˚C + 5% CO_2 and forms shorter chains of cells compared to the *sup1* group (Figure 4.4C, 4D). Besides of these observations, *sup1* and *sup2* displayed similar phenotypes in growth assays including the cryptococcal virulence traits tested, including melanin production, capsule, urease activity, and cell wall stress tolerance. (Figure S4.5). Both *sup1* and *sup2* showed no improved growth compared to the *cbk1*Δ mutant at pH 7.4 37˚C + 5% CO_2. This is likely due to the detrimental combination of high temperature, CO_2, and high pH, as the WT also showed significantly reduced growth in this condition. (Figure S4.5A). Because RAM pathway suppressor mutants were previously identified after treatment with calcineurin inhibitor FK506, and showed improved growth in FK506 and restored mating [23], we also tested our suppressors' growth in FK506 and their ability to mate. We found that both *sup1* and *sup2* failed to restore growth of the *cbk1*Δ on media supplemented with FK506 or restore the ability to mate with the congenic strain H99a (Figure S4.5).

Along with the original *cbk1*Δ mutant, we sequenced the genomes of the 11 *cbk1*Δ suppressors. By comparing their genome sequences with each other and with the original *cbk1*Δ mutant, we found that both *sup1* type suppressor mutants contained a disruptive in-frame deletion at the same location in *CNAG_01919*, which encodes a putative Poly(A)-specific ribonuclease (PARN) domain-containing protein (Figure 4.4A). This domain was previously reported in *S. pombe* proteins [26]. Interestingly, through a BLAST search of the PARN domain, we did not identify this domain in any protein in the genomes of *S. cerevisiae*, *C. albicans* or other ascomycetes, but found it in Basidiomycetes and higher eukaryotes. The in-frame deletion

results in a change of two amino acids within the predicted PARN domain, the only discernable domain present in this protein. We named this previously uncharacterized gene Partial Suppressor of *cbk1*Δ (*PSC1*). All 9 *sup2* isolates contained loss of function or missense mutations in the gene *CNAG_03345* (Figure 4.4B), which encodes an RNA-binding protein homologous to *S. cerevisiae* Ssd1p, a known suppressor of *cbk1*Δ phenotypes in *S. cerevisiae*. ScSsd1p represses transcript translation and is negatively regulated by Cbk1p phosphorylation [27,28].

To confirm that the putative loss-of-function mutations in *SSD1* and *PSC1* are responsible for suppressing *cbk1*Δ phenotypes, we created *cbk1*Δ*ssd1*Δ and *cbk1*Δ*psc1*Δ double mutants together with the control single mutants *ssd1*Δ and *psc1*Δ. Indeed, relative to the *cbk1*Δ mutant, the double mutants showed reduced sensitivity to host temperature and CO_2 levels (Figure 4.4C), similar to the natural suppressor mutants. Likewise, the morphology of the double mutants resembles that of the spontaneous suppressor mutants (Figure 4.4D). The deletion of *SSD1* and *PSC1* alone in the wild-type background did not yield any discernable phenotype. The results confirm that loss-of-function mutations in *SSD1* and *PSC1* are responsible for partial suppression of the *cbk1*Δ mutant's growth defects observed in the isolated suppressor strains. Interestingly, *sup2* and the *cbk1*Δ*ssd1*Δ mutants both grew noticeably better than *sup1* and *cbk1*Δ*psc1*Δ at 37˚C and 37˚C + 5% CO_2. To test the genetic interaction between the two suppressor genes *SSD1* and *PSC1,* we created a triple *cbk1*Δ*psc1*Δ*ssd1*Δ mutant and the control strain *psc1*Δ*ssd1*Δ. The *psc1*Δ*ssd1*Δ control strain did not exhibit any defect and grew similarly well to either single mutant or the wild type (Figure 4.4C). The triple mutant *cbk1*Δ*psc1*Δ*ssd1*Δ grew similarly well as *sup2* or *cbk1*Δ*ssd1*Δ at 37˚C + 5% CO_2 (Figure 4.4C). However, the triple mutant displayed aberrant morphology and budding defects which are not observed in the natural

suppressor mutants or the *cbk1*Δ*ssd1*Δ and *cbk1*Δ*psc1*Δ double mutants (Figure 4.4D). These results suggest that Psc1 and Ssd1 may function in the same pathway in regulating thermotolerance and CO_2 tolerance, but their downstream effects on cell separation and/or polarized growth may be overlapping and distinct.

To determine if the suppressor mutations restore transcript abundance of the differentially expressed genes under CO_2 in *cbk1*Δ, we compared the profiles of *cbk1*Δ to the two suppressor mutants: *sup1* and *sup2*. Overall, we found that the spontaneous suppressors do not restore transcript abundances of most differentially expressed genes in *cbk1*Δ to WT levels (Figure S4.6), suggesting that suppressors affect post-transcriptional regulation of CO_2 tolerance.

Spontaneous suppressors of *cbk1*Δ mutant show improved ability to survive and replicate in the host

RAM mutants have previously been found to be attenuated in virulence in the invertebrate wax moth larva infection model and mouse intranasal infection models [20,23]. Occasionally, cryptococcal strains with point mutations in RAM genes cause death of mice when revertant mutations occur, which restore the function of the RAM pathway [23]. As shown above and consistent with previous literature, the *cbk1*Δ mutant shows a severe growth defect at host temperature and CO_2 concentrations (Figure 4.3C). Because *sup1* and *sup2* both largely restored growth to the cbk1Δ mutant at 37˚C but only modestly restored growth at 37˚C + 5% CO_2, we decided to test if, and by how much, these suppressor mutations would affect the virulence of the *cbk1*Δ mutant. We infected mice with 1 x 10^4 cells of WT, *cbk1*Δ, *sup1*, or *sup2* intranasally. In this intranasal infection model, the WT H99 strain establishes lung infection first and typically disseminates to other organs including the brain by 7-10 days post-infection (DPI). Mice infected

by H99 normally become morbidly ill by 3-4 weeks post-infection and have a high fungal burden in the lungs, brain, and kidney [29,30].

As expected, all mice infected with H99 were moribund by DPI 26 (Figure 4.5A) while those infected with the *cbk1*Δ mutant survived until the experiment was terminated at DPI 60. Surprisingly, *sup1* and *sup2* strains did not cause any mortality either. The organ fungal burden, however, revealed differences in virulence levels between these strains. At the time of euthanasia for H99-infected mice (prior to DPI 26), the median fungal burden in the lungs, brains, and kidneys was $2.1x10^8$, $1.4x10^6$, and $2.4x10^4$ CFUs per organ respectively (Figure 4.5B). As expected, mice completely cleared the *cbk1*Δ mutant at DPI 35. Surprisingly, despite largely restored growth at 37˚C, *sup1* was completely cleared from the mouse lungs by DPI 35, similar to the *cbk1*Δ mutant. In comparison, although *sup2* did not cause any death during the study period, it was able to replicate in the mouse lungs. The median lung fungal burden at DPI 35 was $8.2x10^4$, over 8-fold higher than the original inoculum. The *sup2* strain maintained the same high lung fungal burden at DPI 60 (Figure 4.5B), indicating that it can persist in the lung tissue. The only *in vitro* difference observed between *sup1* and *sup2* was better growth of *sup2* at host CO_2 levels which may explain the difference in their ability to propagate and persist in the mouse lung. However, it is worth nothing that due to the complex host environment, there could be other unrecognized factors contributing to the differences *in vivo*.

Although the spontaneous suppressor *sup2* was able to replicate in the mouse lungs, no fungal burden was detected in the brain or the kidney at DPI 35 or 60 (no organisms were detected in any of the mice), indicating that the mutant was unable to disseminate. We considered two hypotheses: 1) Inability of suppressor *sup2* to disseminate from the lungs; 2) Inability of suppressor *sup2* to penetrate other organs from the blood. Because *C. neoformans*

can disseminate from the lungs to other organs by a "Trojan Horse" mechanism, where *Cryptococcus* travels within the mobile host phagocytes [31,32], we examined phagocytosis of the *cbk1*Δ mutant and its suppressors to test the first hypothesis. We expected that cryptococcal mutants defective in being phagocytosed by host cells might be defective in dissemination, and the *cbk1*Δ mutant was previously found to have a poor phagocytosis index [33]. Here, we co-cultured murine macrophage JA774 cells with H99, *cbk1*Δ*, sup1*, *sup2*, the double mutant *cbk1*Δ*ssd1*Δ, or the control single mutant *ssd1*Δ. Because different types of opsonization can impact phagocytosis of *C. neoformans*, opsonization was performed using either naïve mouse serum (complement mediated phagocytosis) or serum from mice vaccinated against cryptococcosis (complement + antibody mediated phagocytosis). The serum (containing antibodies) from the vaccinated mice recognizes antigens present in the capsule of cryptococcal cells [30,34]. Consistent with our previous finding, phagocytosis of the *cbk1*Δ mutant was extremely low (~1% of the WT H99 level under complement mediated phagocytosis, Figure 4.5C). Opsonization with serum from vaccinated mice increased phagocytosis of *cbk1*Δ and the suppressor mutants, but the phagocytosis indexes of these mutants were still only 20% or less than that of the wildtype (Figure 4.5D). In both phagocytosis experiments, the suppressor mutants nor the double mutants *ssd1*Δ*cbk1* and *psc1*Δ *cbk1* mutants showed increased phagocytosis relative to the *cbk1*Δ mutant. The poor phagocytosis of the *cbk1*Δ mutant and its suppressors may contribute to their lack of dissemination from the lungs to the other organs in the inhalation infection mouse model of cryptococcosis.

To test the second hypothesis, we infected mice intravenously with H99, *cbk1*Δ*, sup1*, *sup2*, the double mutant *cbk1*Δ*ssd1*Δ, or the control single mutant *ssd1*Δ. In this intravenous infection model, the barrier of the lungs is bypassed. H99 cells disseminate to the brain and other

organs within hours [35]. Because H99 rapidly disseminates in this model, infected mice typically reach moribundity after 1 week. Therefore, we euthanized mice at DPI 5 before H99-infected mice would have become moribund. As expected, H99-infected mice showed high fungal burdens in the lungs, brains, and kidneys, with the highest fungal burden in the brain (over 10^6 CFUs) (Figure 4.5E). The *cbk1*Δ mutant failed to disseminate in this intravenous infection model as no viable cells were recovered in any organ. Similarly, we could not recover any *sup1* cells from the lungs or the brain, and only detected a few fungal cells in the kidney. In contrast, *sup2* suppressor mutants were recovered in all three organs, albeit with reduced fungal burdens (~10^4 CFUs in the brain and a few hundred in lungs/kidney) compared to the wildtype H99 control group (Figure 4.5E). This finding indicates that the *sup2* suppressor, once disseminated into the bloodstream, can invade other organs and replicate. Combined with the earlier observations that 1) both suppressors fully restore growth at host temperature and 2) *sup2* is slightly more CO_2 tolerant than *sup1*, the observation that only *sup2* can survive, amplify, and persist in animals implicates an importance of CO_2 tolerance in cryptococcal pathogenesis. Collectively, the results from phagocytosis, the inhalation infection model, and the intravenous infection model, support the hypothesis that failure of the suppressor mutants to disseminate to other organs in the intranasal model is largely due to reduced phagocytosis and inability to escape the lungs. That said, other factors, such as increased systemic clearance by the immune system, could potentially contribute to the containment of the mutant in the lungs. Again, the *cbk1*Δ*ssd1*Δ mutant recapitulated the phenotype of the *sup2* strain in intravenous infection model and other in vitro assays, demonstrating that our observed *sup2* phenotypes are due to disruption of *SSD1*.

As mutants that are temperature sensitive have reduced virulence in the mouse model of cryptococcosis, we decided to test the virulence of these strains in the *Galleria mellonella* larvae

infection model to remove temperature as a variable. We inoculated *G. mellonella* larvae with 5 x 10^4 cells of WT, *cbk1*Δ, *sup1*, or *sup2*, and maintained the larvae at 30˚C as previously described [23]. PBS buffer inoculated larvae were included as a sham control. Infected larvae (n = 20 per strain) were monitored for survival over a period of 15 days post inoculation. All 20 of the larvae inoculated with the H99 strain died between DPI 3 and DPI 10 (Figure 4.6A). In comparison, only 2/20 of the *cbk1*Δ mutant-infected larvae died during this period. Interestingly, 5/20 *sup1*-infected larvae and 7/20 *sup2*-infected larvae died in this experiment (Figure 4.6A), indicating their partially restored virulence in this larva infection model. To further confirm the observed differences between these strains in this model conducted at 30˚C, we infected 5 larvae with 5 x 10^4 cells per strain and measured their fungal burden at day 5 post inoculation. At DPI 5, the mean fungal burden of WT-infected larvae was $1.5x10^7$ CFUs (Figure 4.6B). In comparison, the mean fungal burden for the *cbk1*Δ-infected larvae was only $8.4x10^2$ CFUs, which is almost 20,000-fold lower than the WT control group and about 60-fold lower than the original inoculum, indicating that most *cbk1*Δ cells have been cleared by this time point. The mean fungal burden of *sup1*-infected larvae was $9.6x10^3$ CFUs while the mean fungal burden *sup2*-infected larvae was $2.3x10^4$ CFUs (Figure 4.6B). These results indicate that both *sup1* and *sup2* partially rescued virulence of the *cbk1*Δ mutant, and that *sup2* showed slightly better restoration of virulence compared to *sup1* in this insect model, which is independent of tolerance to mammalian body temperature.

Discussion

Detection of and adaptation to changing CO_2 levels is an important trait across biological kingdoms and may play a crucial role in the pathogenicity of fungi [6,36-38]. Here we report the identification of genes required for growth at high levels of CO_2 in the fungal pathogen *C.*

neoformans. Multiple pathways important for growth at high temperature, such as the Ras1-Cdc24, CWI, Calcineurin, and RAM pathways, were found to be required for growth in high CO_2 concentrations, indicating that growth in response to host CO_2 may be intricately coordinated and co-regulated with response to host temperature. It is therefore likely that both host CO_2 and host temperature represent stressors that cryptococcal cells infecting mammalian hosts must overcome to cause disease.

Calcineurin and RAM pathways were both identified in our screen for mutants that affect cryptococcal CO_2 sensitivity. A previous study found synthetic lethality between the RAM and calcineurin pathways in *C. neoformans* but not in *S. cerevisiae* [22]. This corroborates our findings of the key differences between the basidiomycete *C. neoformans* and the ascomycete yeasts. In *C. albicans*, CO_2 levels are sensed through bicarbonate or cAMP-dependent activation of adenylyl cyclase to increase hyphal growth [39,40]. While these pathways may also be functioning to sense CO_2 in *Cryptococcus* [13,14], our results indicate that these pathways do not play a significant role in host CO_2 tolerance in *C. neoformans*. We also found that disruption of the RAM pathway effector kinase Cbk1 caused a severe growth defect at host CO_2 in *C. neoformans*, but not in *C. albicans*. The vast differences between these organisms in terms of growth response to CO_2 may reflect the evolutionary distance between these species and/or the distinct niches they normally occupy. Indeed, *C. albicans* is a human commensal and has adapted to host CO_2 concentrations. *S. cerevisiae* is a powerful fermenter that thrives in conditions with high levels of CO_2. For the environmental fungus *C. neoformans*, however, the ability to grow in a CO_2-enriched condition does not appear to be strongly selected for in the natural environment, and the host level of CO_2 (~5% CO_2) is over 100-fold higher than the ambient air (~0.04% CO_2).

The RAM pathway mutants were among the most sensitive mutants to host levels of CO_2. Remarkably, the growth defects of *cbk1*Δ could be partially restored by single mutations in the genes *PSC1* or *SSD1*. While the PARN ribonuclease-encoding gene *PSC1* represents an uncharacterized protein, *SSD1* is a known suppressor of *cbk1*Δ phenotypes that has been extensively characterized in ascomycete yeasts to regulate the translation of numerous and diverse mRNA transcripts [27,28,41-43]. Our genetic interaction analysis indicates that Psc1 likely functions in the same pathway as Ssd1. Interestingly, in *S. cerevisiae*, deletion of *SSD1* can suppress the lethality of the *cbk1*Δ mutant but not the cell separation defect, which is regulated by the transcription factor Ace2 [44]. However, an Ace2 homolog has not been identified in *Cryptococcus* or any other basidiomycete [33]. In *C. albicans*, Ssd1 plays an important role in polarized growth and hyphal initiation by negatively regulating the transcription factor Nrg1 [43]. The observation that *cbk1*Δ*psc1*Δ and *cbk1*Δ*ssd1*Δ suppressor mutants partially rescue cell separation defects or depolarized growth suggests that *C. neoformans* may primarily utilize Ssd1/Psc1 rather than a potential Ace2 homolog to regulate cell separation or polarization. Differential regulation of target mRNA transcripts by Ssd1 and Psc1 may explain the functional divergence of the RAM pathway we observed between the basidiomycete *Cryptococcus* and the ascomycete yeasts. Our observation that the natural suppressors do not restore transcript abundances of CO_2-associated genes in *cbk1*Δ to WT levels supports a hypothesis that disruption of Ssd1 and Psc1 suppresses the *cbk1*Δ mutant's defects at a post-transcriptional level. *C. neoformans* has been demonstrated to use post-transcriptional regulation to adapt to various host stresses [45-47]. A temperature-sensitive environmental species of *Cryptococcus, C. amylolentus*, fails to initiate host stress-induced translational reprogramming and is non-pathogenic [47]. Whether or not translatome reprogramming is initiated in *C. neoformans* in response to host CO_2,

and whether such reprogramming, if occurs, relies on Ssd1 and/or Psc1, has yet to be determined.

Materials and Methods

Strains, growth conditions, and microscopy examination

Strains used in this study are listed in Table 3.2. Unless stated otherwise, all *C. neoformans* cells were maintained at 30˚C on yeast peptone dextrose (YPD) media or YPD + $CuSO_4$ (25 μM) for strains transformed with P_{CTR4}-*CBK1*. For morphological examination, all strains were examined under a Zeiss Imager M2 microscope, equipped with an AxioCam MRm camera. For spotting assays, the tested strains were grown overnight in liquid YPD medium at 30˚C with shaking at 220 RPM. The cells were then adjusted to the same cell density of OD_{600} = 1 and serially diluted 10-fold. The cell suspensions were then spotted onto YPD agar medium and incubated at the indicated condition for two days. CO_2 levels were controlled by a VWR CO_2 incubator or by a Pro-CO_2 controller (Biospherix, Lacona, NY, USA)

Genetic manipulation

Gene Deletion Constructs: To delete the gene *SSD1,* a deletion construct with a Nourseothricin (NAT) resistance marker cassette with 5' and 3' homology arms to *SSD1* was used. Primers Linlab7974 (gctgcctttgcgtcatctc) and Linlab7976 (ctggccgtcgttttactctcgccttccttctcctta) were used to amplify the 5' arm from the H99 genome. The 3' arm was amplified from H99 with primers Linlab7977 (gtcatagctgtttcctgcgattgacattgccgtcttag) and Linlab7979 (cgacctgatcaaactactcgc). The NAT marker was amplified with universal primers M13F and M13R from plasmid pPZP-NATcc. The three pieces were fused together by overlap PCR and amplified with nested primers Linlab7975 (acaatgagccactgccag) and Linlab7977 (tgcgtgttcactactgtagac). To disrupt the gene *PSC1*, a Hygromycin (HYG) marker cassette was

used to insert into the PARN domain. To generate the sgRNA for specific targeting to the *SSD1* locus, the *U6* promoter and sgRNA scaffold were amplified from JEC21 genomic DNA and the plasmid pDD162 using primers Linlab7980/Linlab4627 (ttgagtggggtgggtcaattaacagtataccctgccggtg and ggctcaaagagcagatcaatg) and Linlab7981/Linlab4628 (aattgacccacccccactcaagttttagagctagaaatagcaagtt and cctctgacacatgcagctcc). For sgRNA targeted mutation of *PSC1*, the primers Linlab8380/Linlab4627 (tagttgttttcgccgacgccaacagtataccctgccggtg and ggctcaaagagcagatcaatg) were used to amplify the *U6* promoter, and Linlab8381/Linlab4628 (ggcgtcggcgaaaacaactagttttagagctagaaatagcaagtt and cctctgacacatgcagctcc) to amplify the sgRNA scaffold. The *U6* promoter and sgRNA scaffold were fused together by overlap PCR with primers Linlab4594/Linlab4595 (ccatcgatttgcattagaactaaaaacaaagca and ccgctcgagtaaaacaaaaaagcaccgac) to generate the final sgRNA construct as described previously [19,48].

Gene Overexpression Constructs: The *CBK1* overexpression construct was generated by amplifying the *CBK1* open reading frame with primers Linlab7005/BC (ataggccggccatgtcgtatcgcccaatccag) and Linlab7006/BC (cagcatctcgtatcgtcggaag) and cloning the fragment with FseI and PacI into the pXC plasmid backbone [16], which contains the promoter of *CTR4* and Neomycin resistance marker. The *CTR4* promoter is highly induced on the copper limiting YPD media. The *MPK1* overexpression construct was generated by amplifying the *MPK1* open reading frame with primers Linlab8326/BC (ataggccggccatggacaataccccctagacac) and Linlab8327/BC (ccttaattaaggctatgataatttctgcctctcc) and cloning the fragment with FseI and AsiSI into a pUC19 plasmid backbone, containing the promoter of *GPD1* and Neomycin resistance marker. The *CDC24* overexpression construct was generated by amplifying the *CDC24* open

reading frame with primers Linlab6674/BC (ataggccggccatgtctgtatccggtcccatctc) and Linlab6675/BC (ccttaattaaggataaatctctccttgtggggtacc) and cloning the fragment with FseI and PacI into a pUC19 plasmid backbone, containing the promoter of *CTR4* and Neomycin resistance marker. The overexpression constructs were integrated into the *SH2* locus as described previously [19,48].

Transformation: Constructs for overexpression and deletion were transformed into *Cryptococcus* strains by the TRACE method [19,48], and transformants were selected on YPD medium with 100 μg/mL of nourseothricin (NAT),100 μg/mL of neomycin (NEO), or 200 μg/mL of hygromycin (HYG).

Quantitative Real-Time PCR

WT H99 strain along with the *cbk1*Δ, *CBK1*^{OE} strain were cultured by shaking at 220 RPM at 30˚C overnight in liquid YPD medium containing 50μM $CuSO_4$ to suppress the CTR4 promoter of the *CBK1*^{OE} construct. The cultures were then diluted to OD_{600}=.2 in fresh liquid YPD medium containing 50μM BCS to induce expression. After 5 hours of further incubation, cells were collected, flash frozen in liquid nitrogen, and lyophilized overnight. Three biological replicates per strain were used. Total RNA was isolated by using the PureLink RNA Mini Kit (Invitrogen) and first strand cDNA was synthesized using the GoScript Reverse Transcription System (Promega) following the manufacturer's instructions. The Power SYBR Green system (Invitrogen) was used for RT-PCR. The following primers were used to target *CBK1*: Linlab9217/BC (gatgctctcactcctgattcc) and Linlab8641/BC (gtacgagtctgacttcaccga). The following primers were used to target the *TEF1* housekeeping gene as an endogenous control for each sample: Linlab329/XL (cgtcaccactgaagtcaagt) and Linlab330/XL (agaagcagcctccatagg).

Relative transcript level was determined using the ΔΔct method as described previously. Statistical significance was determined using a student's t-test.

NanoString RNA profiling

Overnight YPD cultures of H99, *cbk1*Δ, *cbk1*Δ*ssd1*Δ, and *cbk1*Δ*psc1*Δ were washed 2X in PBS and resuspended in RPMI+165mM MOPS, pH 7.4 before quantification on an Invitrogen Countess automated cell counter. Cells were diluted to $7.5x10^5$ cells per mL in 3 mL per well in a 6-well plate. Two wells were used for each biological replicate (n=3) and condition (ambient or 5% CO_2). Plates were sealed with BreatheEasy sealing membranes (Sigma #Z380059) and incubated in a static incubator at 30˚C in ambient air or 5% CO_2 for 24 hours. Cells were harvested, pelleted at 3,200xg for 5 minutes, and the supernatant was removed. The pellets were then frozen at -80˚C and lyophilized overnight. Lyophilized cells were disrupted for 45 seconds with 0.5mm glass beads on an MP Biomedicals FastPrep-24 benchtop homogenizer. RNA was extracted following manufacturer instructions for the Invitrogen PureLink RNA mini-kit with on-column DNAse treatment. Purified RNA was quantified on a NanoDrop OneC spectrophotometer and a total of 100ng per sample was combined with a custom probeset (Source data 1) from NanoString Technologies according to manufacturer instructions. Probes were hybridized at 65˚C for 18 hours, then run on a NanoString nCounter SPRINT profiler according to manufacturer instructions. Data from Reporter Code Count (RCC) files were extracted with nSolver software (version 4.0) and raw counts were exported to Microsoft Excel. Internal negative controls were used to subtract background from raw counts (negative control average + 2 standard deviations). Counts were normalized across samples by total RNA counts. Probes below background were set to a value of 1. Fold change and significance were calculated in Excel after averaging biological triplicates, using a Student t-test ($p<0.05$). Volcano plot was

generated with transformed values (-log[p-value] and log_2[fold change]) in GraphPad Prism 9. Normalized total counts were used in Morpheus (https://software.broadinstitute.org/morpheus/) to generate a heat map, with hierarchical clustering, one minus Pearson correlation, average linkage method and clustered according to rows and columns.

Bioinformatics

Whole genome sequencing was performed using the Illumina platform with NovaSeq 6000 at the University of California – Davis Sequencing Center, Novogene USA. A paired-end library with approximately 350 base inserts was constructed for each sample, and all libraries were multiplexed and run in one lane using a read length of 150 bases from either side.

The Illumina reads were first trimmed with Trim Galore v0.6.5 [49], and then mapped to the *Cryptococcus neoformans* H99 reference genome (FungiDB version 50) using the BWA-MEM algorithm of the BWA aligner v0.7.17[50]. SAMtools v1.10 [51], Picard Tools v2.16.0 [52], and bcftools v1.13 [53] were used for variant calling from each sample. Variants in the suppressor strains were called with the original *cbk1*Δ mutant as a reference.

The protein diagrams of Psc1 and Ssd1 were made with the illustrator of biological sequences (IBS) software package [54].

Phagocytosis Assays

The authenticated mouse macrophage cell line J774A.1 (ATCC® TIB-67™) was acquired from the American Type Culture Collection. Before being used, normal morphology, cell adhesion, and phagocytosis activity of the cell line was confirmed. Contamination by mycoplasma was not detected. Phagocytosis assays were performed using similar procedures as we described previously [33]. Briefly, 1mL of $2x10^5$ J774A.1 macrophages (MΦ) in DMEM was seeded into a 24 well plate and incubated at 37˚C with 5% CO_2 for 24 hours. *Cryptococcus*

strains with a starting OD_{600} of 0.2 in 3mL of liquid YPD were cultured for 16 hours. Each strain had three technical replicates. The cells were washed three times in sterile H_2O. $2x10^6$ cryptococcal cells of each strain were opsonized in either 40µl of 100% fetal bovine serum, naïve mouse serum, or mouse serum from LW10 vaccinated A/J mice [30,34], for 30 minutes prior to co-incubation with MΦ. Old DMEM from MΦ was removed and 1mL of fresh DMEM with the opsonized *Cryptococcus* cells were added, followed by a 2-hour incubation at 37˚C with 5% CO_2. The co-culture was then washed six times with warm PBS to remove non-adherent *Cryptococcus* cells. To lyse the macrophages, the cell suspensions were washed with 1mL of cold PBS + 0.01% Triton X. Serial dilutions in PBS of the cell suspensions were then plated onto YNB agar medium and allowed to grow at 30˚C for two days to count colony forming units (CFUs). Statistical analyses were performed using the program Graphpad Prism 8. A two-tailed t-test was applied to determine significance. A p-value of less than 0.05 was considered significant.

***G. mellonella* Infection Model**

Galleria mellonella larvae were purchased from Best Bait (Marblehead, OH). The infection was performed as described previously described [55]. In brief, cryptococcal strains were inoculated in 3mL of liquid YPD medium with the initial OD_{600}= 0.2 (approximately 10^6 cell/mL) and incubated for 15 hours at 30˚C with shaking. Prior to infection, cells were washed with sterile PBS three times and adjusted to the final concentration of $1x10^7$ cell/mL. 5µL of the cell suspension ($5x10^4$ cells), or PBS for the control group, were injected into the last left proleg of the larvae. The proleg was cleaned with 70% ethanol prior to injection. Infected larvae were maintained at 30˚C and monitored daily for survival.

Prior to fungal burden quantification, larvae were first cleaned with 70% ethanol. The larvae were cut open with sterile scissors and vortexed in a microcentrifuge tube containing 500μL PBS and 100μL of 0.5mm diameter glass beads (RPI). Larval suspensions were then serially diluted in PBS and plated onto YNB agar medium containing 50μg/mL Kanamycin and 20μg/mL chloramphenicol and incubated at 30˚C for 2 days before counting the colony-forming units (CFUs).

Statistical analyses were performed using the program Graphpad Prism 8. The log-rank Mantel-Cox test was used to assess statistical significance of survival curves for comparison between two groups. One-way ANOVA tests were used to compare groups of three or more and for fungal burden assays.

Murine models of cryptococcosis

Intranasal infection model: Female Balb/C mice of 8-10 weeks old were purchased from the Jackson Labs (Bar Harbor, Maine). Cryptococcal strains were inoculated in 3mL of liquid YPD medium with the initial OD_{600}= 0.2 (approximately 10^6 cell/mL) and incubated for 15 hours at 30˚C with shaking. Prior to intranasal infection, cells were washed with sterile saline three times and adjusted to the final concentration of $2x10^5$ cell/mL. Once the mice were sedated with ketamine and xylazine via intraperitoneal injection, 50μL of the cell suspension ($1x10^4$ cells per mouse) were inoculated intranasally as previously described [30,56-59]. Mice were monitored daily for disease progression. Surviving animals were euthanized at day 35 or 60 post-infection (DPI) and the brain, lungs, and kidneys, were dissected.

Intravenous infection model: Prior to intravenous infections, cryptococcal cells were washed with sterile saline three times and adjusted to the final concentration of $1x10^6$ cell/mL. Mice were sedated with Isoflurane. 100μL of the cell suspension ($1x10^5$ cells per mouse) were injected

intravenously as previously described [56-59]. After DPI 5, animals were euthanized and the brain, lungs, and kidneys were dissected.

For fungal burden quantifications, dissected organs were homogenized in 2mL of cold sterile PBS using an IKA-T18 homogenizer as we described previously [34,58]. Tissue suspensions were serially diluted in PBS and plated onto YNB agar medium and incubated at 30˚C for 2 days before counting the colony-forming units (CFUs).

Ethical statements

This study was performed according to the guidelines of NIH and the University of Georgia Institutional Animal Care and Use Committee (IACUC). The animal models and procedures used have been approved by the IACUC (AUP protocol numbers: A2017 08-023 and A2020 06-015).

Data Availability

Sequences generated from this research has been deposited to the Sequence Read Archive (SRA) under project accession number: PRJNA791949.

Acknowledgments

This work was supported by National Institutes of Health (http://www.niaid.nih.gov) (R01AI147541 to D.J.K. and X.L., and R01AI140719 to X.L.). The funder had no role in study design, data collection, and interpretation, or the decision to submit the work for publication. We thank all Lin lab members for their helpful suggestions. We thank Dr. Fanglin Zheng for the plasmid pFZ1, and Dr. Lukasz Kozubowski for the plasmid LKB61.

References

1. Rajasingham, R. *et al.* Global burden of disease of HIV-associated cryptococcal meningitis: an updated analysis. *The Lancet Infectious Diseases* **17**, 873-881 (2017).
2. Zhao, Y., Lin, J., Fan, Y. & Lin, X. Life cycle of *Cryptococcus neoformans*. *Annual Review of Microbiology* **73**, null (2019).

3. Casadevall, A. & Perfect, J.R. *Cryptococcus Neoformans*, (ASM Press, 1998).
4. Litvintseva, A.P. & Mitchell, T.G. Most environmental isolates of *Cryptococcus neoformans* var. *grubii* (serotype A) are not lethal for mice. *Infect Immun* **77**, 3188-95 (2009).
5. Mukaremera, L. *et al.* The Mouse Inhalation Model of *Cryptococcus neoformans* Infection Recapitulates Strain Virulence in Humans and Shows that Closely Related Strains Can Possess Differential Virulence. *Infect Immun* **87**(2019).
6. Krysan, D.J., Zhai, B., Beattie, S.R., Misel, K.M., Wellington, M. & Lin, X. Host carbon dioxide concentration is an independent stress for *Cryptococcus neoformans* that affects virulence and antifungal susceptibility. *mBio* **10**, e01410-19 (2019).
7. Perfect, J.R. *Cryptococcus neoformans*: the yeast that likes it hot. *FEMS Yeast Res* **6**, 463-8 (2006).
8. Yang, D.-H. *et al.* Rewiring of Signaling Networks Modulating Thermotolerance in the Human Pathogen *Cryptococcus neoformans*. *Genetics* **205**, 201 (2017).
9. Stempinski, P.R. *et al.* Genetic contribution to high temperature tolerance in *Cryptococcus neoformans*. *Genetics* **217**, 1-15 (2021).
10. Gobeil, S.M.C. *et al.* Leveraging Fungal and Human Calcineurin-Inhibitor Structures, Biophysical Data, and Dynamics To Design Selective and Nonimmunosuppressive FK506 Analogs. *mBio* **12**, e0300021-e0300021 (2021).
11. Chun, C.D. & Madhani, H.D. Applying genetics and molecular biology to the study of the human pathogen *Cryptococcus neoformans*. *Methods Enzymol* **470**, 797-831 (2010).
12. Klengel, T. *et al.* Fungal adenylyl cyclase integrates CO_2 sensing with cAMP signaling and virulence. *Current biology : CB* **15**, 2021-2026 (2005).
13. Mogensen, E.G. *et al. Cryptococcus neoformans* Senses CO_2 through the Carbonic Anhydrase Can2 and the Adenylyl Cyclase Cac1. *Eukaryotic Cell* **5**, 103-111 (2006).
14. Bahn, Y.-S., Cox, G.M., Perfect, J.R. & Heitman, J. Carbonic Anhydrase and CO_2 Sensing during *Cryptococcus neoformans* Growth, Differentiation, and Virulence. *Current Biology* **15**, 2013-2020 (2005).
15. Wang, L. *et al.* Morphotype transition and sexual reproduction are genetically associated in a ubiquitous environmental pathogen. *PLoS pathogens* **10**, e1004185-e1004185 (2014).
16. Wang, L., Zhai, B. & Lin, X. The link between morphotype transition and virulence in *Cryptococcus neoformans*. *PLoS pathogens* **8**, e1002765-e1002765 (2012).
17. Ory, J.J., Griffith, C.L. & Doering, T.L. An efficiently regulated promoter system for *Cryptococcus neoformans* utilizing the CTR4 promoter. *Yeast* **21**, 919-26 (2004).
18. Upadhya, R. *et al.* A fluorogenic *C. neoformans* reporter strain with a robust expression of m-cherry expressed from a safe haven site in the genome. *Fungal Genet Biol* **108**, 13-25 (2017).
19. Lin, J., Fan, Y. & Lin, X. Transformation of *Cryptococcus neoformans* by electroporation using a transient CRISPR-Cas9 expression (TRACE) system. *Fungal genetics and biology : FG & B* **138**, 103364-103364 (2020).
20. Lee, K.T. *et al.* Systematic functional analysis of kinases in the fungal pathogen *Cryptococcus neoformans*. *Nat Commun* **7**, 12766 (2016).
21. Saputo, S., Chabrier-Rosello, Y., Luca, F.C., Kumar, A. & Krysan, D.J. The RAM Network in Pathogenic Fungi. *Eukaryotic Cell* **11**, 708 (2012).

22. Walton, F.J., Heitman, J. & Idnurm, A. Conserved elements of the RAM signaling pathway establish cell polarity in the basidiomycete *Cryptococcus neoformans* in a divergent fashion from other fungi. *Molecular biology of the cell* **17**, 3768-3780 (2006).
23. Magditch, D.A., Liu, T.-B., Xue, C. & Idnurm, A. DNA Mutations Mediate Microevolution between Host-Adapted Forms of the Pathogenic Fungus *Cryptococcus neoformans*. *PLOS Pathogens* **8**, e1002936 (2012).
24. Wakade, R.S., Ristow, L.C., Stamnes, M.A., Kumar, A. & Krysan, D.J. The Ndr/LATS Kinase Cbk1 Regulates a Specific Subset of Ace2 Functions and Suppresses the Hypha-to-Yeast Transition in *Candida albicans*. *mBio* **11**(2020).
25. Mulhern, S.M., Logue, M.E. & Butler, G. *Candida albicans* transcription factor Ace2 regulates metabolism and is required for filamentation in hypoxic conditions. *Eukaryot Cell* **5**, 2001-13 (2006).
26. Marasovic, M., Zocco, M. & Halic, M. Argonaute and Triman Generate Dicer-Independent priRNAs and Mature siRNAs to Initiate Heterochromatin Formation. *Molecular Cell* **52**, 173-183 (2013).
27. Wanless, A.G., Lin, Y. & Weiss, E.L. Cell morphogenesis proteins are translationally controlled through UTRs by the Ndr/LATS target Ssd1. *PLoS One* **9**, e85212 (2014).
28. Jansen, J.M., Wanless, A.G., Seidel, C.W. & Weiss, E.L. Cbk1 regulation of the RNA-binding protein Ssd1 integrates cell fate with translational control. *Curr Biol* **19**, 2114-20 (2009).
29. Chadwick, B.J. & Lin, X. On the History and Applications of Congenic Strains in *Cryptococcus* Research. *Pathogens* **9**(2020).
30. Lin, J. *et al.* Immunoprotection against Cryptococcosis Offered by Znf2 Depends on Capsule and the Hyphal Morphology. *mBio* **0**, e02785-21 (2022).
31. Kechichian, T.B., Shea, J. & Del Poeta, M. Depletion of alveolar macrophages decreases the dissemination of a glucosylceramide-deficient mutant of *Cryptococcus neoformans* in immunodeficient mice. *Infect Immun* **75**, 4792-8 (2007).
32. Santiago-Tirado, F.H., Onken, M.D., Cooper, J.A., Klein, R.S. & Doering, T.L. Trojan Horse Transit Contributes to Blood-Brain Barrier Crossing of a Eukaryotic Pathogen. *mBio* **8**(2017).
33. Lin, J., Idnurm, A. & Lin, X. Morphology and its underlying genetic regulation impact the interaction between *Cryptococcus neoformans* and its hosts. *Med Mycol* **53**, 493-504 (2015).
34. Zhai, B. *et al.* Development of protective inflammation and cell-mediated immunity against *Cryptococcus neoformans* after exposure to hyphal mutants. *mBio* **6**, e01433-15 (2015).
35. O'Connor, L. *et al.* Pharmacodynamics of liposomal amphotericin B and flucytosine for cryptococcal meningoencephalitis: safe and effective regimens for immunocompromised patients. *The Journal of infectious diseases* **208**, 351-361 (2013).
36. Bahn, Y.S. & Mühlschlegel, F.A. CO_2 sensing in fungi and beyond. *Curr Opin Microbiol* **9**, 572-8 (2006).
37. Hetherington, A.M. & Raven, J.A. The biology of carbon dioxide. *Curr Biol* **15**, R406-10 (2005).
38. Cummins, E.P., Selfridge, A.C., Sporn, P.H., Sznajder, J.I. & Taylor, C.T. Carbon dioxide-sensing in organisms and its implications for human disease. *Cell Mol Life Sci* **71**, 831-45 (2014).

39. Du, H. *et al.* The transcription factor Flo8 mediates CO_2 sensing in the human fungal pathogen *Candida albicans*. *Mol Biol Cell* **23**, 2692-701 (2012).
40. Hall, R.A. *et al.* CO(2) acts as a signalling molecule in populations of the fungal pathogen Candida albicans. *PLoS Pathog* **6**, e1001193 (2010).
41. Li, L., Lu, Y., Qin, L.X., Bar-Joseph, Z., Werner-Washburne, M. & Breeden, L.L. Budding yeast SSD1-V regulates transcript levels of many longevity genes and extends chronological life span in purified quiescent cells. *Mol Biol Cell* **20**, 3851-64 (2009).
42. Hu, Z. *et al.* Ssd1 and Gcn2 suppress global translation efficiency in replicatively aged yeast while their activation extends lifespan. *Elife* **7**(2018).
43. Lee, H.J., Kim, J.M., Kang, W.K., Yang, H. & Kim, J.Y. The NDR Kinase Cbk1 Downregulates the Transcriptional Repressor Nrg1 through the mRNA-Binding Protein Ssd1 in Candida albicans. *Eukaryot Cell* **14**, 671-83 (2015).
44. Kurischko, C., Weiss, G., Ottey, M. & Luca, F.C. A Role for the Saccharomyces cerevisiae Regulation of Ace2 and Polarized Morphogenesis Signaling Network in Cell Integrity. *Genetics* **171**, 443-455 (2005).
45. Stovall, A.K., Knowles, C.M., Kalem, M.C. & Panepinto, J.C. A Conserved Gcn2-Gcn4 Axis Links Methionine Utilization and the Oxidative Stress Response in *Cryptococcus neoformans*. *Front Fungal Biol* **2**(2021).
46. Kalem, M.C., Subbiah, H., Leipheimer, J., Glazier, V.E. & Panepinto, J.C. Puf4 Mediates Post-transcriptional Regulation of Cell Wall Biosynthesis and Caspofungin Resistance in *Cryptococcus neoformans*. *mBio* **12**(2021).
47. Bloom, A.L.M. *et al.* Thermotolerance in the pathogen *Cryptococcus neoformans* is linked to antigen masking via mRNA decay-dependent reprogramming. *Nature communications* **10**, 4950-4950 (2019).
48. Fan, Y. & Lin, X. Multiple Applications of a Transient CRISPR-Cas9 Coupled with Electroporation (TRACE) System in the *Cryptococcus neoformans* Species Complex. *Genetics* **208**, 1357-1372 (2018).
49. Krueger, F. Trim Galore! (2021).
50. Li, H. Aligning sequence reads, clone sequences and assembly contigs with BWA-MEM. (2013).
51. Li, H. *et al.* The Sequence Alignment/Map format and SAMtools. *Bioinformatics (Oxford, England)* **25**, 2078-2079 (2009).
52. Broad_Institute. Picard Tools. *Broad Institute, GitHub repository*.
53. Danecek, P. *et al.* Twelve years of SAMtools and BCFtools. *GigaScience* **10**, giab008 (2021).
54. Liu, W. *et al.* IBS: an illustrator for the presentation and visualization of biological sequences. *Bioinformatics* **31**, 3359-61 (2015).
55. Mylonakis, E. *et al. Galleria mellonella* as a model system to study *Cryptococcus neoformans* pathogenesis. *Infect Immun* **73**, 3842-50 (2005).
56. Zhao, Y., Wang, Y., Upadhyay, S., Xue, C. & Lin, X. Activation of Meiotic Genes Mediates Ploidy Reduction during Cryptococcal Infection. *Curr Biol* **30**, 1387-1396 e5 (2020).
57. Zhai, B., Zhu, P., Foyle, D., Upadhyay, S., Idnurm, A. & Lin, X. Congenic strains of the filamentous form of *Cryptococcus neoformans* for studies of fungal morphogenesis and virulence. *Infect Immun* **81**, 2626-37 (2013).

58. Zhai, B., Wu, C., Wang, L., Sachs, M.S. & Lin, X. The antidepressant sertraline provides a promising therapeutic option for neurotropic cryptococcal infections. *Antimicrob Agents Chemother* **56**, 3758-66 (2012).
59. Zhu, P., Zhai, B., Lin, X. & Idnurm, A. Congenic strains for genetic analysis of virulence traits in *Cryptococcus gattii*. *Infect Immun* **81**, 2616-25 (2013).
60. Nielsen, K., Cox, G.M., Wang, P., Toffaletti, D.L., Perfect, J.R. & Heitman, J. Sexual cycle of *Cryptococcus neoformans* var. *grubii* and virulence of congenic a and alpha isolates. *Infect Immun* **71**, 4831-41 (2003).
61. Kozubowski, L., Aboobakar, E.F., Cardenas, M.E. & Heitman, J. Calcineurin colocalizes with P-bodies and stress granules during thermal stress in *Cryptococcus neoformans*. *Eukaryot Cell* **10**, 1396-402 (2011).
62. Bahn, Y.S., Kojima, K., Cox, G.M. & Heitman, J. A unique fungal two-component system regulates stress responses, drug sensitivity, sexual development, and virulence of Cryptococcus neoformans. *Mol Biol Cell* **17**, 3122-35 (2006).
63. Bahn, Y.-S., Kojima, K., Cox, G.M. & Heitman, J. Specialization of the HOG Pathway and Its Impact on Differentiation and Virulence of Cryptococcus neoformans. *Molecular Biology of the Cell* **16**, 2285-2300 (2005).
64. Dickinson, D.J., Ward, J.D., Reiner, D.J. & Goldstein, B. Engineering the Caenorhabditis elegans genome using Cas9-triggered homologous recombination. *Nat Methods* **10**, 1028-34 (2013).
65. Walton, F.J., Idnurm, A. & Heitman, J. Novel gene functions required for melanization of the human pathogen Cryptococcus neoformans. *Mol Microbiol* **57**, 1381-96 (2005).

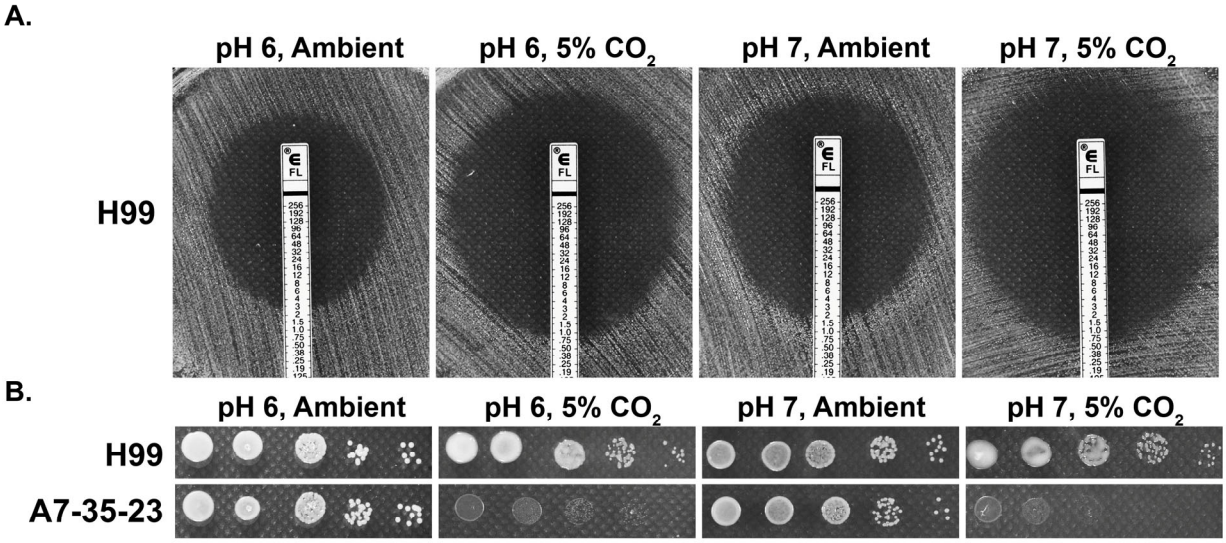

Figure 4.1. CO_2 sensitivity is not simply due to lowered medium pH. (A) H99 cells were plated onto RPMI solid medium buffered to either pH 6 or pH 7. Fluconazole containing E-test strips were placed onto the lawn of H99 cells and the plates were incubated at 37˚C in ambient air or in 5% CO_2. The larger the halo surrounding the E-strip, the more sensitive the cells are to

fluconazole. The intercept value of the halo with the E-strip is the minimal inhibitory concentration. (B) Cells of the previously identified CO_2-tolerant H99 and CO_2-sensitive A7-35-23 were serial diluted, spotted onto RPMI media buffered to pH 6 or pH 7, and incubated at 37˚C in ambient air or in 5% CO_2.

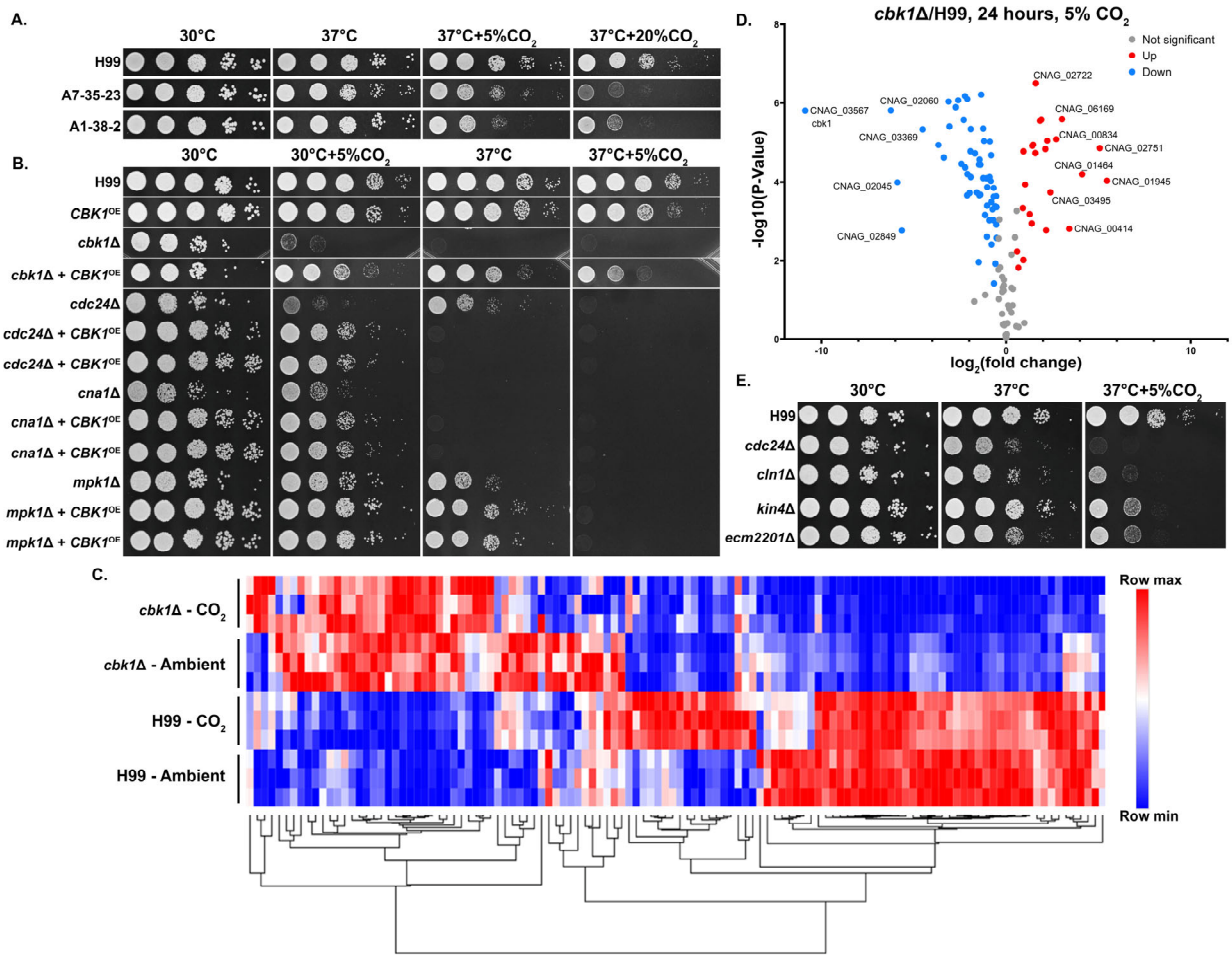

Figure 4.2. The RAM pathway effector kinase Cbk1 is critical for CO_2 tolerance. (A). The clinical reference strain H99 and environmental strains A7-35-23 and A1-38-2 were grown overnight in YPD, serially diluted, and spotted onto solid YPD media plates. Photographs were taken two days after incubation in the indicated condition. (B) This serial dilution spotting assay was similarly performed for H99 and the mutants indicated. Two independent overexpression transformants for each mutant background were included as biological replicates. (C) Heatmap

showing normalized total RNA counts of NanoString targets in H99 and *cbk1Δ* cultured at either ambient or 5% CO_2, red indicates higher and blue indicates lower transcript abundance. (D) Volcano plot showing significantly differentially expressed transcripts (p-value of <0.05) in the *cbk1Δ* compared to H99 in the 5% CO_2 condition. (E) Serial dilution spotting assay of H99 and four of the mutants found in the deletion set screening to be CO_2 sensitive which also correspond to significantly downregulated genes shown in the Volcano plot.

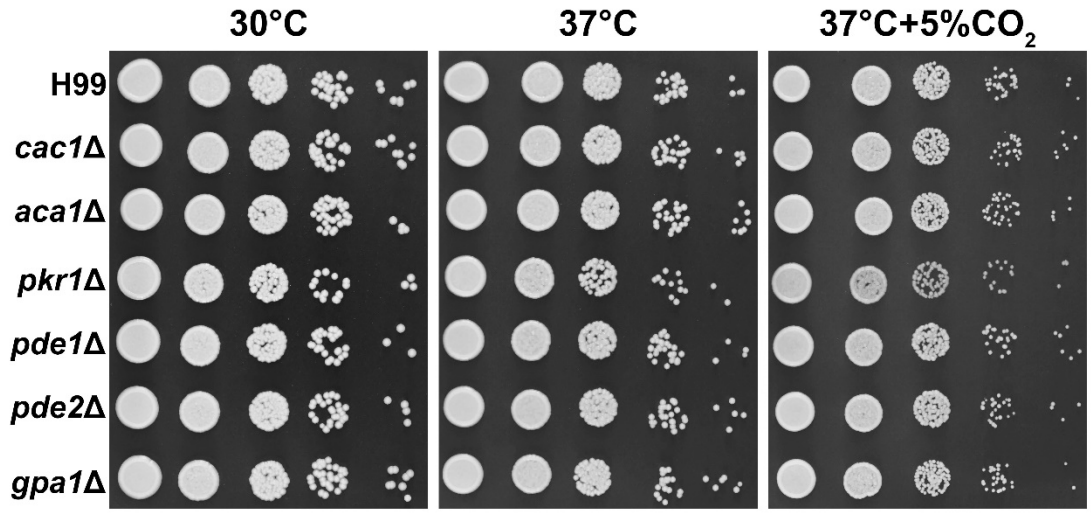

Figure S4.1. The cAMP pathway is not essential for CO_2 tolerance. The reference strain H99 and the indicated gene deletion mutants were grown overnight in YPD, serially diluted, and spotted onto solid YPD media plates. Photographs were taken two days after incubation in the indicated condition.

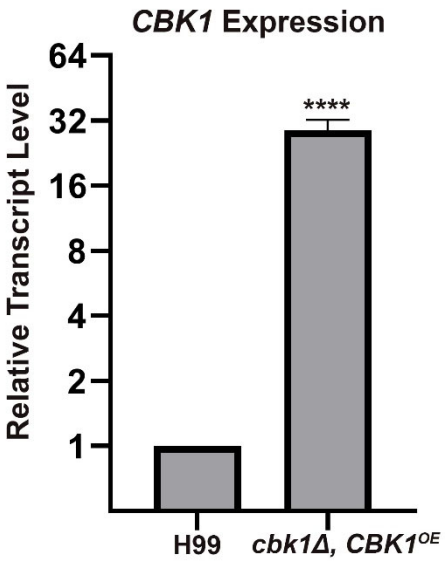

Figure S4.2. Confirming overexpression of *CBK1*. The relative transcript levels of the *CBK1* gene in the *cbk1*Δ, *CBK1*^{OE} strain compared to in the WT strain was assayed by RT-PCR. The transcript level of *CBK1* in the WT strain background was set to 1 for normalization. The housekeeping gene *TEF1* was used as an endogenous control. Three biological and three technical replicates were used for each sample. A student's t-test was used to determine significance level. "****" refers to a *p value* < 0.0001.

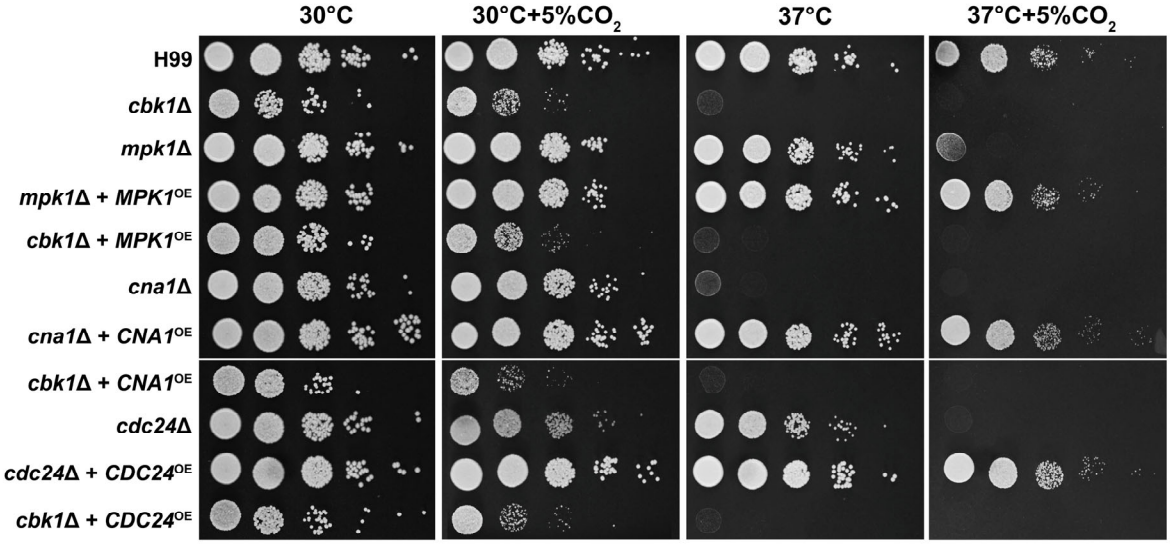

Figure S4.3 Overexpression of *CDC24*, *MPK1*, or *CNA1* does not restore growth at host CO_2 or temperature levels. The strains above were grown overnight in YPD, serially diluted, and spotted onto solid YPD media plates. Photographs were taken two days after incubation in the indicated condition.

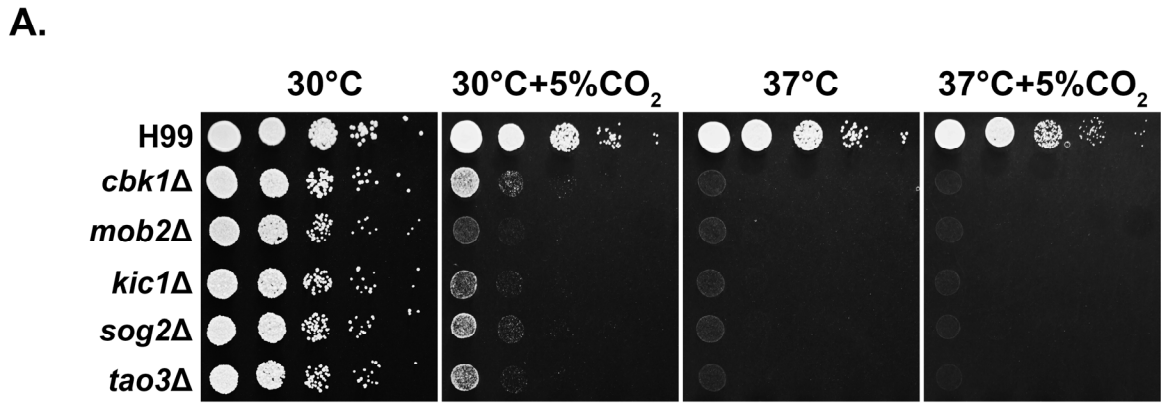

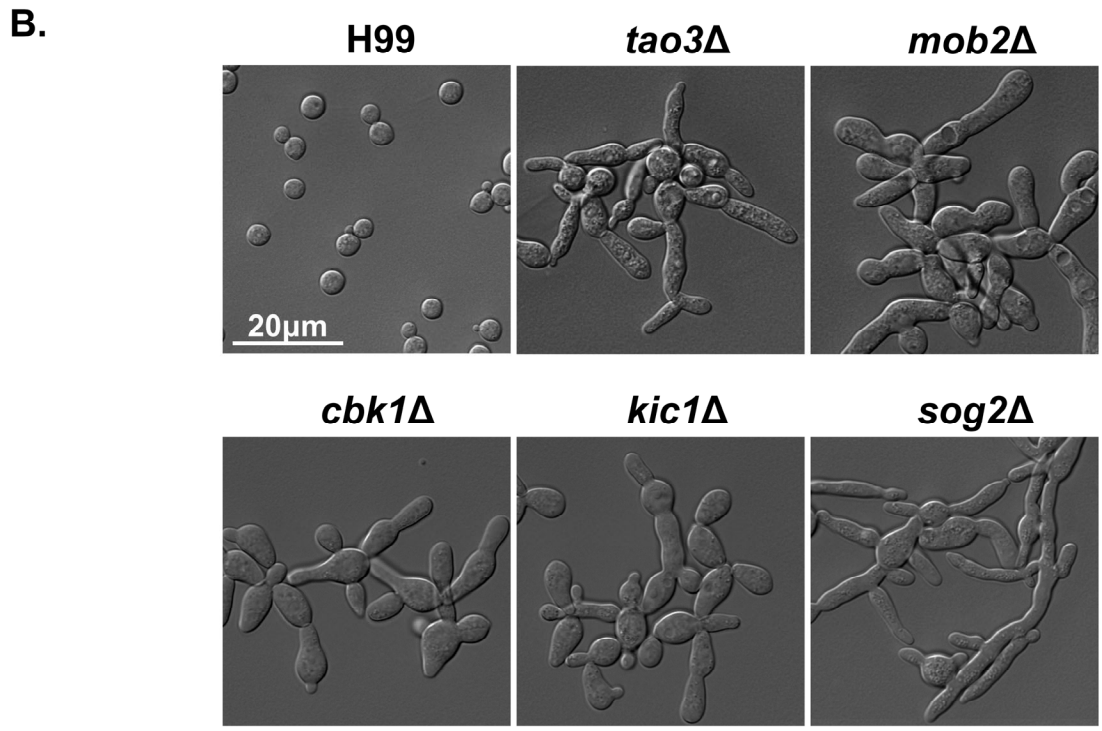

Figure 4.3 The RAM pathway is critical for normal morphology, thermotolerance, and CO_2 tolerance. (A) *C. neoformans* WT H99 and RAM pathway mutants were serially diluted, spotted onto YPD medium, and incubated for two days at the indicated condition. (B) The

cellular morphology of *Cryptococcus neoformans* WT H99 and RAM pathway mutants cultured in YPD medium.

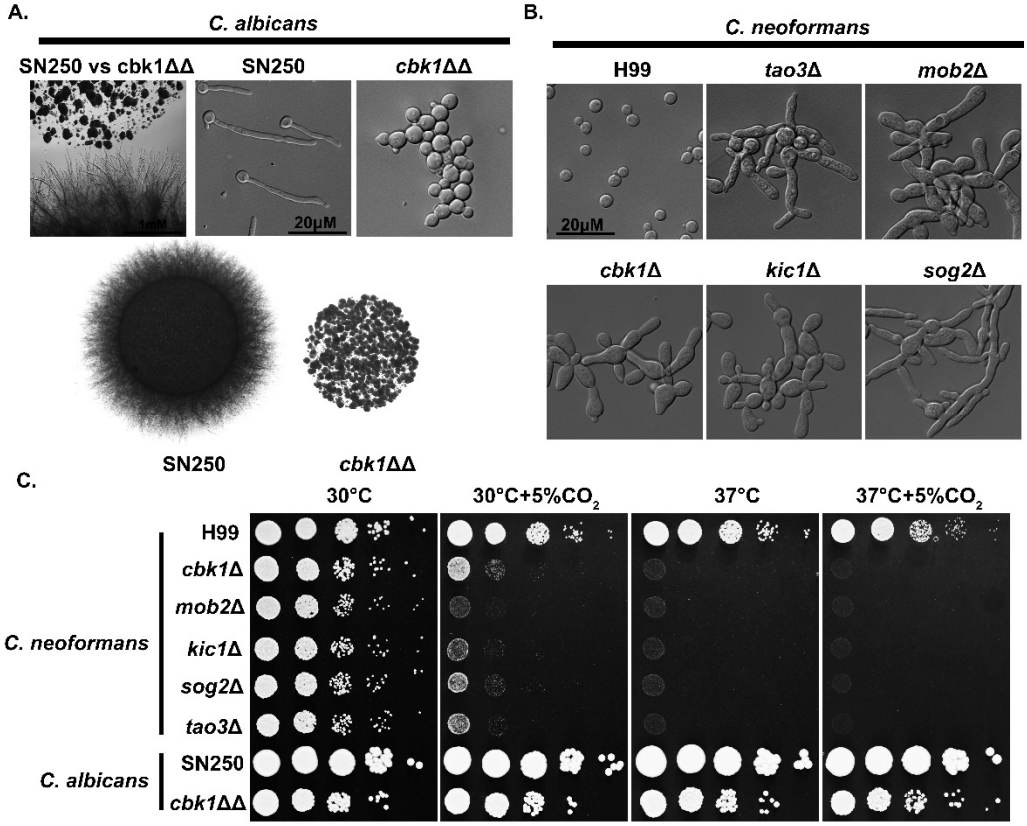

Figure S4.4. Conserved and divergent roles of the RAM pathway in ascomycete *Candida albicans* and basidiomycete *Cryptococcus neoformans*. (A) The colony and cellular morphology of *Candida albicans* WT strain SN250 and the homozygous *cbk1*ΔΔ mutant grown on RPMI. (B) The cellular morphology of *Cryptococcus neoformans* WT H99 and RAM pathway mutants cultured in YPD medium. (C) *C. neoformans* and *C. albicans* WT and RAM pathway mutants were serially diluted, spotted onto YPD medium, and incubated for two days at the indicated condition. The *Cryptococcus neoformans* data in this Figure 4.were taken from Figure 4.6.

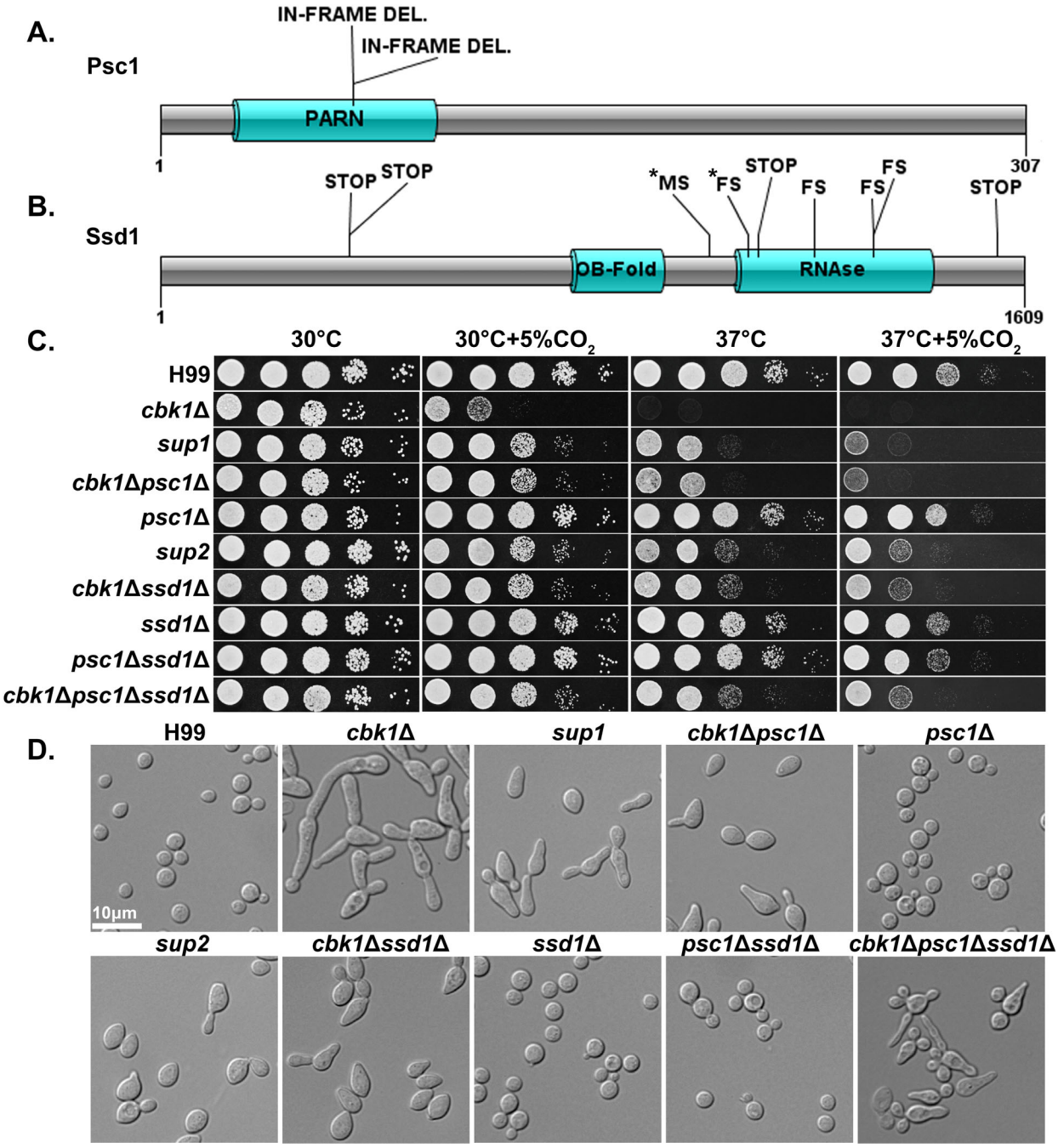

Figure 4.4. Natural suppressors of the RAM pathway *cbk1*Δ mutant restore multiple defects. (A) Protein diagram of Psc1 showing the effects and positions of suppressor mutations in the two *sup1* type natural suppressors. (B) Protein diagram of Ssd1 and the effects and positions of suppressor mutations in Ssd1 in the nine *sup2* type natural suppressors. STOP

indicates a nonsense mutation, MS a missense mutation, and FS a frameshift mutation. Asterisks (*) indicate mutations in the same suppressor strain. (C) Serial dilutions of H99 and the mutant strains were spotted onto YPD agar media and incubated for two days in the indicated condition to observe growth. (D) The cellular morphology of H99 and the mutant strains in liquid YPD cultures were examined under microscope.

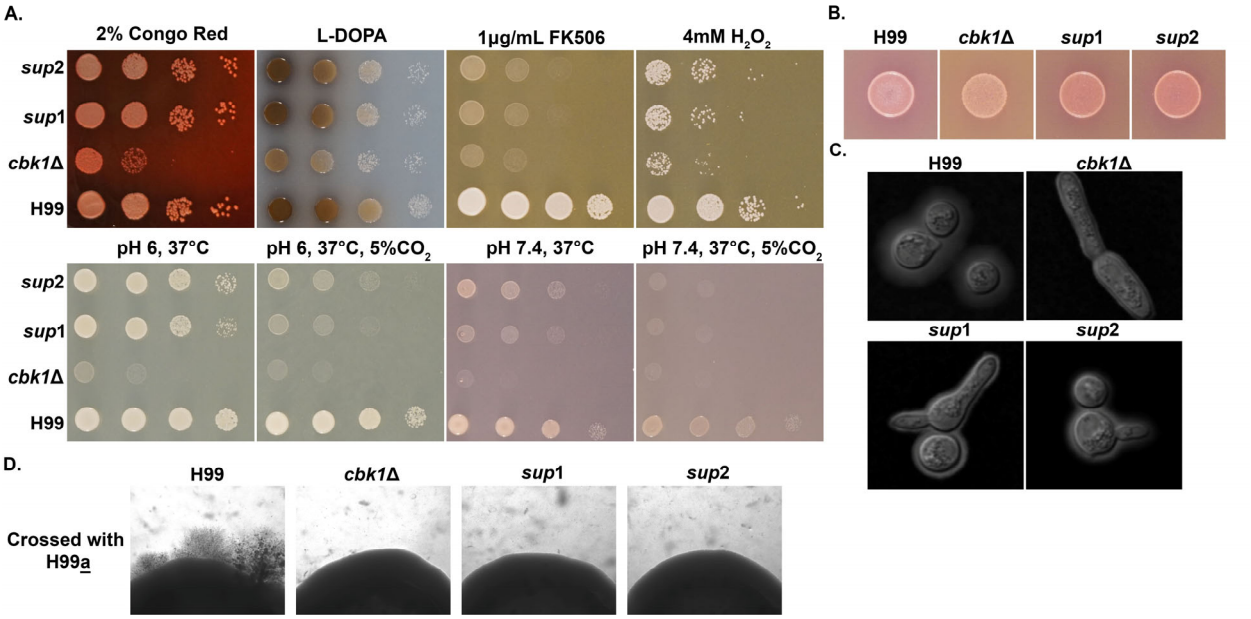

Figure S4.5. Phenotypic characterization of *cbk1*Δ suppressor mutants. (A, B) The strains above were grown overnight in YPD, serially diluted, and spotted onto the indicated solid media. YPD+2% Congo Red was used to assay cell wall stress tolerance. YPD + 1µg/mL FK506 was used to assay growth under calcineurin inhibition. YPD + 4mM H_2O_2 was used to assay oxidative stress tolerance. L-DOPA media was used to assay melaninization. RPMI media buffered with MOPS was used to test tolerance to 37˚C or 37˚C+ 5% CO_2 at pH 6 and pH 7.4. Photographs were taken two days of incubation. Christensen Urea Agar was used to assay urease activity, indicated by change in media coloration from yellow to pink. (C) The cells incubated for two days on RPMI pH 7.4, 37˚C+ 5% CO_2, were stained with India Ink and observed under the microscope to check capsule size. (D) Cells were grown overnight in liquid culture, and then

diluted to the concentration of OD_{600}=.01. Equal volumes of the indicated MAT**a** and MATα cells were mixed and 3μL was spotted onto V8 pH 5.0 solid medium. After incubation at 22˚C for 2 weeks in the dark, mating colonies were examined with a SZX16 stereoscope (Olympus).

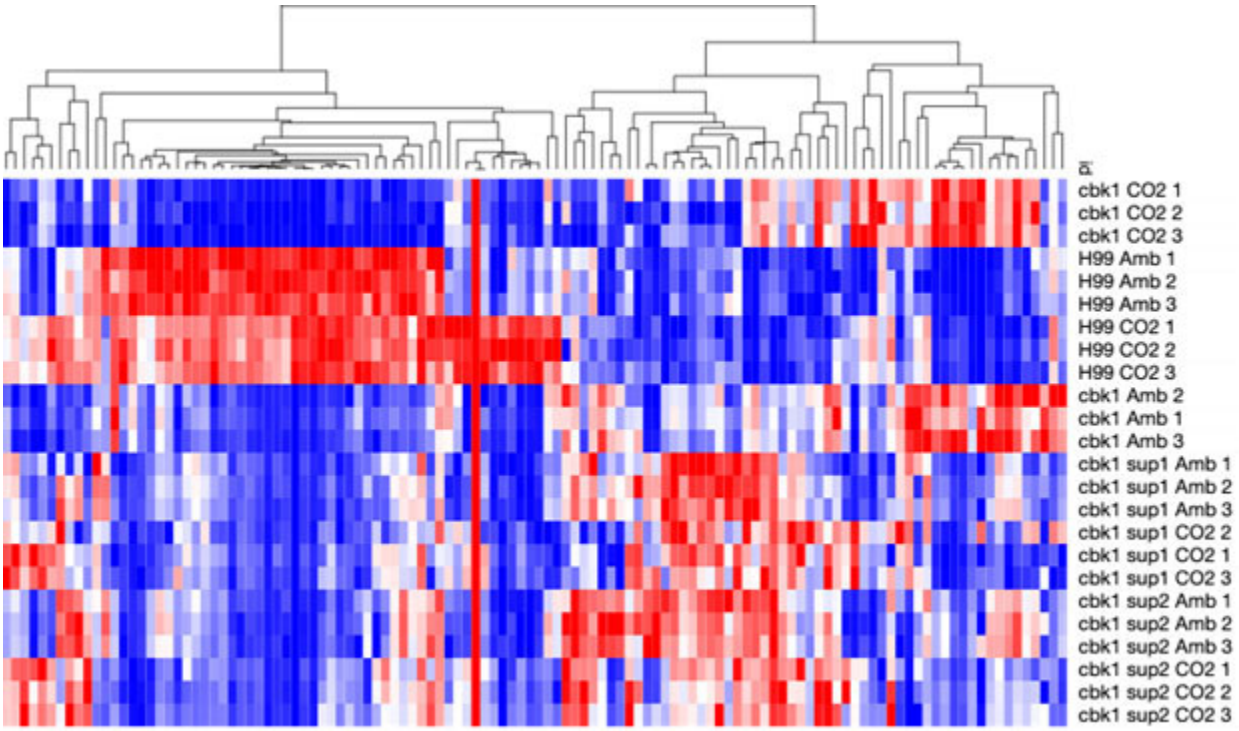

Figure S4.6. Suppressor mutants do not restore transcript levels of Nanostring targets in *cbk1*Δ. Heatmap showing normalized total RNA counts of NanoString targets in H99, *cbk1Δ*, *sup1*, and *sup2* cultured at either ambient or 5% CO_2. Red indicates higher and blue indicates lower transcript abundance.

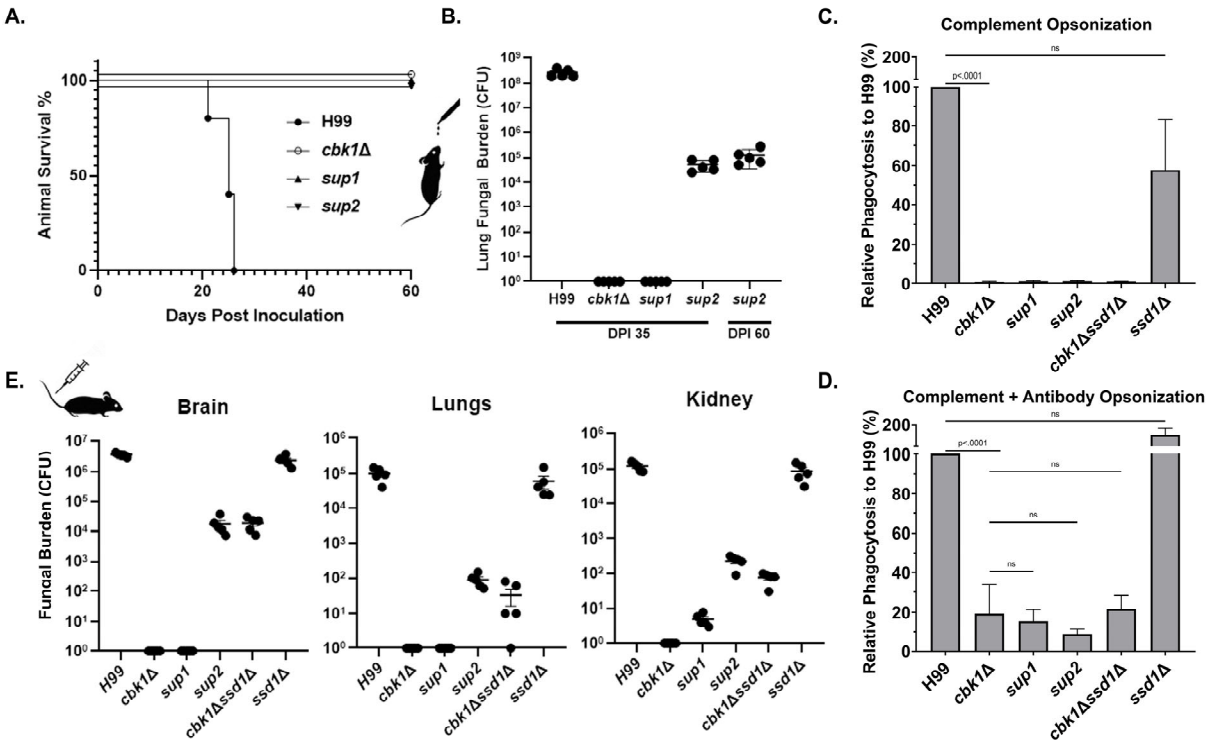

Figure 4.5. Suppressor mutants are partially restored for phagocytosis and can disseminate in the intravenous infection model of cryptococcosis. (A) Mice were infected with $1x10^4$ fungal cells intranasally, and their survival was monitored for 60 days post infection. (B) At day 35 post infection (DPI 35) and at the time of termination (DPI 60), 5 out of 10 mice per group for the *cbk1*Δ mutant, *sup1* and *sup2* groups were harvested for brains, kidneys, and lungs. For H99 infected mice, they were euthanized at their clinical end point (all before DPI 26). Tissue homogenate was serially diluted and plated onto YNB medium to count the colony forming units (CFUs) to measure the fungal burden per organ. (C) Murine macrophage J774A.1 cells were co-incubated with $2x10^6$ cryptococcal cells opsonized with serum from naïve mouse for two hours. Nonadherent or phagocytosed cells were washed, and cryptococcal cells were released and then serially diluted before plating onto YNB medium for measurement of colony forming units (CFUs). (D) The same as above, except opsonization was performed with serum of mice vaccinated against cryptococcosis. (E) Mice were challenged with $1x10^5$ cryptococcal cells

intravenously. At day 5 post infection, five mice per group were sacrificed. Brains, kidneys, and lungs of euthanized mice were dissected and homogenized. Serial dilutions were plated to count CFUs for quantification of fungal burden per organ.

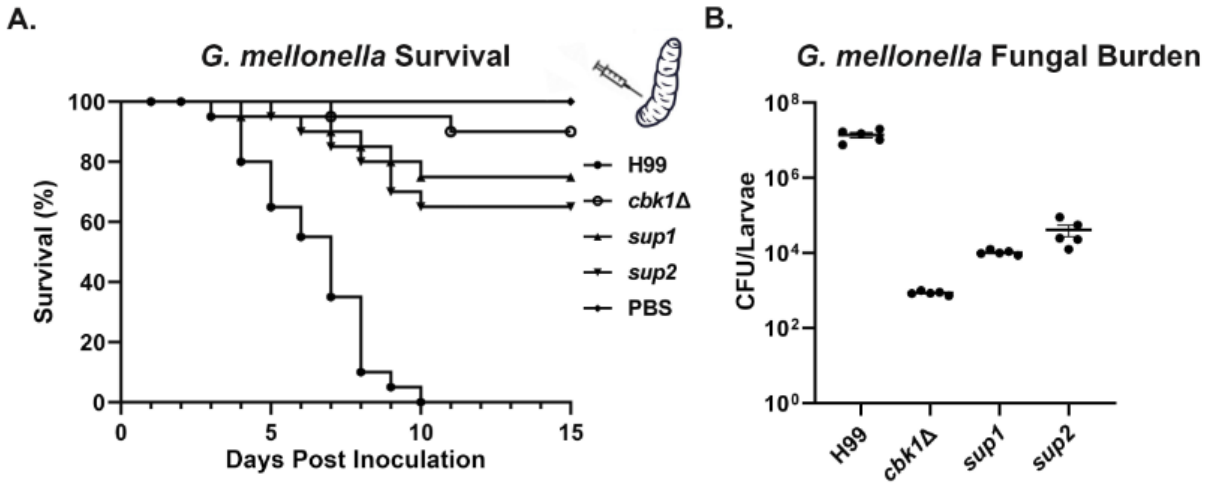

Figure 4.6. Suppressor mutants partially restore virulence in the *G. mellonella* model. (A) *G. mellonella* larvae were infected with $5x10^4$ fungal cells of the indicated strain and their survival was monitored for 15 days post inoculation. The *cbk1*Δ group survival curve was not significantly different from *sup1* (p-value =0.2) and was significantly different from the *sup2* curve (p-value = 0.05). (B) At day 5 post inoculation (DPI 5), 5 out of 25 larvae per group for the H99, the *cbk1*Δ mutant, *sup1*, and *sup2* groups were homogenized, serially diluted, and plated to count the colony forming units (CFUs) and measure the fungal burden of each larva. The fungal burden of the *sup1* and *sup2* groups were significantly higher than the *cbk1*Δ group (p-value < 0.001).

Table 3.1. Hits from forward genetic screening

Gene ID	FungiDB Description	SGD Name
CNAG_00097	myo-inositol transporter, putative	ITR1
CNAG_00293	Ras-like protein	RSR1
CNAG_00328	DNA excision repair protein ERCC-5	RAD2
CNAG_00333	hypothetical protein	N/A

CNAG_00405	ste/ste20/ysk protein kinase	N/A
CNAG_00414	Maintenance of killer protein 32, putative	MAK32
CNAG_00443	hypothetical protein	YCR023C
CNAG_00444	hypothetical protein	N/A
CNAG_00458	hypothetical protein	N/A
CNAG_00503	hypothetical protein	N/A
CNAG_00563	hypothetical protein	N/A
CNAG_00577	hypothetical protein	N/A
CNAG_00699	transmembrane receptor	N/A
CNAG_00833	hypothetical protein	N/A
CNAG_00888	calcineurin subunit B	CNB1
CNAG_00968	hypothetical protein, variant	N/A
CNAG_00991	flap endonuclease 1	RAD27
CNAG_01016	vacuolar membrane protein	MTC5
CNAG_01038	hypothetical protein	N/A
CNAG_01150	omega-6 fatty acid desaturase (delta-12 desaturase)	N/A
CNAG_01213	hypothetical protein	MDM20
CNAG_01255	hypothetical protein	N/A
CNAG_01415	cytoplasmic protein	YOR296W
CNAG_01507	protein CGI121	CGI121
CNAG_01536	myosin heavy chain	MYO1
CNAG_01575	ATP-binding cassette transporter	YCF1
CNAG_01653	cytokine inducing-glycoprotein	N/A
CNAG_01845	AGC/PKC protein kinase	PKC1
CNAG_01864	hypothetical protein	N/A
CNAG_01875	wd-repeat protein	RAV1
CNAG_01918	cytoskeletal regulatory protein binding protein	BUD6
CNAG_01936	Sugar transporter	N/A
CNAG_02232	RNA polymerase II-associated factor 1	PAF1
CNAG_02332	hypothetical protein	N/A
CNAG_02359	small subunit ribosomal protein S25e	RPS25A
CNAG_02434	Copper transport protein ATX1	ATX1
CNAG_02532	D-amino-acid oxidase	N/A
CNAG_02586	Sugar transporter	N/A
CNAG_02730	sorting nexin-41	ATG20
CNAG_03050	hypothetical protein	N/A
CNAG_03155	ENTH domain-containing protein	YAP1801
CNAG_03159	cytoplasmic protein	YAR1
CNAG_03227	hypothetical protein	N/A
CNAG_03301	mitochondrial inner membrane translocase subunit TIM13	TIM13
CNAG_03322	UDP-glucuronate decarboxylase	N/A

CNAG_03355	Two-component-like sensor kinase	N/A
CNAG_03567	RAM signaling network protein kinase, putative	CBK1
CNAG_03622	cell polarity protein mor2	TAO3
CNAG_03634	DNA-directed RNA polymerase I subunit RPA49	RPA49
CNAG_03741	hypothetical protein	N/A
CNAG_03745	hypothetical protein	DAL81
CNAG_03824	solute carrier family 25	PIC2
CNAG_03918	ram signaling network protein	N/A
CNAG_03963	tyrosine phosphatase	OCA1
CNAG_04048	53 kda brg1-associated factor b	ARP4
CNAG_04159	ariadne-1	HEL1
CNAG_04243	cell division control protein 24	CDC24
CNAG_04351	methylmalonate-semialdehyde dehydrogenase (acylating)	N/A
CNAG_04382	hypothetical protein	N/A
CNAG_04642	tetraspanin Tsp2	N/A
CNAG_04655	rab family protein	YPT52
CNAG_04693	target of rapamycin complex 2 subunit	AVO1
CNAG_04796	calcineurin a catalytic subunit	CNA1
CNAG_04853	derlin-2/3	N/A
CNAG_04951	3-deoxy-7-phosphoheptulonate synthase	ARO4
CNAG_04992	hypothetical protein	N/A
CNAG_05021	hypothetical protein, variant	REE1
CNAG_05095	pod-specific dehydrogenase SAC25	ENV9
CNAG_05114	peroxisomal copper amine oxidase	N/A
CNAG_05159	hypothetical protein	N/A
CNAG_05299	oxidoreductase	N/A
CNAG_05309	hypothetical protein	N/A
CNAG_05451	hypothetical protein	N/A
CNAG_05604	hypothetical protein	N/A
CNAG_05678	membrane protein	ADY2
CNAG_05789	hypothetical protein	ACL4
CNAG_05794	CBK1 kinase activator protein MOB2	MOB2
CNAG_05882	class E vacuolar protein-sorting machinery protein HSE1	HSE1
CNAG_05992	hypothetical protein	N/A
CNAG_05998	rho family protein	N/A
CNAG_06003	hypothetical protein	N/A
CNAG_06218	Amidase	AMD2
CNAG_06224	nuclear movement protein nudC	N/A
CNAG_06373	mitotic spindle assembly checkpoint protein MAD2B	REV7
CNAG_06376	vacuolar membrane protein	PEP5
CNAG_06529	hypothetical protein	N/A

CNAG_06583	hypothetical protein	N/A
CNAG_06589	endoribonuclease L-PSP	N/A
CNAG_06664	sorting nexin Mvp1	MVP1
CNAG_06716	hypothetical protein	MUD1
CNAG_06728	kinesin	N/A
CNAG_06796	serine/arginine repetitive matrix protein 1	N/A
CNAG_07358	hypothetical protein	N/A
CNAG_07438	3-keto sterol reductase	N/A
CNAG_07448	urea transporter, putative	DUR3
CNAG_07862	fumarate reductase	FRD1

Table 3.2. Key Resources Table

Reagent type (species) or resource	**Designation**	**Source or reference**	**Identifiers**	**Additional information**
Genetic reagent (*Cryptococcus neoformans KN99α, matα*)	WT strain: H99	[60]		
Genetic reagent (*Cryptococcus neoformans KN99α, matα*)	WT strain: H99a	[60]		
Genetic reagent (*Cryptococcus neoformans KN99α, matα*)	*cbk1*Δ	[22]	FJW9	H99alpha, *CBK1*::*NAT*^{r}
Genetic reagent (*Cryptococcus neoformans KN99α, matα*)	*mob2*Δ	[22]	FJW10	H99alpha, *MOB2*::*NAT*^{r}
Genetic reagent (*Cryptococcus neoformans KN99α, matα*)	*kic1*Δ	[22]	FJW8	H99alpha, *KIC1*::*NAT*^{r}

Genetic reagent (*Cryptococcus neoformans KN99α, matα*)	*tao3*Δ	[22]	AI136	MATalpha, *TAO3*:: *NAT*^{r}
Genetic reagent (*Cryptococcus neoformans KN99α, matα*)	*sog2*Δ	[22]	AI131	MATalpha, *SOG2*:: *NAT*^{r}
Genetic Reagent (*Candida albicans, SN250*)	SN250	[24]	SN250	HIS-, LEU-, ARG-
Genetic Reagent (*Candida albicans, SN250*)	*cbk1*ΔΔ	[24]	ΔΔcbk1	SN250, ΔΔcbk1: *HIS-, LEU-, ARG-*
Genetic reagent (*Cryptococcus neoformans KN99α, matα*)	*cna1*Δ	FGSC deletion set Plate 46 Well E12	*cna1*Δ	H99alpha *CNA1*::*NAT*^{r}
Genetic reagent (*Cryptococcus neoformans KN99α, matα*)	*cdc24*Δ	FGSC deletion set Plate 33 Well C4	*cdc24*Δ	H99alpha, *CDC24*::*NAT*^{r}
Genetic reagent (*Cryptococcus neoformans KN99α, matα*)	*mpk1*Δ	FGSC deletion set Plate 11 Well A5	*mpk1*Δ	H99alpha, *MPK1*::*NAT*^{r}
Genetic reagent (*Cryptococcus neoformans KN99α, matα*)	*CBK1*^{OE}	This study.	BC1449	H99alpha, P$_{CTR4}$-*CBK1*-mCherry-*NEO*^{r}
Genetic reagent (*Cryptococcus neoformans KN99α, matα*)	*cdc24*Δ, *CBK1*^{OE}	This study.	BC1281	H99alpha, *CDC24*::*NAT*^{r}, P$_{CTR4}$-*CBK1*-

				mCherry-*NEO*^{r}
Genetic reagent (*Cryptococcus neoformans KN99α, matα*)	*cdc24*Δ, *CBK1*^{OE}	This study.	BC1282	H99alpha, *CDC24*::*NAT*^{r}, P$_{CTR4}$-*CBK1*-mCherry-*NEO*^{r}
Genetic reagent (*Cryptococcus neoformans KN99α, matα*)	*cna1*Δ, *CBK1*^{OE}	This study.	BC1283	H99alpha, *CNA1*::*NAT*^{r}, P$_{CTR4}$-*CBK1*-mCherry-*NEO*^{r}
Genetic reagent (*Cryptococcus neoformans KN99α, matα*)	*cna1*Δ, *CBK1*^{OE}	This study.	BC1284	H99alpha, *CNA1*::*NAT*^{r}, P$_{CTR4}$-*CBK1*-mCherry-*NEO*^{r}
Genetic reagent (*Cryptococcus neoformans KN99α, matα*)	*mpk1*Δ, *CBK1*^{OE}	This study.	BC1285	H99alpha, *MPK1*::*NAT*^{r}, P$_{CTR4}$-*CBK1*-mCherry-*NEO*^{r}
Genetic reagent (*Cryptococcus neoformans KN99α, matα*)	*mpk1*Δ, *CBK1*^{OE}	This study.	BC1286	H99alpha, *MPK1*::*NAT*^{r}, P$_{CTR4}$-*CBK1*-mCherry-*NEO*^{r}
Genetic reagent (*Cryptococcus neoformans KN99α, matα*)	*cdc24*Δ, *CDC24*^{OE}	This study.	BC650	H99alpha, *CDC24*::*NAT*^{r}, P$_{CTR4}$-mNeonGreen-*CDC24*-*NEO*^{r}

Genetic reagent (*Cryptococcus neoformans KN99α, matα*)	*cbk1*Δ, *CBK1*^{OE}	This study.	BC669	H99alpha, *CBK1*::*NAT*^{r}, P$_{CTR4}$-*CBK1*-mCherry-*NEO*^{r}
Genetic reagent (*Cryptococcus neoformans KN99α, matα*)	*mpk1*Δ, *MPK1*^{OE}	This study.	BC1356	H99alpha, *MPK1*::*NAT*^{r}, P$_{GPD1}$-mNeonGreen-*MPK1*-*NEO*^{r}
Genetic reagent (*Cryptococcus neoformans KN99α, matα*)	*cna1*Δ, *CNA1*^{OE}	[61]	LK214	H99a, *CNA1*::*NEO*^{r}, P$_{H3}$-GFP-*CNA1*-*NAT*^{r}
Genetic reagent (*Cryptococcus neoformans KN99α, matα*)	*cbk1*Δ, *CDC24*^{OE}	This study.	BC1357	H99alpha, *CBK1*::*NAT*^{r}, P$_{CTR4}$-mNeonGreen-*CDC24*-*NEO*^{r}
Genetic reagent (*Cryptococcus neoformans KN99α, matα*)	*cbk1*Δ, *MPK1*^{OE}	This study.	BC1358	H99alpha, *CBK1*::*NAT*^{r}, P$_{GPD1}$-mNeonGreen-*MPK1*-*NEO*^{r}
Genetic reagent (*Cryptococcus neoformans KN99α, matα*)	*cbk1*Δ, *CNA1*^{OE}	This study.	BC1359	H99alpha, *CBK1*::*NAT*^{r}, P$_{H3}$-GFP-*CNA1*-*NAT*^{r}
Genetic reagent (*Cryptococcus neoformans KN99α, matα*)	*sup1*	This study.	BC1068	H99alpha, *CBK1*::*NAT*^{r},SUP1
Genetic reagent (*Cryptococcus neoformans KN99α, matα*)	*sup2*	This study.	BC1076	H99alpha, *CBK1*::*NAT*^{r},SUP2

Genetic reagent (*Cryptococcus neoformans KN99α, matα*)	*cbk1*Δ*ssd1*Δ	This study.	BC1239	H99alpha, *CBK1*::*NAT*^{r}, *SSD1*::*NEO*^{r}
Genetic reagent (*Cryptococcus neoformans KN99α, matα*)	*ssd1*Δ	This study.	BC1241	H99alpha, *SSD1*::*NEO*^{r}
Genetic reagent (*Cryptococcus neoformans KN99α, matα*)	*cbk1*Δ*psc1*Δ	This study.	BC1369	H99alpha, *CBK1*::*NAT*^{r}, *PSC1*::*HYG*^{r}
Genetic reagent (*Cryptococcus neoformans KN99α, matα*)	*psc1*Δ	This study.	BC1393	H99alpha, *PSC1*::*HYG*^{r}
Genetic reagent (*Cryptococcus neoformans KN99α, matα*)	*cac1*Δ	[62]	YSB42	H99alpha, *CAC1*::*NAT*^{r} STM#159
Genetic reagent (*Cryptococcus neoformans KN99α, matα*)	*aca1*Δ	FGSC deletion set Plate 32 Well H6	*aca1*Δ	H99alpha, *ACA1*::*NAT*^{r}
Genetic reagent (*Cryptococcus neoformans KN99α, matα*)	*pkr1*Δ	FGSC deletion set Plate 33 Well H7	*pkr1*Δ	H99alpha, *PKR1*::*NAT*^{r}
Genetic reagent (*Cryptococcus neoformans KN99α, matα*)	*pde1*Δ	FGSC deletion set Plate 10 Well A12	*pde1*Δ	H99alpha, *PDR1*::*NAT*^{r}
Genetic reagent (*Cryptococcus neoformans KN99α, matα*)	*pde2*Δ	FGSC deletion set Plate 11 Well H7	*pde2*Δ	H99alpha, *PDR2*::*NAT*^{r}

Genetic reagent (*Cryptococcus neoformans KN99α, matα*)	*gpa1*Δ	[63]	YSB83	H99alpha, *GPA1*::*NAT*^{r} STM#5
Genetic reagent (*Cryptococcus neoformans KN99α, matα*)	*cln1*Δ	This study.	BZ36	H99alpha, *CLN1*::*NAT*^{r}
Genetic reagent (*Cryptococcus neoformans KN99α, matα*)	*ecm2201*Δ	FGSC deletion set Plate 2 Well A10	*ecm2201*Δ	H99alpha, *ECM2201*::*NAT*^{r}
Genetic reagent (*Cryptococcus neoformans KN99α, matα*)	*kin4*Δ	Bahn Kinase Deletion Set Plate 4 Well G8 [20]	*kin4*Δ	H99alpha, *KIN4*::*NAT*^{r}
Recombinant DNA reagent	pPZP-NATcc	[64]	pPZP-NATcc	
Recombinant DNA reagent	pDD162	[65]	pDD162	
Recombinant DNA reagent	pFZ1-*CDC24*	This study.	P$_{CTR4\text{-}2}$-mNeonGreen-*CDC24*(H99)-*NEO*^{r}	
Recombinant DNA reagent	pXC-*CBK1*-mCh	This study.	P$_{CTR4\text{-}2}$-*CDC24*(H99)-mCherry-*NEO*^{r}	
Recombinant DNA reagent	LKB61	[61]	P$_{GPD1}$-mCherry-*CNA1*-*HYG*^{r}	
Recombinant DNA reagent	pUC19-*MPK1*-mNG	This study.	P$_{GPD1}$-*MPK1*-mNeonGreen-NEO^r	
Cell line	J774A.1 (ATCC® TIB-67™)	American Type Culture Collection		

Chemical Compound, drug	Hygromycin	Research Products International	Cat. NO.: H75000	
Chemical Compound, drug	G418	Research Products International	Cat. NO.: G64000	
Chemical Compound, drug	Nourseothricin	Jena Bioscience	Cat. NO.: AB-102-25G	
Software, algorithm	Graphpad Prism 9	Graphpad		
Software, algorithm	nSolver software version 4.0	NanoString Technologies		
Software, algorithm	Trim Galore v0.6.5	[49]		
Software, algorithm	BWA aligner v0.7.17	[50]		
Software, algorithm	SAMtools v1.10	[51]		
Software, algorithm	Picard Tools v2.16.0	[52]		
Software, algorithm	bcftools v1.13	[53]		
Software, algorithm	illustrator of biological sequences (IBS)	[54]		

CHAPTER 5

QTL MAPPING AND BULK SEGREGANT ANALYSIS IDENTIFIES CO_2 TOLERANCE GENES ASSOCAITED WITH VIRULENCE IN THE GLOBAL PATHOGEN *CRYPTOCOCCUS NEOFORMANS*

Benjamin J. Chadwick, Xiaofeng Xie, Laura C. Ristow, Damian J. Krysan, Xiaorong Lin, submitted to Nature Microbiology, October 4, 2023

Abstract

Cryptococcus neoformans is a ubiquitous free-living soil yeast and opportunistic pathogen that causes ~223,100 cases of cryptococcal meningitis per year, killing over 180,000 people. The pathogenicity of *C. neoformans* relies on its adaptation to the host conditions. An important difference between its natural environment and the mammalian host is the concentration of CO_2. CO_2 levels in the host fluctuate around 5%, which is ~125-fold higher than in ambient air. We recently found that while clinical isolates are tolerant to host levels of CO_2, many environmental isolates are CO_2-sensitive and virulence-attenuated in animal models. The genetic basis responsible for cryptococcal adaptation to high levels of CO_2 is unknown. Here, we utilized quantitative trait loci (QTL) mapping with 374 progeny from a cross between a CO_2-tolerant clinical isolate and a CO_2-sensitive environmental isolate to identify genetic regions regulating CO_2 tolerance. To identify specific quantitative trait genes (QTGs), we applied fine mapping through backcrossing and bulk segregant analysis coupled with pooled genome sequencing of near-isogenic progeny but with distinct tolerance levels to CO_2. The roles of the identified QTGs in CO_2 tolerance were verified by targeted gene deletion. We further demonstrated that virulence levels among near-isogenic strains in a murine model of cryptococcosis correlate with their levels of CO_2 tolerance. Moreover, we discovered that sensitive strains may adapt *in vivo* to become more tolerant to increased CO_2 levels and more virulent. These findings highlight the underappreciated role of *C. neoformans* tolerance to host CO_2 levels and its importance in the ability of an opportunistic environmental pathogen to cause disease.

Introduction

Cryptococcus neoformans is an environmental fungus and a global opportunistic pathogen, responsible for over 180,000 fatalities annually [1]. Most cases occur in immunocompromised individuals, particularly AIDS patients [2,3]. The pathogenic *C. neoformans* species complex have been differentiated based on serotypes and molecular types [4]. Most infections observed globally in clinics are overwhelmingly caused by serotype A isolates and more specifically by those with the molecular type VNI [5,6].

In 2009, Livintseva et al. reported that many *C. neoformans* environmental isolates are not lethal in mice, although sharing similar sequence types and *in vitro* phenotypes with lethal clinical isolates [7]. The *in vitro* phenotypes tested were the three classic cryptococcal virulence traits: thermotolerance (the ability to grow at 37˚C), melanin production, and encapsulation. Mukaremera et al. isolated *C. neoformans* from patients who died from the infection and from those who survived, and found that lethality of these strains in humans correlated to lethality in the murine model. However, there was no strong correlation of virulence with genome sequence types, or with *in vitro* phenotypes including encapsulation, thermotolerance, susceptibility to various cell wall stresses, antifungal heteroresistance, and cell size enlargement [7,8]. These findings suggest that an unrecognized virulence trait may have a major contribution to the aggressiveness of *C. neoformans*.

In 2019, our research group demonstrated that host temperature combined with host CO_2 concentrations is inhibitory to the growth of many cryptococcal isolates *in vitro*, and tolerance to host CO_2 levels correlates with the virulence of strains tested by Litvintseva et al [9]. CO_2 tolerance may therefore be an important factor when predicting virulence of environmental isolates. To explore the genetic regulation of CO_2 tolerance in *C. neoformans*, we recently

identified pathways and genes important for the clinical and reference strain H99 to grow at host CO_2 levels [10,11]. However, the natural genetic variation in *Cryptococcus* isolates which determine CO_2 tolerance remain unknown. Given that CO_2 tolerance is a complex genetic trait, we decided to use the power of quantitative trait loci (QTL) mapping to determine the genetic loci associated with variation in CO_2 tolerance in natural populations.

Results

Phenotypic variations in CO_2 tolerance

To generate the QTL mapping population, we crossed the CO_2 tolerant strain KN99**a** (congenic to the clinical reference strain H99) with A7-35-23α; a virulence-attenuated and CO_2 sensitive environmental strain [7]. Both are serotype A isolates with KN99 being molecular type VNI and A7-35-23 VNII. Apart from CO_2 tolerance, A7-35-23 is similar to H99 in terms of classically studied virulence factors, including thermotolerance, melanization, capsule production, susceptibility to oxidative stress, or urease activity (Figure 5.1A, B). The two strains were able to mate and produce basidiospores (Figure 5.1C), which were collected for QTL mapping. Because each meiosis in a basidium head is followed by multiple rounds of mitosis to produce four chains of spores, the random collection of spores could be enriched for clonal spores derived from the same meiotic event (Figure 5.1D). Therefore, we first genotyped the progeny using three restriction fragment length polymorphism (RFLP) markers and the mating type marker ("A": A7-35-23α allele; "K": KN99**a** allele). This gave us 16 genotype groups. We found that the frequency of each genotype was roughly similar, indicating that most of the progeny are recombinant and derived from distinct meiotic events (Figure 5.1E). One exception is the "KKA" group, which is much larger than other groups with biased enrichment of *MAT*α

(Figure 5.1F). This group is likely enriched for mitotic amplification of the same meiotic products.

Linkage mapping with SNP markers

We generated SNP markers by utilizing a double restriction enzyme digestion coupled with sequencing similar to the approach described by Elshire et al., [12]. Our individual genome coverage ranged from 5% to 67%, with a median of 15%. Overall, our genome sequencing results generated over 16,000 SNP markers in the F1 population, covering a majority of the genome (Figure 5.2A). The sequences confirmed that nearly ~98% of the progeny collected were indeed recombinant (Figure 5.2B). A group of recombinant progeny sharing identical sequences (indicated with an arrow in Figure 5.2B**)** correspond to the "KKA" group (Figure 5.1F), consistent with the idea that mitotic amplification of meiotic products in spore chains could yield biased representation of some recombinant progeny from a random collection of spores.

To examine the presence of chromosome arrangements differentiating the two parents, we generated a chromosome-level genome assembly of A7-35-23 using long-read Oxford Nanopore Sequencing. The assembled genome of A7-35-23 was approximately 18.8 Mb, consisted of 14 nuclear contigs (chromosomes) and 1 mitochondrial genome, and was largely syntenic to the established genome of H99 [13] (Figure 5.2D). A7-35-23 carries a reciprocal chromosomal translocation between chromosome 3 and 11, relative to H99 (Figure S5.1, Figure S5.2, and Figure S5.3). Karyotype variations among cryptococcal isolates are not uncommon based on earlier studies [14,15].

We reduced our SNP marker list to facilitate genetic mapping by removing co-segregating markers and consolidating SNPs within a 500bp distance, using a pipeline developed by Qi et al. [16]. The R/qtl software was used to estimate the genetic distance between SNP

markers and generate the linkage map [17] (Figure 5.2C). Based on our genetic map, the ratio of physical to genetic distance was 24.9 kb/cM for this inter-molecular type cross (a cross between molecular types), which is higher than those seen in crosses between isolates of the same molecular type (4.69-13.2 kb/cM) [18-20], and lower than the one observed from an inter-serotype cross (63.5kb/cM) [21]. This result is consistent with the idea that recombination rates decrease as genome divergence increases.

QTL analysis of CO_2 tolerance on YPD and RPMI

We next tested the CO_2 tolerance of the F1 progeny. We used a spotting dilution assay in which progeny were diluted to an equal cell density, spotted onto RPMI and YPD media, and incubated at 37˚C with or without 10% CO_2. Scores ranging from 0.0-1.0 were given to progeny based on their growth in 10% CO_2 compared to their growth in ambient air (see methods). The spotting assays were replicated 3 times and the average of the scores were used as the final score. A larger variation in CO_2 tolerance was observed in the mammalian cell culture RPMI media than in the nutrient rich YPD media (Figure 5.3A), indicating that media nutrition has a large impact on CO_2 tolerance. In either condition, there are progeny that grew worse in CO_2 than the sensitive parent A7-35-23 (Figure 5.3D, red line), or better than the tolerant parent KN99 (Figure 5.3D, blue line). This transgressive segregation pattern indicates that growth at high levels of CO_2 is likely controlled by multiple genetic loci, and that the CO_2 tolerant strain KN99 may also contain a CO_2 sensitive allele(s).

We next performed QTL analyses with the R/qtl package with the genotype and phenotype information using single marker regression, interval mapping, composite interval mapping, or multiple interval mapping, which all led to similar results. The QTL analysis for CO_2 tolerance on YPD media revealed two significant loci on chromosomes 2 and 12, while the

QTL analysis on RPMI media revealed significant loci on 10 different chromosomes (Figure 5.3B, Tables 4.1 and 4.2). The difference is consistent with the difference in variation in the CO_2 scores for each medium. Of interest, the significant loci on chromosome 12 for both YPD and RPMI overlap, indicating this region is important for CO_2 tolerance regardless of the media used. Although the LOD (log of the odds index) score peaks for chromosomes 2 and 7 on YPD are not above the significance threshold, they overlap with significant loci found in the RPMI condition. Thus, it seems that some genetic loci have conserved roles in CO_2 tolerance regardless of growth media. In general, the KN99 alleles for the significant loci provide greater CO_2 tolerance for the progeny except for the QTL on chromosome 7 (Figure 5.3C). This chromosome 7 allele therefore likely explains in part the transgressive segregation of CO_2 tolerance observed in the F1 progeny.

The significant peaks on chromosomes 1, 3, 9, 11, 12, and 14 are too large to identify the quantitative trait genes associated with CO_2 tolerance. The QTL regions on chromosomes 2, 7, and 8 only contained two, three, and four genes respectively. We utilized the deletion set made by the Madhani lab to test the available mutants of these genes [22].

Of the four genes in the chromosome 8 peak, deletion of *CNAG_03196* caused CO_2 sensitivity. This gene encodes for Ura5 in the pyrimidine biosynthesis pathway[23]. Similarly, we found the Ura4 encoding gene, *CNAG_00734*, in the chromosome 1 QTL (~20kb region). To examine the role of pyrimidine biosynthesis genes in CO_2 tolerance, we tested four available mutants *ura2*Δ, *ura4*Δ, *ura5*Δ, and *ura10*Δ. Growth via spotting assays was observed for host temperature and CO_2 tolerance on RPMI, RPMI + uracil and uridine, and YPD. Apart from the *ura10*Δ mutant, the other three uracil biosynthesis gene knockout mutants were unable to grow on RPMI or on the minimal YNB media without supplementation of uracil and uridine (Figure

5.4A, B). In *S. cerevisiae*, both Ura5 and Ura10 catalyze the same reaction from orotate to orotidine-5'-phosphate, but Ura5 is the major enzyme [24]. This is likely also the case in *C. neoformans*. The *ura5*Δ was temperature sensitive, but it was also sensitive to CO_2 at 30˚C on YPD media. The *ura10*Δ mutant was not temperature sensitive but displayed CO_2 sensitivity both at 30˚C and 37˚C regardless of uracil and uridine supplementation. This finding further differentiates the biological roles of the Ura5/10 paralogs, as Ura5 appears to be more critical for thermotolerance and uracil biosynthesis, while Ura10 has a more specific role in CO_2 tolerance. The *ura2*Δ mutant was sensitive to host levels of CO_2 at 30˚C and was also sensitive to 37˚C (Figure 5.4A). The *ura4*Δ mutant was slightly CO_2-sensitive at 37˚C on the supplemented RPMI media and failed to grow at 37˚C on YPD media. Interestingly, according to the transcriptomic data we previously generated of H99 and A7-35-23 in RPMI with and without 5% CO_2 [11], the transcript levels of *URA4, URA5*, and *URA2* are higher in H99 relative to A7-35-23 in the presence of 5% CO_2 (Figure 5.4C).

To examine if the difference in growth on RPMI and YPD of the F1 progeny depends on which parent's *URA4* (Chromosome 1 QTL) and *URA5* (Chromosome 8 QTL) allele they inherited, we plotted the CO_2 tolerance growth score of each progeny on RPMI against their score on YPD media and categorized them based on which *URA* alleles they carry. Interestingly, progeny with the A7-35-23 allele for both *URA4* and *URA5* ($URA4^A/URA5^A$) showed almost no correlation in growth between RPMI and YPD ($R^2 = 0.01$), while progeny with both KN99 alleles ($URA4^K/URA5^K$) had a much stronger correlation ($R^2 = 0.36$). For progeny with one allele from A7-35-23 and one from KN99, the correlation was stronger for progeny with genotype $URA4^K/URA5^A$ ($R^2 = 0.17$) than $URA4^A/URA5^K$ ($R^2 = 0.07$), indicating the *URA4* allele from KN99 has a stronger impact on the correlation of growth at 37˚C + 5% CO_2 between RPMI and

YPD media than the *URA5* allele from A7-35-23. Supporting this, the LOD score for the chromosome 1 QTL where the *URA4* gene resides was also higher than the LOD score of the chromosome 8 QTL containing the *URA5* gene (6.8 vs. 4.9). The results presented above suggest the pyrimidine biosynthesis pathway may play an important role for integrating nutritional signals with growth at host temperature and CO_2 levels.

Of the two genes in the chromosome 2 QTL, *CNAG_03644* and *CNAG_03645*, deletion of *CNAG_03644* did not render CO_2-sensitivity. The *CNAG_03645* deletion mutant does not exist in the deletion set and we also failed in deleting this gene. Its homolog *NAN1* in *S. cerevisiae* is an essential gene encoding for a U3 snoRNA binding protein localizing to both the nucleolus and the peroxisome, an organelle important for detoxification of oxidative stress and lipid metabolism. Interestingly, the *CNAG_03645* gene showed nearly 4x more SNPs than the average frequency (~15 SNPs/Kb), and is upregulated 3-fold in H99 in response to CO_2 but is not induced in A7-35-23 (Figure 5.4C) [11]. It is possible that higher expression of *CNAG_03645* may contribute to CO_2 tolerance.

The chromosome 7 peaks overlapped for both YPD and RPMI conditions. Of the 3 genes in the peak (*CNAG_05705-05707*), loss of *CNAG_05706* caused CO_2 and temperature sensitivity on both YPD and RPMI media (Figure 5.3E). *CNAG_05706* contains 16 missense mutations. *CNAG_05706* encodes for a protein homologous to Eos1 in *S. cerevisiae*, an ER membrane protein with a role in oxidative stress tolerance and N-glycosylation [25]. Polymorphism in Eos1 could impact cell wall and membrane important for CO_2 tolerance.

Bulk segregant analysis reveals quantitative trait genes controlling CO_2 tolerance.

Although we were able to identify candidate genes contributing to the narrow QTLs on chromosomes 1,2,7, and 8, we decided to fine map some of the large QTLs covering many

genes. To that end, we utilized a backcrossing strategy to reduce the number of SNPs while maintaining differences in CO_2 tolerance among progeny (Figure 5.5A). To confirm the success of our backcrosses to KN99, we visualized the karyotypes of the two ancestral strains and the backcross progeny through contour-clamped homogenous electric field (CHEF). The karyotypes of A7-35-23 and KN99 were distinct, likely due to the larger chromosome 11 and smaller chromosome 3 of A7-35-23 (Figure 5.5B), consistent with the comparison with our assembled genome (Figure 5.2D). After 3 backcrosses, the karyotypes of KN99 and the BC_3 progeny were visually identical.

The final cross yielded near-isogenic BC_4 progeny. We placed them into three groups based on their CO_2 tolerance for bulk segregant analysis (BSA). The "Sensitive" group displayed CO_2 sensitivity at both 30˚C and 37˚C, similar to the parent strain BC_3. The "S37˚C" group displayed CO_2 sensitivity only at 37˚C, and the "Tolerant" group grew similarly to KN99 in all conditions tested (Figure 5.5C). We then pooled genomic DNA from 20-30 progeny per group for whole genome sequencing to identify the allele differences between progeny with differing phenotypes. We calculated and plotted the allele difference using the SNP markers between "Sensitive" and "S37˚C", and between "S37˚C" and "Tolerant" (Figure 5.5D). Allele difference was calculated as the absolute value of the difference between the KN99 allele (SNP) frequency in the groups compared. ~4,500/5,000 of the total SNPs in the population were present on the non-syntenic region of chromosome 11, likely caused by lack of recombination observed between these two regions in the F1 progeny due to chromosomal rearrangement that differentiates the parents. With the reduced number of SNPs in the population, we were able to map the significant polymorphisms to one gene per region, except for the chromosome 3 and 11 peaks, which maintained a relatively high SNP density. The significant polymorphisms identified

on chromosomes 3, 4, 11, and 12 through BSA overlapped with significant polymorphisms identified from the QTL mapping of F1 progeny (red in Figure 5.5D). In addition, we identified significant polymorphisms on chromosomes 1, 7, 10, and 14, which were not significant in our QTL mapping results. As shown in Table 5.3, the KN99 allele for 3/9 of the genes has a negative effect on CO_2 tolerance, consistent with our earlier observation indicating the existence of KN99 alleles contributing to CO_2 sensitivity.

To confirm the role of these quantitative trait genes (QTGs) identified from BSA in CO_2 tolerance, we generated and obtained knockout mutants in both parental strains KN99 and A7-35-23 (Figure 5.5E, F). Overlapping with the chromosome 3 QTL, significant SNPs from the BSA were present in *PCL5* and *CLC1*. Deletion of *CLC1*, but not *PCL5*, caused CO_2 sensitivity in both backgrounds indicating that *CLC1* is the QTG at this locus. Deletion of *LHP1* on chromosome 10 and *CNAG_06529* on chromosome 7 also caused host temperature and CO_2 sensitivity in both strain backgrounds. However, deletion of *RAD57* (Chr. 11) and *CNAG_06181* (Chr. 12) did not affect A7-35-23 CO_2 tolerance, although they did have negative effects on KN99 CO_2 tolerance. This result suggests that *RAD57* and *CNAG_06181* might already have reduced function in A7-35-23.

To determine if differences in CO_2 tolerance among the near isogenic BC_4 progeny are due to transcriptomic differences, we did transcriptome profiling of three sensitive BC_4 progeny and three tolerant BC_4 progeny cultured at 37˚C with either ambient or 5% CO_2 using NanoString on a set of 118 genes selected based on our previous RNA sequencing experiments with multiple strains including KN99 and A7-35-23[10,11]. Overall, we did not find expression patterns that distinguish the CO_2-tolerant from the CO_2-sensitive BC_4 progeny (Figure S5.4).

Interaction between multiple genetic loci contributes to CO_2 tolerance

Our QTL analysis results imply that CO_2 tolerance is a result of the effect of many alleles (Figure 5.3). Further, we detected five significant interactions among QTLs on RPMI media, between the chromosome 2 and 11 QTLs, 3 and 11, 9 and 11, 3 and 9, and 11 and 12 (Figure 5.6A). Notably, the QTLs on chromosome 3 and 11 co-segregated in the progeny, therefore having an enhanced effect on CO_2 tolerance. Thus, the interactions between the QTL on chromosome 9 with either chromosomes 3 or 11 QTLs represent interactions between 3 loci in the population. While the most significant loci on chromosome 7 of the YPD QTL analysis did not reach the significance threshold of $p < .05$, interaction between this allele and the QTL regions on chromosomes 2 and 12 had a strong effect on growth in CO_2. To further confirm such interaction with the identified QTGs on chromosomes 3, 7, 11 and 12, we generated double knockout mutants. We found that double deletion of QTGs on chromosomes 3 and 11 (*rad57*Δ*clc1*Δ), QTGs on chromosomes 11 and 12 ((*CNAG_06181*Δ*rad57*Δ), and QTGs on chromosomes 7 and 12 (*CNAG_06181*Δ*eos1*Δ), all resulted in increased sensitivity to host temperature and CO_2. This result matches the additive effects based on our QTL pairwise analysis.

CO_2 tolerance is a crucial virulence factor

We previously observed a positive correlation between CO_2 tolerance and virulence in natural isolates of *C. neoformans*, but a direct link between the two has not been established [9]. Here we utilized 10 near-isogenic BC_4 progeny strains with the only observable phenotypic difference in CO_2 tolerance to answer this question (Figure S5.5). We infected outbred CD-1 mice intranasally with 5 CO_2 tolerant and 5 CO_2 sensitive progeny with the highly aggressive parental strain KN99 as a control. We monitored the mice for 40 days after infection. Half of the mice infected with the control strain KN99 had become moribund by day 25 (Figure 5.7B). 72%

(36/50) of the mice infected with CO_2-tolerant progeny succumbed to infection between day 14 and 34 post infection (DPI). In comparison, only 10% (5/50) of the mice infected with CO_2-sensitive strains succumbed to infection during the study period.

Several mice infected with CO_2-sensitive strains died from the infection, and we wondered if these originally sensitive strains became tolerant to CO_2, enabling them to cause disease. To test this, we isolated multiple cryptococcal cells from a mouse succumbed to infection at DPI 21 by the CO_2-sensitive strain S3. Interestingly, all isolates that recovered from this mouse showed enhanced tolerance to 5% CO_2 compared to the original S3 strain (Figure 5.7D). We pooled and sequenced their genomic DNA, and detected allele differences throughout the genome compared with the original strain (Figure 5.7C). The most striking difference in the evolved isolates was within the chromosome 10 QTL identified in the BSA (Figure 5.7C). The candidate QTG in this locus is *LHP1*, which we showed earlier for its importance in thermotolerance and CO_2 tolerance. *LHP1* contained multiple indels among pooled sequences in the 3'UTR (Table 5.3). Notably, one of the indel mutations was the same 3' UTR variant at position 1,006,927 from the BSA, suggesting that some isolates had mutated to an allele more similar to KN99.

Taken together, these data support that CO_2 tolerance is an important virulence factor in the murine model of cryptococcosis and supports the contribution of the chromosome 10 QTL in CO_2 tolerance and virulence.

Discussion

As an environmental fungus, the ability for *Cryptococcus* to adapt to mammalian host physiological conditions is a prerequisite to cause disease. We previously found that the host level of CO_2 (~125x higher than ambient air) is inhibitory to the growth of many environmental isolates [9], a discovery that is not unexpected and yet unrecognized. How clinical isolates have

adapted to higher concentrations of CO_2 remains a mystery. Here, we showed that a previously CO_2 sensitive strain can adapt to higher levels of CO_2 within 21 days in the animal host (Figure 5.7). It is therefore plausible that environmental strains can evolve *in vivo* to become CO_2 tolerant. Alternatively, a small proportion of environmental isolates may experience and adapt to high levels of CO_2 found in certain natural environments [26-30].

In this study, we found that CO_2 tolerance is a complex trait. Even among near-isogenic strains, there remains a large variation in CO_2 tolerance explained by more than 9 loci identified from our bulk segregant analysis (Figure 5.5). Interestingly, our NanoString RNA profiling did not reveal major transcriptomic differences between the near-isogenic CO_2-tolerant and CO_2-sensitive BC_4 progeny. We observed a similar phenomenon previously where there is no transcriptome restoration in the CO_2-tolerant suppressor mutants of the originally CO_2-sensitive *cbk1*Δ mutant [10]. In that case, the *cbk1*Δ suppressor mutations were identified in RNA binding proteins. We proposed and are currently testing the hypothesis that post transcriptional regulation is critical for partial restoration of CO_2-tolerance in the *cbk1*Δ mutant. Here, we found that deletion of the chromosome 10 QTG *LHP1* caused CO_2 sensitivity both on YPD and RPMI media. Furthermore, mutations in this gene and neighboring genes were found in the *in vivo* evolved isolates which gained CO_2 tolerance. *LHP1* encodes for a protein containing an LA motif RNA-binding domain. Characterized proteins containing this domain function in regulation of RNA processing or translation [31]. Lhp1 was previously characterized as a potential calcineurin target regulating thermotolerance and virulence[32]. Consistent with this, we previously identified the calcineurin pathway in our screen for CO_2 sensitive mutants[10]. *LHP1* was also found to be one of the 16 proteins overproduced in dormant "viable but non-culturable cells" [33]. In that study, to reach non-replicative dormancy, cells were grown for 8 days in hypoxic

conditions, which were enriched for CO_2. Future research is needed to determine and possibly differentiate the specific roles of *LHP1* in thermotolerance, hypoxia, and host CO_2 response.

One common theme of recent QTL mapping studies is the observation of pleiotropic virulence regulation. For example, polymorphisms in the guanine exchange factor *Ric8* have been associated with titan cell formation, thermotolerance, oxidative stress resistance, capsule production, and melanization [34,35]. In our QTL mapping and bulk segregant analysis, in addition to Lhp1 which we described above, we also identified polymorphisms in *CLC1,* which encodes a putative voltage gated ion channel important for calcium homeostasis [36]. In a previous study, disruption of *CLC1* led to loss of melanization, reduced capsule production, reduced growth at elevated pH, and virulence attenuation [37]. Many defects of the *clc1*Δ, such as defects in thermotolerance, could be rescued by calcium supplementation [36]. This relationship between calcium homeostasis and virulence traits like thermotolerance and CO_2 tolerance further emphasizes the critical role of the calcineurin pathway in cryptococcal pathogenesis.

Previous studies hint at connections between the pyrimidine biosynthesis pathway and CO_2. For example, uridine auxotrophic mutants of *Neurospora crassa* and *Escherichia coli* can grow without addition of uridine in high CO_2 [38,39]. One connection could be through the pyrimidine ring precursor molecule carbamoyl phosphate, which requires carbon dioxide for its synthesis. Interestingly, we found that growth of the knockout mutant of carbamoyl phosphate synthetase, *ura2*Δ, was greatly inhibited by CO_2 at 30˚C (Figure 5.4A). Furthermore, two of the QTGs identified in our study are involved in pyrimidine biosynthesis (Ura4 and Ura5). It is therefore possible that CO_2 inhibits growth of the pyrimidine biosynthesis mutants in *C. neoformans* due to disturbance in carbamoyl phosphate metabolism. Alternatively, but not exclusively, CO_2 may indirectly regulate pyrimidine biosynthesis through other upstream

signaling pathways. For instance, the TOR signaling pathway in mammalian cells regulates pyrimidine biosynthesis through phosphorylation of carbamoyl phosphate enzyme CAD [40,41] and our recent study found that the TOR pathway is critical for *C. neoformans* growth at host CO_2 levels [11].

In conclusion, here we showed that cryptococcal growth at host levels of CO_2 is related to polymorphisms and combination effects of multiple genetic loci. This finding suggests that environmental isolates have more than one way to adapt and become CO_2 tolerant once introduced into the host. As we previously showed that CO_2 potentiates antifungal agents that target biosynthesis of ergosterol or sphingolipid [9], it is important to investigate how current antifungal treatment shapes the evolution of *C. neoformans in vivo*. It is our conviction that future antifungal drug development should also consider the effect of host level CO_2 on antifungal activity and drug resistance/tolerance.

Materials and methods

Strains used and growth conditions

The genotypes of parental and mutant strains are detailed in Table 5.4. *Cryptococcus* strains were stored at -80˚C in 15% glycerol and grown on YPD medium unless otherwise specified. The H99 congenic pair strain KN99**a** was used for crosses with A7-35-23 and generating backcross progeny [42,43] Parental strains were mated on V8 media (5% V8 juice, 0.5g/L KH_2PO_4, 4% agar, and pH adjusted to 5 using 5M KOH) for ~3 weeks at 22˚C in the dark, until basidiospore chains were observable under microscope. The basidiospores were collected using a loop and plated onto YPD media. Germinated spores were then stored in individual cryotubes and 96-well plates in 15% glycerol at -80˚C for later phenotyping.

Phenotyping F1 progeny

F1 progeny in 96-well plates were cultured in YPD medium overnight and then diluted to OD_{600} = 0.1 (measurements taken with BioTek plate reader Epoch2) in water. Cells were then serially diluted and spotted onto YPD and RPMI agar media, and incubated at 30˚C, 37˚C, and 37˚C + 10% CO_2. For each condition tested, progeny were scored on a 1-5 scale, with 1 being the worst and 5 being the best. The progeny growth score at 37˚C was normalized to the growth score at 30˚C, and the growth score at 37˚C + 10% CO_2 was normalized to the score at 37˚C resulting in scores between 0.0-1.0. Each phenotypic assay was done in triplicates, and scores were averaged to generate the final score.

Genotyping with PCR and RFLP markers

Progeny from the cross between KN99a and A7-35-23 were cultured in liquid YPD and DNA was extracted using the cetyltrimethylammonium bromide (CTAB) method as described previously [13]. We utilized three PCR-RFLP markers and mating type specific primers to analyze the progeny from a cross between KN99 and A7-35-23. The primers used are listed in Table 5.5. First, genomic DNA of each progeny was used to PCR amplify products. PCR products were then digested with the restriction enzyme *Bgl*II and resolved on 1% agarose gels to assay the genotypes. Primers targeting S*TE20*α and *SXI2***a** were used to determine mating type of the progeny [44].

Genomic sequencing

All sequencing data was submitted under BioProject#: PRJNA1014009. To extract genomic DNA, strains were cultured in liquid YPD overnight and DNA was extracted using the CTAB method as described previously [13]. Whole genome sequencing for BSA was performed by Novogene, USA, on the Illumina platform NovaSeq6000.

The A7-35-23 Nanopore DNA library was prepared using the SQK-LSK108 kit per the manufacturer's guidelines. Sequencing was carried out using the FLO-MIN106 flow cell and was run for 48 hours. The Oxford Nanopore MinKNOW software was utilized for live base-calling. Canu version 2.1.1 [45] with default setting was used for the initial assembly, followed by mapping the A7-35-23 Nanopore reads to the assembled genome with Minimap2 version 2.17 [46], polishing with Racon version 1.4.13 [47], generating consensus with Medaka version 1.2.3 (https://github.com/nanoporetech/medaka), mapping the A7-35-23 Illumina reads to the polished genome with BWA version 0.7.17 [48] and SAMtools version 1.10 [49], and polishing again with Pilon version 1.24 [50]. The last two steps (mapping and polishing) were repeated 5 times until the polishing made no changes.

For genotyping the F_1 progeny for QTL analysis, DNA sequencing was performed at Georgia Genomics and Bioinformatics Core using a genotyping-by-sequencing approach adapted from Elshire et al., [12]. In brief, DNA samples were digested with *Hpa*II and *Nde*I. Oligos for barcoding were ordered from IDT. Adapter ligation was performed using T4 ligase from NEB (Cat# M0202L) and PCR amplification of libraries was performed with NEB 5x PCR Master Mix (Cat# M0285L). The final libraries were sequenced on NextSeq high output flow cells with 150 read 1 cycles.

SNP calling and QTL analysis

Low quality ends of sequencing reads were trimmed using Trim Galore version 0.4.5 [51] and were aligned to the KN99 reference genome (FungiDB version 50) using the BWA-MEM algorithm of the BWA aligner version 0.7.17 [48]. The GATK pipeline version 4.1.2.0 was used to call SNPs and create a combined genotype file for all progeny [52]. SNPs were further processed using python scripts developed by Qi et al., [16]. "SNP_cosegregration.py" was used to remove co-

segregating markers. “SNP_Genotyper.py” was used to score SNPs (described below), filter SNPs with a per sample read depth less than 3, and consolidate SNPs within a 500bp distance of each other to reduce the number of markers for computing. SNPs were scored as A (KN99 genotype), B (A7-35-23 genotype), H (Heterozygous), C (ambiguous B or H), and D (ambiguous C or H). As no progeny were heterozygous, we removed SNPs scored as H, C, or D. SNPs that were missing in over 30% of the progeny were removed. Clonal progeny and progeny with over 30% missing marker information were also removed before genetic map construction.

QTL analysis was then carried out using the R package r/QTL [17]. The map function “kosambi” was used to calculate the genetic distance between markers anchored by their physical distance. Interval mapping was performed using the Haley-Knott regression with 1,000 permutations to calculate the LOD significance threshold. The Haley-Knott regression was also used to calculate pairwise interactions. Figures for the allele differences and LOD scores were generated using CMplot [53] and boxplots were generated by GraphPad Prism 9.

Pulse-field gel electrophoresis

Pulse-field gel electrophoresis was performed as described previously [54-56]. Strains were grown overnight in 10 mL YPD medium at 30˚C with 225 rpm shaking and then diluted 500x in YNB + 1M NaCl and continued to grow until reaching OD_{600} = 0.6-1.0. The cells were washed twice with a 0.5M NaCl + 50mM EDTA pH 8 solution and stored on ice. The cell pellets were then resuspended in 0.5% low melting agarose with 25 mg/mL lysing enzymes (Lysing enzymes from *Trichoderma harzianum*, Sigma-Aldrich), and molded to create the agarose plugs using CHEF Disposable Plug Molds from BioRad. The plugs were incubated overnight at 37˚C in 700 µl of buffer containing 500 mM EDTA, 10 mM Tris, pH 7.5. 400 µL of a solution containing 5% sarcosyl and 5 mg/mL proteinase K in 500mM EDTA pH 7.5 was added to the samples and

incubated at 50˚C for 12 hours with periodic inversion. The agarose plugs were washed with buffer containing 20 mM Tris, 50 mM EDTA, pH 8, before being stored at 4˚C.

The contour-clamped homogenous electric field (CHEF) method was carried out using a CHEF Mapper XA system (BioRad) on a 1% agarose gel in 0.5x TBE maintained at 14˚C. The system was run with a gradient of 6.0 V/cm and a linear ramp switch time of 90.5 - 266 seconds for 38.5 hours with an included angle of 120˚. Gel images were obtained using a ChemStudio imager (Analytik).

Genetic manipulations

To generate knockout mutants not already present in the FGSC *Cryptococcus* deletion collections, TRACE (Transient CRISPR-Cas9 Coupled with Electroporation) was utilized to disrupt target genes as we described previously [57,58]. Diagnostic PCR with open reading frame primers were used to confirm disruption of target genes. Details on the primers used for each mutant are in Table 5.5. Guide RNA target sequences were identified using the FungiDB Eukaryotic Pathogen CRISPR guide RNA/DNA Design Tool [59]. Transformants were selected on YPD medium with 100 μg/mL of Nourseothricin (NAT), 100 μg/mL of Geneticin (G418), or 200 μg/mL of Hygromycin (HYG).

NanoString RNA profiling

Overnight cultures of the *C. neoformans* strains were plated onto RPMI media buffered with MOPS to pH 7.0 and incubated at 30˚C with ambient levels of 5% CO_2 for 24 hours. After 24 hours, the cells were harvested, frozen in liquid nitrogen, and lyophilized. Lyophilized cells were disrupted for 45 seconds with 0.5 mm glass beads on an MP Biomedicals FastPrep-24 benchtop homogenizer. The Invitrogen PureLink RNA mini-kit with on-column DNAse treatment was used according to the manufacturer's instructions for RNA extraction. The

NanoDrop OneC spectrophotometer was used to quantify the RNA, and a total of 100 ng per sample was combined with a custom probe set from NanoString Technologies according to the manufacturer instructions. Hybridization was performed at 65°C for 18 hours, before being run on a NanoString nCounter Pro Analysis System according to manufacturer instructions. The software nSolver (version 4.0) was used to extract the data from Reporter Code Count and raw counts were exported to Microsoft Excel. Internal negative controls were used to subtract background from raw counts (negative control average +2 SDs). The Counts were normalized across samples by total RNA counts, and probes below the background level were set to a value of 1. Morpheus (https://software.broadinstitute.org/morpheus/) was used to generate the heat map with hierarchical clustering, one minus Pearson correlation, average linkage method, and clustered according to rows and columns.

Intranasal infection model of cryptococcosis

Cryptococcal cells were grown overnight in liquid YPD at 30˚C and washed three times with sterile saline, enumerated by hemacytometer, and diluted to a concentration of 2 x 10^6 cells/mL. CD-1 female mice (Charles River Laboratories) with body weight of 25 to 30 grams were sedated with ketamine and xylazine via intraperitoneal injection and inoculated intranasally with 1 x 10^5 cells/animal (50 µL) as previously described [10,60-64]. Mice were monitored daily for disease progression and surviving animals were euthanized at DPI 40.

Ethical statements

This study was performed according to the guidelines of NIH and the University of Georgia Institutional Animal Care and Use Committee (IACUC). The animal models and procedures used have been approved by the IACUC (AUP protocol number: A2023 03-033)

Acknowledgments

This work was supported by National Institutes of Health (http://www.niaid.nih.gov) (R01AI147541 to DJK and XL) and University of Georgia Gene E. Michaels fund to XL. The funders had no role in study design, data collection, and interpretation, or the decision to submit the work for publication. We thank all Lin lab members and the UGA fungal group for their helpful suggestions.

References

1. Rajasingham, R. *et al.* Global burden of disease of HIV-associated cryptococcal meningitis: an updated analysis. *The Lancet Infectious Diseases* **17**, 873-881 (2017).
2. Casadevall, A. & Perfect, J.R. *Cryptococcus Neoformans*, (ASM Press, 1998).
3. Zhao, Y., Lin, J., Fan, Y. & Lin, X. Life cycle of *Cryptococcus neoformans*. *Annual Review of Microbiology* **73**, null (2019).
4. Cogliati, M. Global molecular epidemiology of *Cryptococcus neoformans* and *Cryptococcus gattii*: an atlas of the molecular types. *Scientifica* **2013**, 675213-675213 (2013).
5. Litvintseva, A.P., Thakur, R., Vilgalys, R. & Mitchell, T.G. Multilocus sequence typing reveals three genetic subpopulations of *Cryptococcus neoformans* var. *grubii* (serotype A), including a unique population in Botswana. *Genetics* **172**, 2223-38 (2006).
6. Desjardins, C.A. *et al.* Population genomics and the evolution of virulence in the fungal pathogen *Cryptococcus neoformans*. *Genome Res* **27**, 1207-1219 (2017).
7. Litvintseva, A.P. & Mitchell, T.G. Most environmental isolates of *Cryptococcus neoformans* var. *grubii* (serotype A) are not lethal for mice. *Infect Immun* **77**, 3188-95 (2009).
8. Mukaremera, L. *et al.* The Mouse Inhalation Model of *Cryptococcus neoformans* Infection Recapitulates Strain Virulence in Humans and Shows that Closely Related Strains Can Possess Differential Virulence. *Infect Immun* **87**(2019).
9. Krysan, D.J., Zhai, B., Beattie, S.R., Misel, K.M., Wellington, M. & Lin, X. Host carbon dioxide concentration is an independent stress for *Cryptococcus neoformans* that affects virulence and antifungal susceptibility. *mBio* **10**, e01410-19 (2019).
10. Chadwick, B.J., Pham, T., Xie, X., Ristow, L.C., Krysan, D.J. & Lin, X. The RAM signaling pathway links morphology, thermotolerance, and CO_2 tolerance in the global fungal pathogen *Cryptococcus neoformans*. *eLife* **11**, e82563 (2022).
11. Ristow, L.C., Jezewski, A., Chadwick, B. J., Stamnes, M. A., Lin, X., Krysan, D. J. The fungal pathogen Cryptococcus neoformans adapts to the host environment through TOR-mediated remodeling of phospholipid asymmetry. *Preprint at https://assets.researchsquare.com/files/rs-2828872/v1_covered.pdf?c=1682464745* (2023).
12. Elshire, R.J. *et al.* A Robust, Simple Genotyping-by-Sequencing (GBS) Approach for High Diversity Species. *PLOS ONE* **6**, e19379 (2011).

13. Yadav, V., Sun, S., Coelho, M.A. & Heitman, J. Centromere scission drives chromosome shuffling and reproductive isolation. *Proceedings of the National Academy of Sciences* **117**, 7917-7928 (2020).
14. Fries, B.C., Chen, F., Currie, B.P. & Casadevall, A. Karyotype instability in *Cryptococcus neoformans* infection. *J Clin Microbiol* **34**, 1531-4 (1996).
15. Perfect, J.R., Ketabchi, N., Cox, G.M., Ingram, C.W. & Beiser, C.L. Karyotyping of Cryptococcus neoformans as an epidemiological tool. *J Clin Microbiol* **31**, 3305-9 (1993).
16. Qi, P. *et al.* UGbS-Flex, a novel bioinformatics pipeline for imputation-free SNP discovery in polyploids without a reference genome: finger millet as a case study. *BMC plant biology* **18**, 117-117 (2018).
17. Broman, K.W., Wu, H., Sen, S. & Churchill, G.A. R/qtl: QTL mapping in experimental crosses. *Bioinformatics* **19**, 889-90 (2003).
18. Roth, C., Sun, S., Billmyre, R.B., Heitman, J. & Magwene, P.M. A High-Resolution Map of Meiotic Recombination in Cryptococcus deneoformans Demonstrates Decreased Recombination in Unisexual Reproduction. *Genetics* **209**, 567-578 (2018).
19. Sun, S., Billmyre, R.B., Mieczkowski, P.A. & Heitman, J. Unisexual Reproduction Drives Meiotic Recombination and Phenotypic and Karyotypic Plasticity in Cryptococcus neoformans. *PLOS Genetics* **10**, e1004849 (2014).
20. Marra, R.E. *et al.* A genetic linkage map of Cryptococcus neoformans variety neoformans serotype D (Filobasidiella neoformans). *Genetics* **167**, 619-631 (2004).
21. Vogan, A.A., Khankhet, J., Samarasinghe, H. & Xu, J. Identification of QTLs Associated with Virulence Related Traits and Drug Resistance in Cryptococcus neoformans. *G3 (Bethesda, Md.)* **6**, 2745-2759 (2016).
22. Chun, C.D. & Madhani, H.D. Applying genetics and molecular biology to the study of the human pathogen *Cryptococcus neoformans*. *Methods Enzymol* **470**, 797-831 (2010).
23. de Gontijo, F.A., Pascon, R.C., Fernandes, L., Machado, J., Alspaugh, J.A. & Vallim, M.A. The role of the de novo pyrimidine biosynthetic pathway in *Cryptococcus neoformans* high temperature growth and virulence. *Fungal Genetics and Biology* **70**, 12-23 (2014).
24. de Montigny, J., Kern, L., Hubert, J.C. & Lacroute, F. Cloning and sequencing of URA10, a second gene encoding orotate phosphoribosyl transferase in Saccharomyces cerevisiae. *Curr Genet* **17**, 105-11 (1990).
25. Nakamura, T., Ando, A., Takagi, H. & Shima, J. EOS1, whose deletion confers sensitivity to oxidative stress, is involved in N-glycosylation in *Saccharomyces cerevisiae*. *Biochemical and Biophysical Research Communications* **353**, 293-298 (2007).
26. Gundersen, K. Growth of *Fomes annosus* under Reduced Oxygen Pressure and the Effect of Carbon Dioxide. *Nature* **190**, 649-649 (1961).
27. Römer, D., Bollazzi, M. & Roces, F. Carbon dioxide sensing in an obligate insect-fungus symbiosis: CO2 preferences of leaf-cutting ants to rear their mutualistic fungus. *PLoS One* **12**, e0174597 (2017).
28. Teskey, R.O., Saveyn, A., Steppe, K. & McGuire, M.A. Origin, fate and significance of CO2 in tree stems. *New Phytol* **177**, 17-32 (2008).
29. Burges, A. & Fenton, E. The effect of carbon dioxide on the growth of certain soil fungi. *Transactions of the British Mycological Society* **36**, 104-108 (1953).

30. Buyanovsky, G.A. & Wagner, G.H. Annual Cycles of Carbon Dioxide Level in Soil Air. *Soil Science Society of America Journal* **47**, 1139-1145 (1983).
31. Maraia, R.J., Mattijssen, S., Cruz-Gallardo, I. & Conte, M.R. The La and related RNA-binding proteins (LARPs): structures, functions, and evolving perspectives. *Wiley Interdiscip Rev RNA* **8**(2017).
32. Park, H.S. *et al.* Calcineurin Targets Involved in Stress Survival and Fungal Virulence. *PLoS Pathog* **12**, e1005873 (2016).
33. Hommel, B. *et al. Cryptococcus neoformans* resists to drastic conditions by switching to viable but non-culturable cell phenotype. *PLOS Pathogens* **15**, e1007945 (2019).
34. Sun, S., Roth, C., Floyd Averette, A., Magwene, P.M. & Heitman, J. Epistatic genetic interactions govern morphogenesis during sexual reproduction and infection in a global human fungal pathogen. *Proc Natl Acad Sci U S A* **119**(2022).
35. Roth, C. *et al.* Pleiotropy and epistasis within and between signaling pathways defines the genetic architecture of fungal virulence. *PLoS Genet* **17**, e1009313 (2021).
36. Li, D., Zhang, X., Li, Z., Yang, J., Pan, J. & Zhu, X. *Cryptococcus neoformans* Ca2+ homeostasis requires a chloride channel/antiporter Clc1 in JEC21, but not in H99. *FEMS Yeast Research* **12**, 69-77 (2012).
37. Zhu, X. & Williamson, P.R. A CLC-type chloride channel gene is required for laccase activity and virulence in *Cryptococcus neoformans*. *Molecular Microbiology* **50**, 1271-1281 (2003).
38. Charles, H.P. & Roberts, G.A. Carbon Dioxide as a Growth Factor for Mutants of *Escherichia coli*. *Microbiology* **51**, 211-224 (1968).
39. Charles, H.P. & Broadbent, J.A. Carbon Dioxide Mutants in *Neurospora*. *Nature* **201**, 1004-1006 (1964).
40. Ben-Sahra, I., Howell, J.J., Asara, J.M. & Manning, B.D. Stimulation of de novo pyrimidine synthesis by growth signaling through mTOR and S6K1. *Science* **339**, 1323-8 (2013).
41. Robitaille, A.M. *et al.* Quantitative phosphoproteomics reveal mTORC1 activates de novo pyrimidine synthesis. *Science* **339**, 1320-3 (2013).
42. Nielsen, K., Cox, G.M., Wang, P., Toffaletti, D.L., Perfect, J.R. & Heitman, J. Sexual cycle of *Cryptococcus neoformans* var. *grubii* and virulence of congenic a and alpha isolates. *Infect Immun* **71**, 4831-41 (2003).
43. Chadwick, B.J. & Lin, X. On the History and Applications of Congenic Strains in *Cryptococcus* Research. *Pathogens* **9**(2020).
44. Lin, X. *et al.* alpha AD alpha hybrids of *Cryptococcus neoformans*: evidence of same-sex mating in nature and hybrid fitness. *PLoS Genet* **3**, 1975-90 (2007).
45. Koren, S., Walenz, B.P., Berlin, K., Miller, J.R., Bergman, N.H. & Phillippy, A.M. Canu: scalable and accurate long-read assembly via adaptive k-mer weighting and repeat separation. *Genome Res* **27**, 722-736 (2017).
46. Li, H. Minimap2: pairwise alignment for nucleotide sequences. *Bioinformatics* **34**, 3094-3100 (2018).
47. Vaser, R., Sović, I., Nagarajan, N. & Šikić, M. Fast and accurate de novo genome assembly from long uncorrected reads. *Genome Res* **27**, 737-746 (2017).
48. Li, H. Aligning sequence reads, clone sequences and assembly contigs with BWA-MEM. (2013).

49. Li, H. *et al.* The Sequence Alignment/Map format and SAMtools. *Bioinformatics (Oxford, England)* **25**, 2078-2079 (2009).
50. Walker, B.J. *et al.* Pilon: An Integrated Tool for Comprehensive Microbial Variant Detection and Genome Assembly Improvement. *PLOS ONE* **9**, e112963 (2014).
51. Krueger, F. Trim Galore! (2021).
52. McKenna, A. *et al.* The Genome Analysis Toolkit: a MapReduce framework for analyzing next-generation DNA sequencing data. *Genome Res* **20**, 1297-303 (2010).
53. Yin, L. *et al.* rMVP: A Memory-efficient, Visualization-enhanced, and Parallel-accelerated Tool for Genome-wide Association Study. *Genomics, Proteomics & Bioinformatics* **19**, 619-628 (2021).
54. Li, Y., Pham, T., Xie, X. & Lin, X. Identification and Characterization of an Intergenic Safe Haven Region in Human Fungal Pathogen *Cryptococcus gattii*. in *Journal of Fungi* Vol. 8 (2022).
55. Sun, S., Billmyre, R.B., Mieczkowski, P.A. & Heitman, J. Unisexual reproduction drives meiotic recombination and phenotypic and karyotypic plasticity in *Cryptococcus neoformans*. *PLoS Genet* **10**, e1004849 (2014).
56. Perfect, J.R., Magee, B.B. & Magee, P.T. Separation of chromosomes of *Cryptococcus neoformans* by pulsed field gel electrophoresis. *Infection and Immunity* **57**, 2624-2627 (1989).
57. Lin, J., Fan, Y. & Lin, X. Transformation of *Cryptococcus neoformans* by electroporation using a transient CRISPR-Cas9 expression (TRACE) system. *Fungal genetics and biology : FG & B* **138**, 103364-103364 (2020).
58. Fan, Y. & Lin, X. Multiple Applications of a Transient CRISPR-Cas9 Coupled with Electroporation (TRACE) System in the *Cryptococcus neoformans* Species Complex. *Genetics* **208**, 1357-1372 (2018).
59. Basenko, E.Y. *et al.* FungiDB: An Integrated Bioinformatic Resource for Fungi and Oomycetes. *J Fungi (Basel)* **4**(2018).
60. Lin, J. *et al.* Immunoprotection against Cryptococcosis Offered by Znf2 Depends on Capsule and the Hyphal Morphology. *mBio* **0**, e02785-21 (2022).
61. Zhao, Y., Wang, Y., Upadhyay, S., Xue, C. & Lin, X. Activation of Meiotic Genes Mediates Ploidy Reduction during Cryptococcal Infection. *Curr Biol* **30**, 1387-1396 e5 (2020).
62. Zhai, B., Zhu, P., Foyle, D., Upadhyay, S., Idnurm, A. & Lin, X. Congenic strains of the filamentous form of *Cryptococcus neoformans* for studies of fungal morphogenesis and virulence. *Infect Immun* **81**, 2626-37 (2013).
63. Zhu, P., Zhai, B., Lin, X. & Idnurm, A. Congenic strains for genetic analysis of virulence traits in *Cryptococcus gattii*. *Infect Immun* **81**, 2616-25 (2013).
64. Zhai, B., Wu, C., Wang, L., Sachs, M.S. & Lin, X. The antidepressant sertraline provides a promising therapeutic option for neurotropic cryptococcal infections. *Antimicrob Agents Chemother* **56**, 3758-66 (2012).
65. Soderlund, C., Nelson, W., Shoemaker, A. & Paterson, A. SyMAP: A system for discovering and viewing syntenic regions of FPC maps. *Genome Res* **16**, 1159-68 (2006).
66. Wang, P., Cutler, J., King, J. & Palmer, D. Mutation of the regulator of G protein signaling Crg1 increases virulence in *Cryptococcus neoformans*. *Eukaryot Cell* **3**, 1028-35 (2004).

67. Altamirano, S. *et al.* The Cyclin Cln1 Controls Polyploid Titan Cell Formation following a Stress-Induced G(2) Arrest in *Cryptococcus*. *mBio* **12**, e0250921 (2021).
68. Idnurm, A., Reedy, J.L., Nussbaum, J.C. & Heitman, J. *Cryptococcus neoformans* virulence gene discovery through insertional mutagenesis. *Eukaryot Cell* **3**, 420-9 (2004).
69. Day, J.N. *et al.* Comparative genomics of *Cryptococcus neoformans* var. grubii associated with meningitis in HIV infected and uninfected patients in Vietnam. *PLoS Negl Trop Dis* **11**, e0005628 (2017).
70. Wang, P., Cardenas, M.E., Cox, G.M., Perfect, J.R. & Heitman, J. Two cyclophilin A homologs with shared and distinct functions important for growth and virulence of *Cryptococcus neoformans*. *EMBO Rep* **2**, 511-8 (2001).

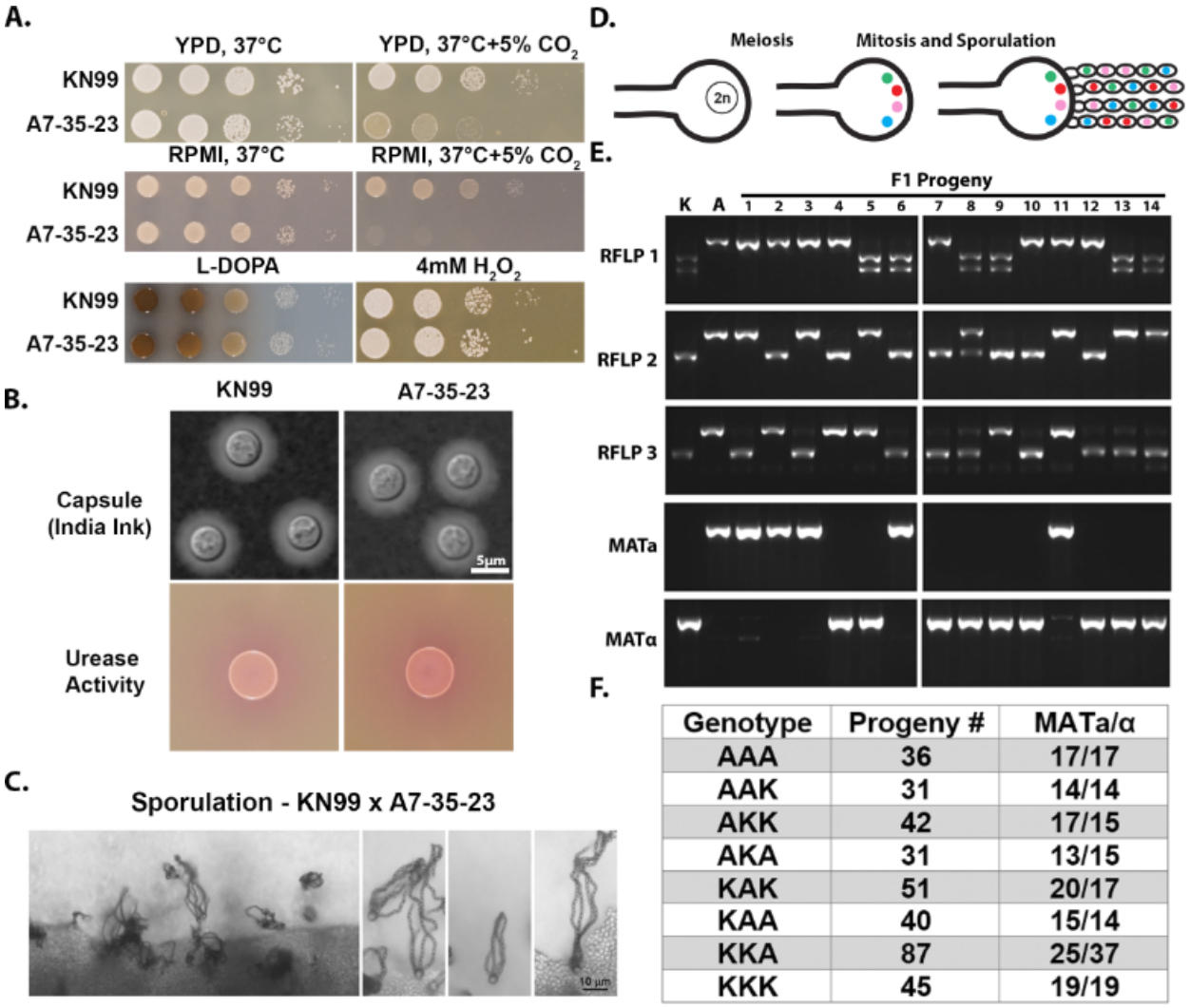

Genotype	Progeny #	MATa/α
AAA	36	17/17
AAK	31	14/14
AKK	42	17/15
AKA	31	13/15
KAK	51	20/17
KAA	40	15/14
KKA	87	25/37
KKK	45	19/19

Figure 5.1. Generating a QTL mapping population. (A) KN99 and A7-35-23 cells were serially diluted and spotted onto the indicated media. YPD is a nutrient rich mycological

medium. RPMI buffered to pH 7.0 was used to mimic host physiological conditions. The appearance of dark brown pigmentation on L-DOPA medium was used to assay melanization. 4mM H_2O_2 was used to test oxidative stress resistance. (B) Cells grown in the RPMI media were stained with India ink to reveal capsule, which excludes the ink particles and appears as a halo surrounding the yeast cell. Christensen Urea Agar was used to test urease activity. Media coloration change from yellow to pink reflects alkalinization due to urease activity. (C) Spore chains produced by the cross between KN99 and A7-35-23 after co-incubation on V8 juice agar medium in the dark at 22˚C for 2 weeks. (D) Diagram of *C. neoformans* meiosis and sporulation. Four distinct genotypes are produced from meiosis, 2 *MAT*a and 2 *MAT*α, followed by mitosis and sporulation. (E) Images of DNA gel electrophoresis showing the RFLP and mating type markers of a few selected progeny. (F) The frequency of each RFLP and mating type genotype observed in the collected F1 progeny.

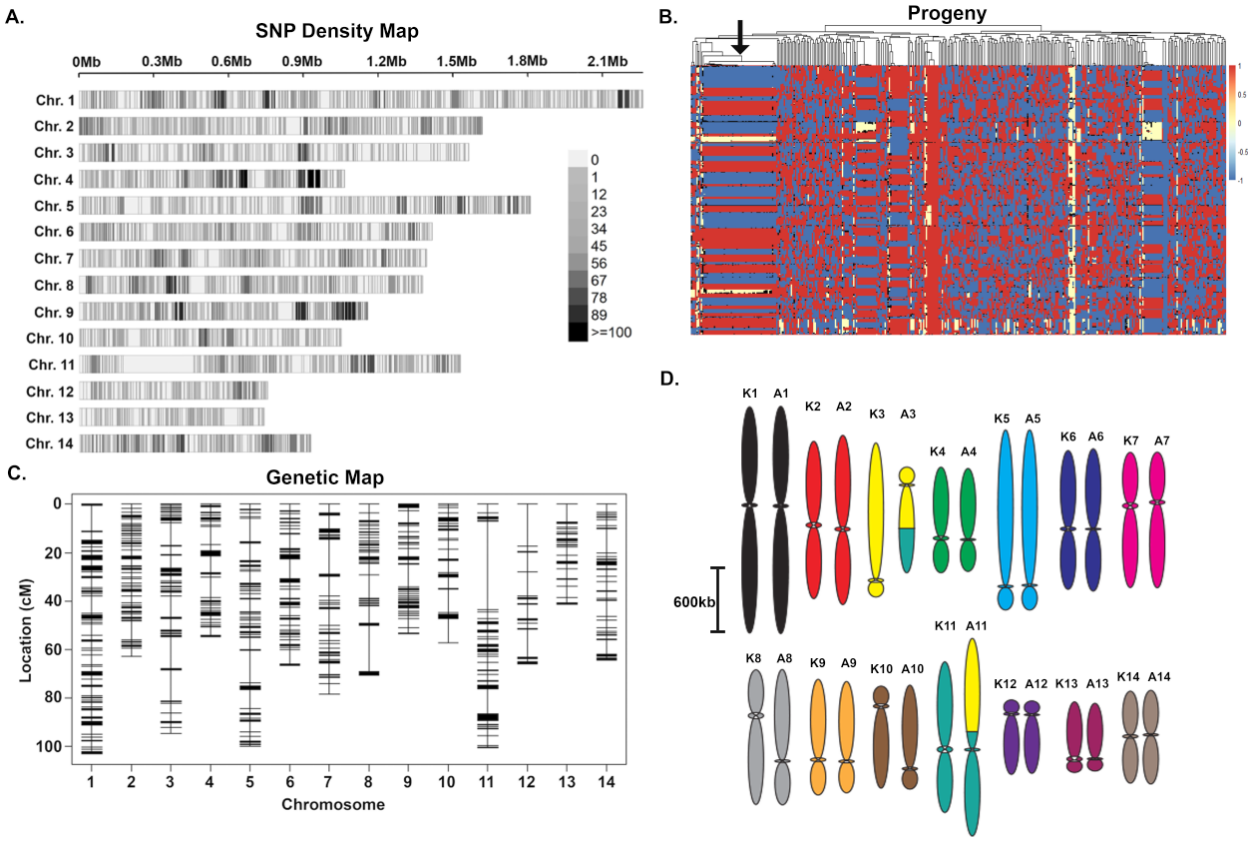

Figure 5.2. Linkage mapping with SNP markers. (A) SNP density plot showing frequency of SNP markers throughout the genome, based on sequences of the F1 progeny. The gradient scale represents the number of SNPs in a 500bp window. (B) Heatmap showing recombination of parental DNA in progeny. Progeny are clustered together based on sequence similarity. Red indicates DNA inherited from KN99, blue indicates DNA inherited from A7-35-23, and black indicates missing sequence information. (C) Genetic map showing location of SNP markers based on their recombination frequency in the F1 progeny. (D) Synteny (same color) between chromosomes of the two parents. “K” for KN99 and “A” for A7-35-23.

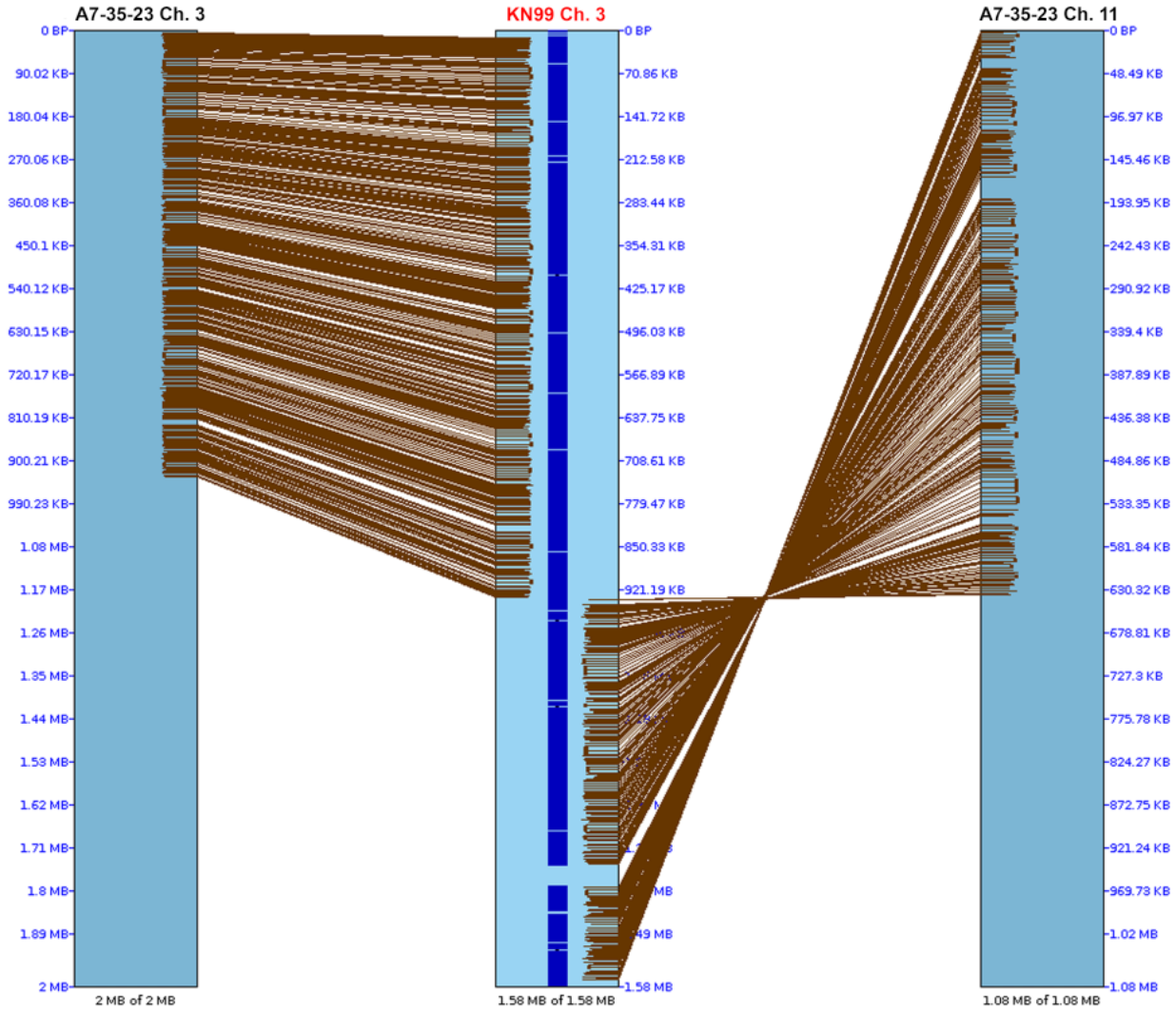

Figure S5.1. Synteny analysis of KN99 chromosome 3. Symap[65] chromosome maps depicting syntenic sequences between chromosome 3 of KN99 and chromosomes 3 and 11 of A7-35-23.

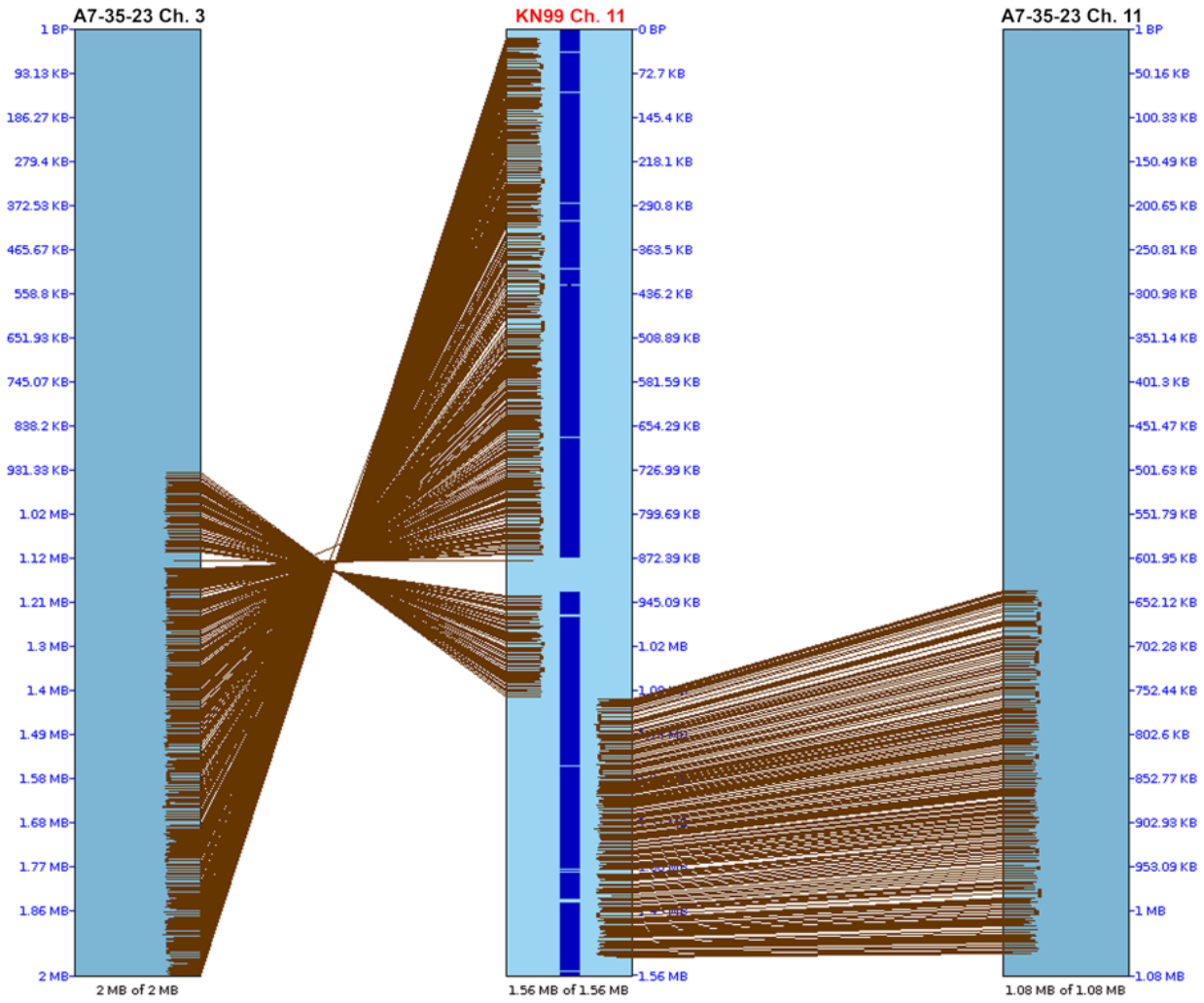

Figure S5.2. Synteny analysis of KN99 chromosome 11. Symap[65] chromosome maps depicting syntenic sequences between chromosome 11 of KN99 and chromosomes 3 and 11 of A7-35-23.

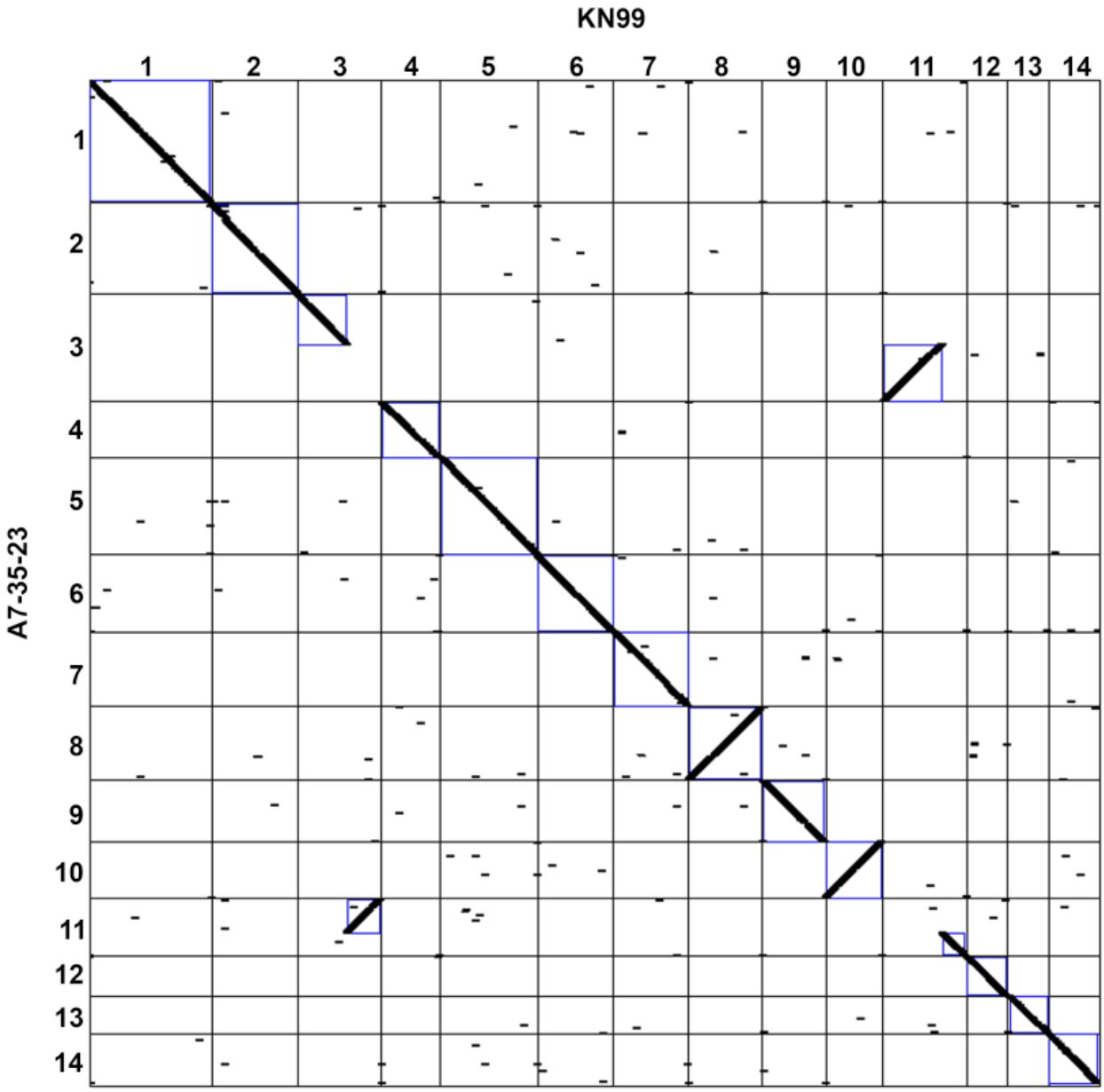

Figure S5.3. Whole genome comparison between KN99 and A7-35-23. Symap [65] dotplot showing chromosome synteny between KN99 and A7-35-23. Dots are plotted when synteny block sequence homology is over 80% similar.

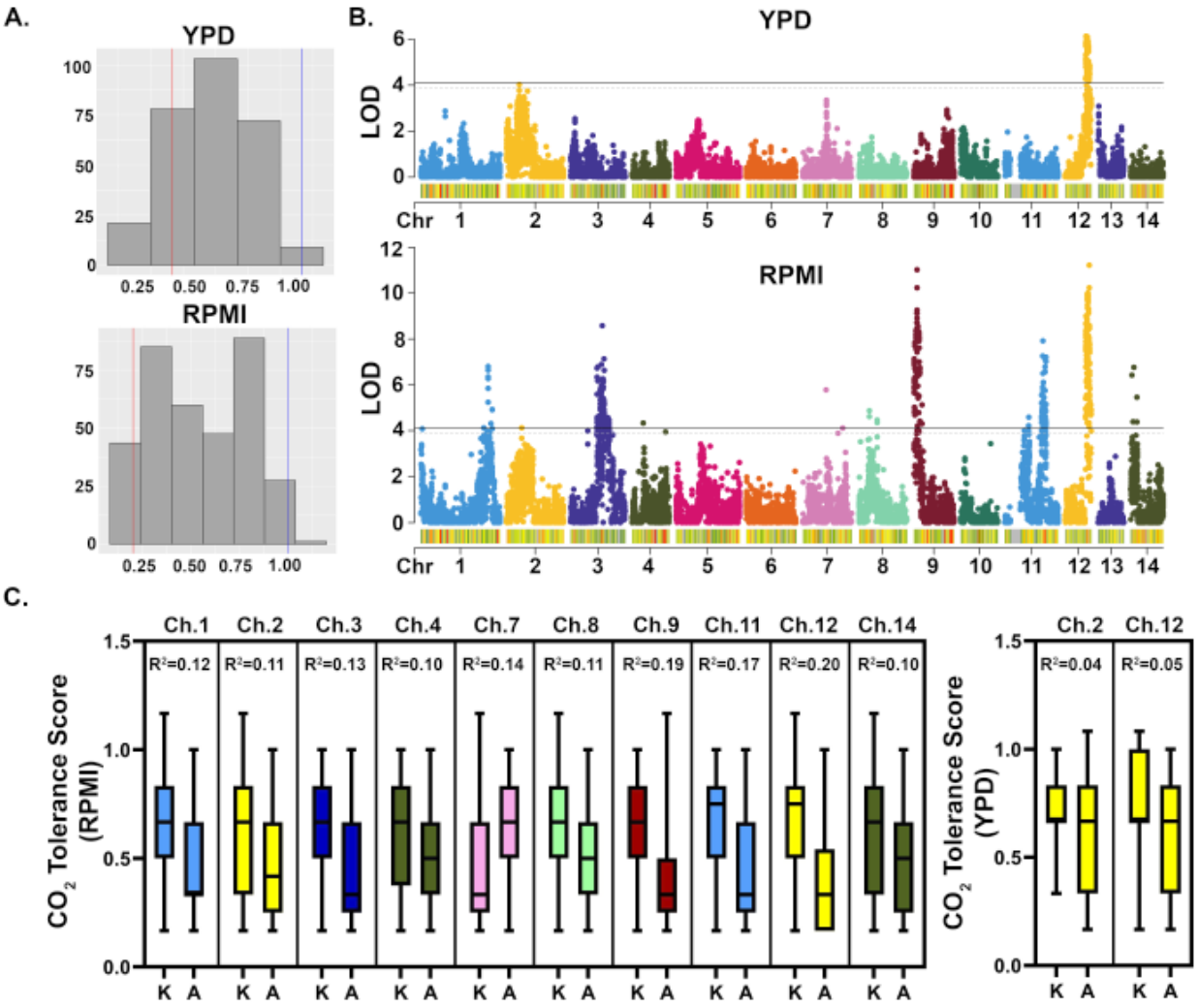

Figure 5.3. QTL mapping analysis. (A) Distributions of CO_2 tolerance scores on YPD or RPMI among the F1 progeny. Red line: the score for A7-35-23, Blue line: the score for KN99. (B) Manhattan plots indicate the LOD score of each SNP marker across the genome. The dashed LOD threshold line indicates $p = 0.05$ and solid line indicates $p = 0.01$. SNP density for each chromosome is depicted by the yellow-green-red (low-medium-high) color across the x-axis. (C) Box plots showing the CO_2 tolerance score distribution at the most significant peak/allele on the indicated chromosome. The R^2 value indicates the variation in CO_2 tolerance the allele explains.

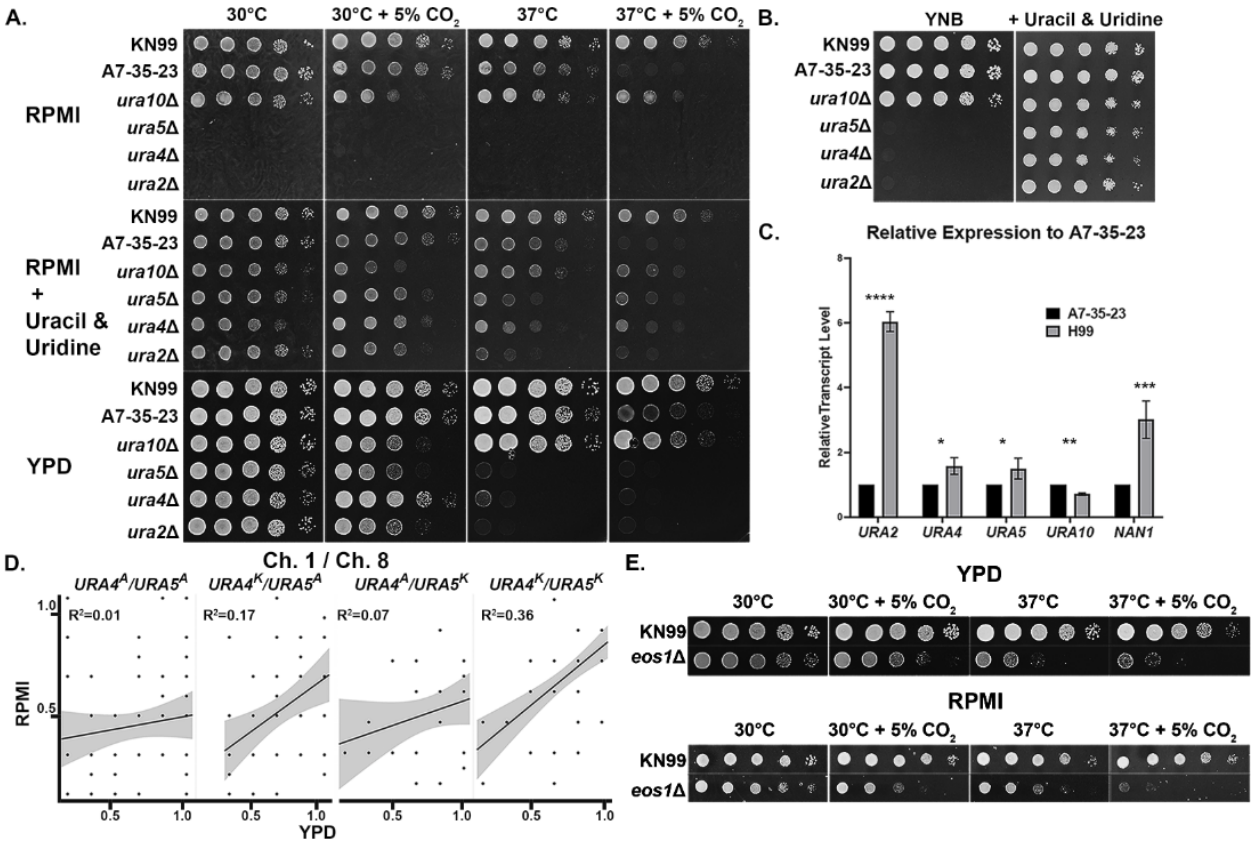

Figure 5.4. Validating the roles of QTL analysis candidate genes in CO_2 tolerance. (A) Growth of the indicated strains on RPMI, RPMI supplemented with 40µM Uracil and 40µM Uridine, or YPD media. (B) The same was done using the minimal YNB media or YNB supplemented with 40µM Uracil and 40µM Uridine. (C) Relative transcript levels in RPMI + 5% CO_2 of the indicated genes were calculated using FPKM values taken from our previously generated RNA sequencing data [11]. Error bars indicate standard deviation and asterisks indicate statistical significance (*P <0.05, **P<0.01, ***P<0.0001, ****P<0.00001). (D) Correlation of growth scores on RPMI vs YPD of progeny with the indicated genotypes for the chromosomes 1 and 8 significant QTL regions. (E) Growth of KN99 and the *CNAG_05706* knockout mutant (*eos1*Δ) cells under the indicated conditions.

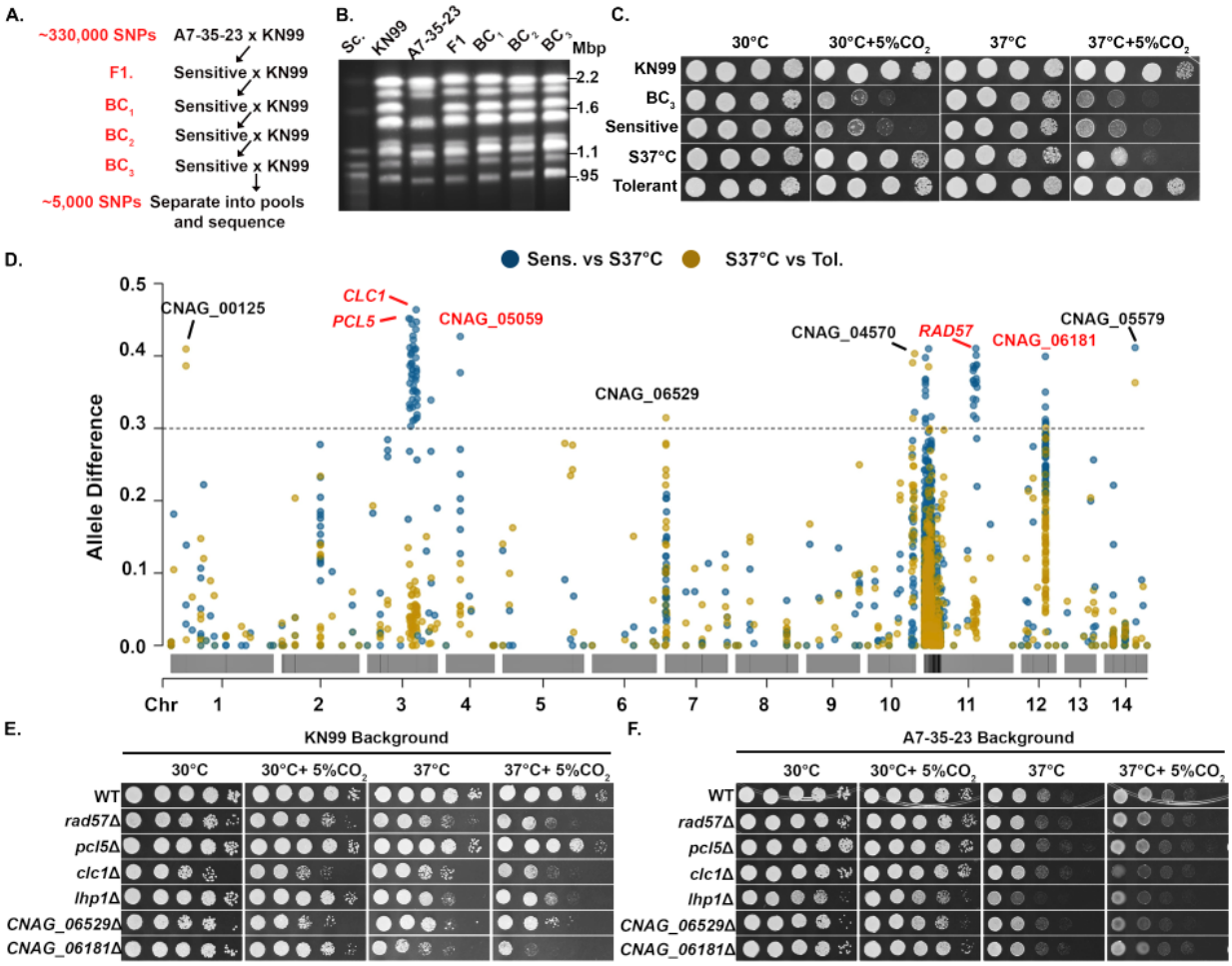

Figure 5.5. Bulk segregant analysis for finer mapping of QTLs. (A) A diagram depicting the backcrossing strategy to generate near-congenic or near-isogenic progeny for bulk segregant analysis. (B) CHEF analysis of karyotypes of parental strains used in the backcrossing strategy. (C) Growth of the two parents (KN99 and BC_3) of the last backcross and representatives of each bulk on YPD media by spotting assay. (D) Allele differences between the indicated groups (yellow or blue) were plotted against position of the SNP in the genome. The chromosomes are drawn in grey along the x-axis, with SNPs marked in black to show SNP density. (E) Serial dilution spotting assays on YPD media of WT and QTG knockouts in both KN99 and the A7-35-23 background.

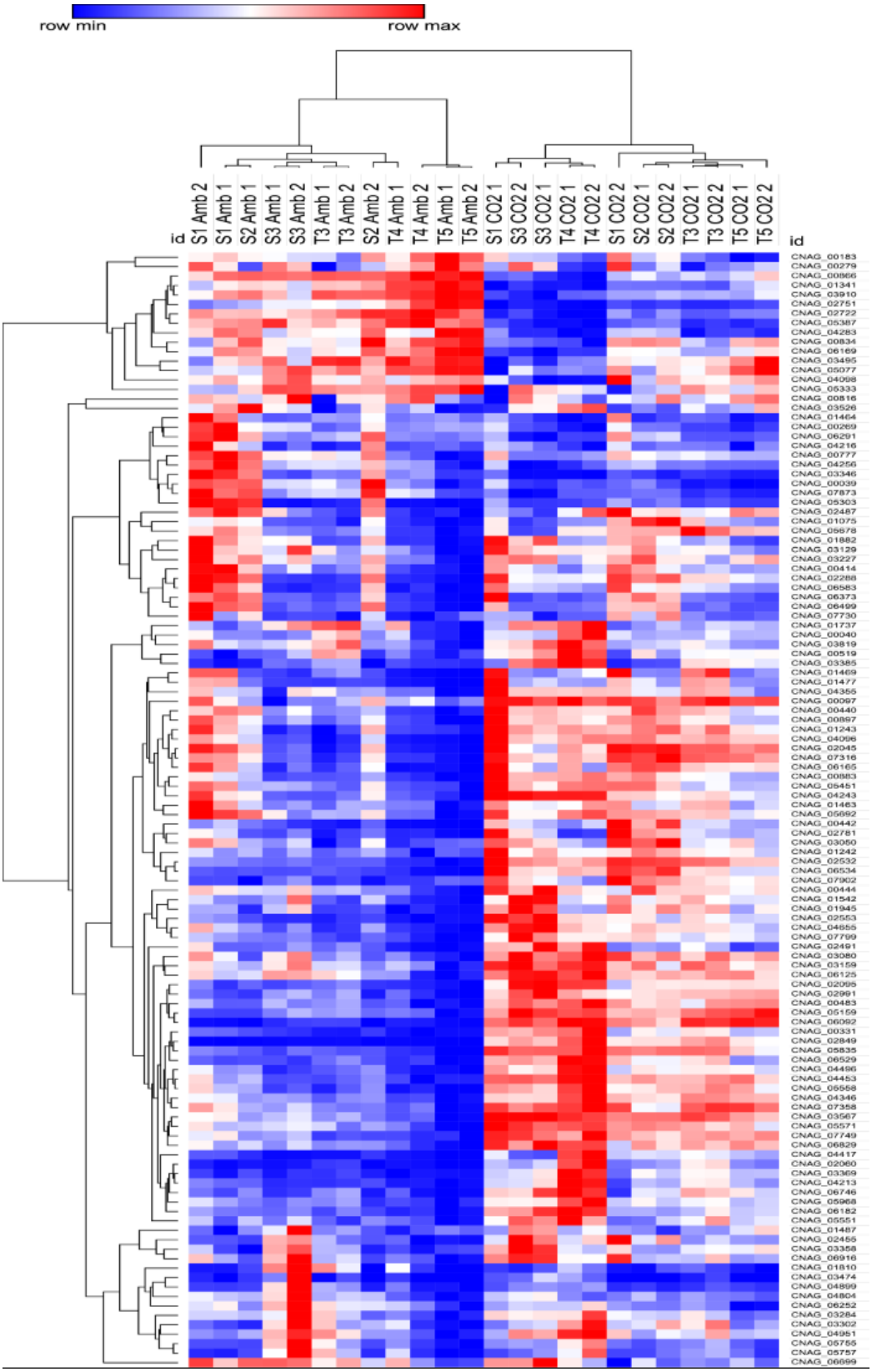
row min
row max
id
S1 Amb 2
S1 Amb 1
S2 Amb 1
S3 Amb 1
S3 Amb 2
T3 Amb 1
T3 Amb 2
S2 Amb 2
T4 Amb 1
T4 Amb 2
T5 Amb 1
T5 Amb 2
S1 CO2 1
S3 CO2 2
S3 CO2 1
T4 CO2 1
T4 CO2 2
S1 CO2 2
S2 CO2 1
S2 CO2 2
T3 CO2 1
T3 CO2 2
T5 CO2 1
T5 CO2 2
id

Figure S5.4. The transcriptome of the selected genes does not differentiate CO_2-sensitive from CO_2-tolerant BC_4 progeny. Heatmap showing normalized total RNA counts of NanoString targets in 3 CO_2-sensitive (S1, S2, S3) and 3 CO_2-tolerant (T3, T4, T5) BC_4 progeny, cultured at either ambient or 5% CO_2. Red indicates higher and blue indicates lower transcript abundance.

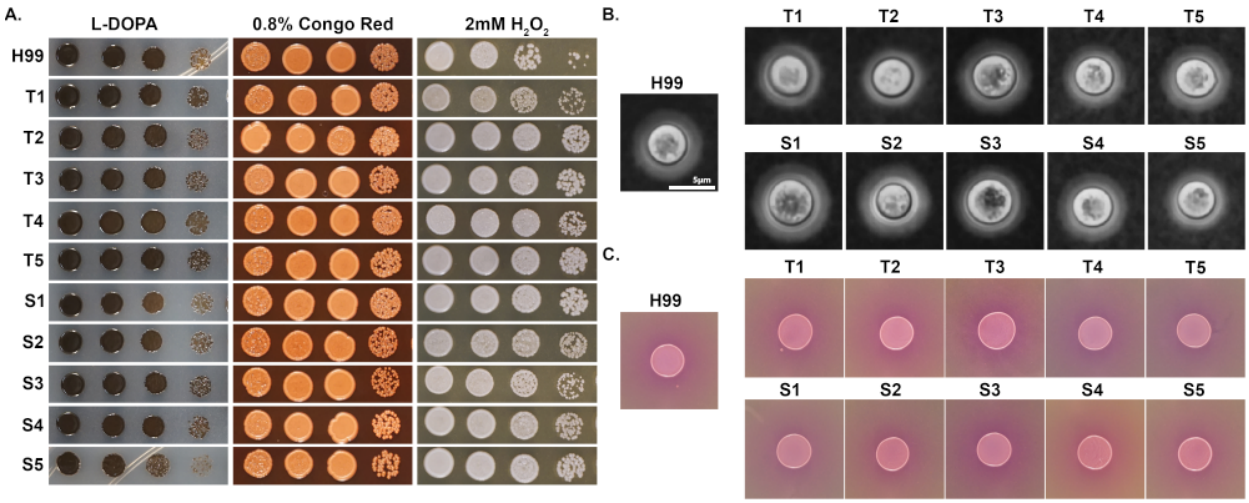

Figure S5.5. *In vitro* phenotypes of backcross progeny differ significantly only in CO_2 tolerance (A) The indicated strains were grown overnight in YPD media, serially diluted, spotted onto the indicated media, and incubated under the indicated condition at 30˚C for two days. L-DOPA medium was used to assess melanin synthesis, YPD + 0.8% Congo Red was used to test cell wall stress tolerance, YPD + 4mM H_2O_2 was used to test oxidative stress tolerance. (B) Cells grown in RPMI 37˚C + 5% CO_2 were observed under microscope with India Ink staining to observe capsule. (C) The same cells were also spotted onto Christensen Urea Agar to test for urease activity, indicated by a change in medium coloration from yellow to pink.

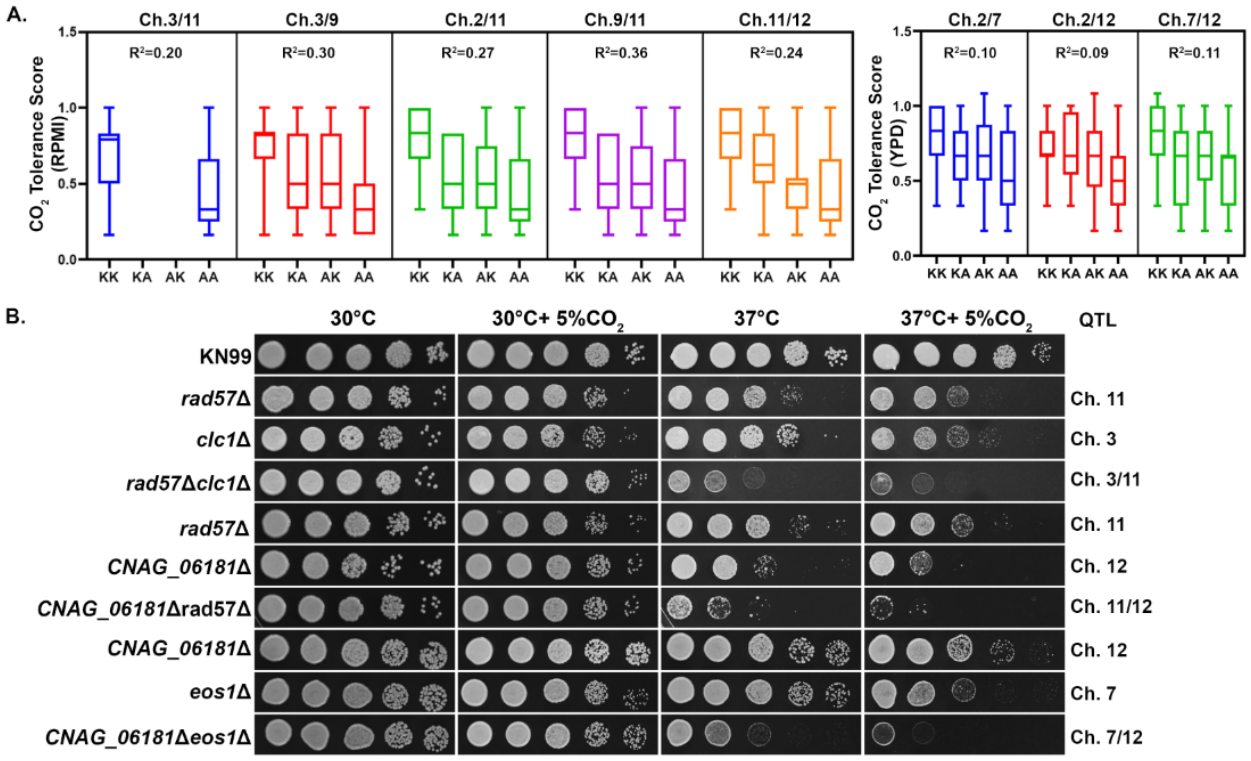

Figure 5.6. Interaction between multiple genetic loci contributes to CO_2 tolerance. (A) Box plots showing the relationship between CO_2 tolerance score and combination of significant alleles from the QTL analysis to observe pairwise interactions. "K" denotes the KN99a allele and "A" denotes the A7-35-23 allele. The R^2 value indicates the variation in CO_2 tolerance the allele combinations explain. (B) Serial dilution spotting assays on YPD of the WT KN99 and mutants to observe interactions between QTGs.

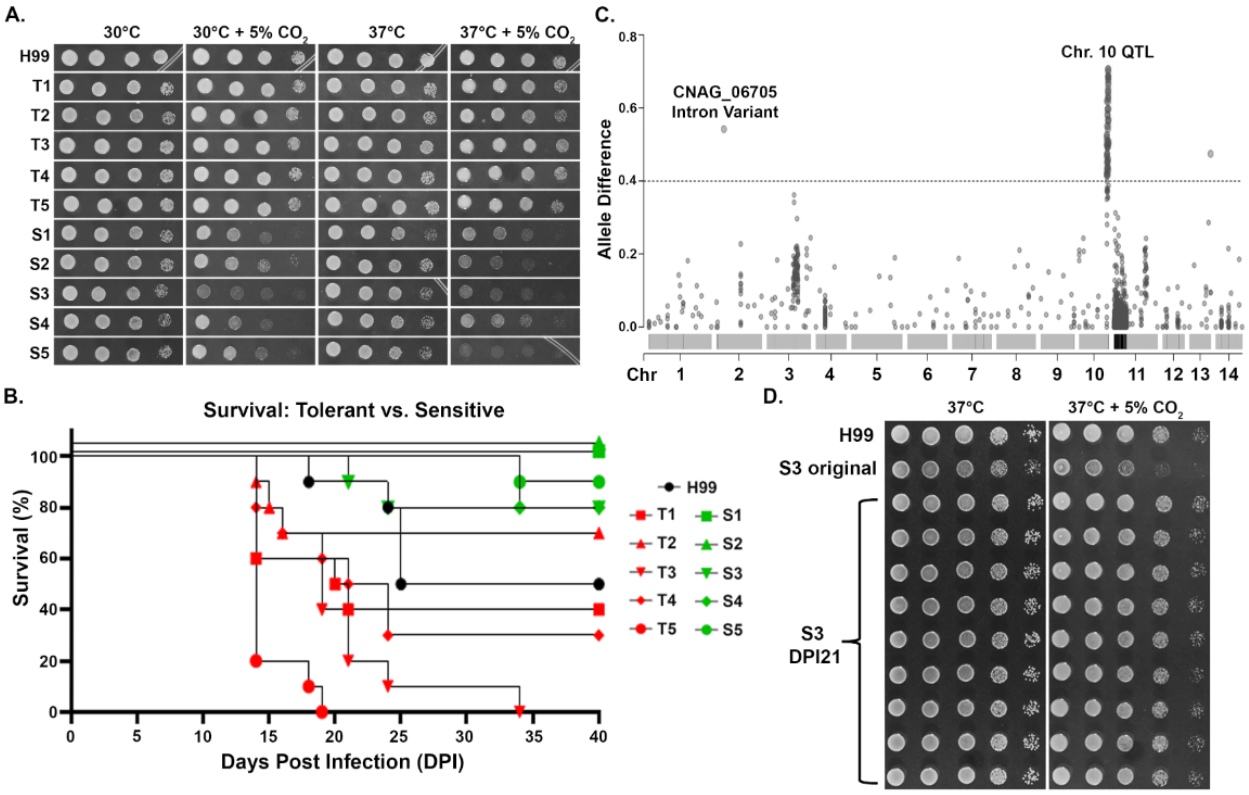

Figure 5.7. CO_2 tolerance in the backcross progeny is a crucial virulence factor (A) Growth of the 10 BC_4 progeny (5 CO_2-sensitive and 5 CO_2-tolerant) and control parental strain KN99 used for the murine model experiment on RPMI medium under the indicated conditions. (B) Survival of outbred CD-1 mice infected with 1 x 10^5 cells of each indicated strain in the panel above (10 mice/strain). (C) Allele differences using SNP markers between the evolved isolates in pool sequencing and original S3 strain. (D) Growth of isolates from a mouse which succumbed to infection by the original CO_2-sensitive strain S3 at DPI 21, and the controls KN99 and original S3 strain.

Table 5.1: RPMI CO_2 tolerance QTL analysis summary

Chr.	LOD 1.5 Interval	Range (bp)	Position of Marker at Peak	LOD at Peak
1	1,907,440 – 1,926,718	19,278	1,919,611	6.8
2	424,895 – 427,260	2,365	425,204	4.1
3	784,263 – 989,875	202,612	910,746	8.6

4	325,843 – 336,186	10,343	325,984	4.3
7	664,647 – 667,652	3,005	664,710	5.8
8	314,486 – 319,934	5,448	315,363	4.9
9	68,240 – 166,158	97,918	103,036	11.1
11	1,094,300 – 1,184,407	90,107	1,095,693	7.9
12	593,304 – 716,620	123,316	695,843	11.2
14	96,371 – 181,571	85,200	98,342	6.77

Table 5.2: YPD CO_2 tolerance QTL analysis summary

Chr.	LOD 1.5 Interval	Range (kb)	Position of Marker at Peak	LOD at Peak
2	95,684 – 605,875	510,191	359,219	4.0
12	596,775 – 716,620	119,845	609,555	6.1

Table 5.3. Results of BSA

Chr.	Gene	Allele Difference	Group Comparison	LOD Score	KN99 Allele Effect	Note on Variant
1	CNAG_00125 (*CRG1*)[42,66]	0.39	S37˚C vs Tol.	n/a	-	Missense
3	CNAG_02658 (*PCL5*)[67]	0.45	Sens. vs S37˚C	8.6	+	5’ UTR Indel
3	CNAG_02702 (*CLC1*)[37,68]	0.46	Sens. vs S37˚C	8.6	+	Intron Variant
4	CNAG_05059 (*PDB1*)	0.42	Sens. vs S37˚C	4.3	-	3’ UTR Indel
7	CNAG_06529	0.31	S37˚C vs Tol.	n/a	+	5’ UTR Indel
10	CNAG_04570 *(LHP1)*[32]	0.39	S37˚C vs Tol.	n/a	+	3’ UTR Indel
11	CNAG_01891 (*RAD57*)[69]	0.40	Sens. vs S37˚C	7.1	+	3’ UTR Indel
12	CNAG_06181	0.52	Sens. vs S37˚C	9.0	+	Missense and 5’ UTR
14	CNAG_05579	0.41	Sens. vs S37˚C	n/a	-	Intron Variant

Table 5.4 – Strains Used

C. neoformans strain Identifier	Strain Background	Genotype	Reference	Additional information
KN99α	H99	MATα	[42]	Isogenic to H99
KN99**a**	H99	MAT**a**	[42]	Parental strain used for QTL Mapping and BSA
A7-35-23	A7-35-23	MATα	[7]	Parental strain used for QTL Mapping
*ura2*Δ	H99	MATα, CNAG_07373::NAT	[22]	FGSC deletion set Plate 17 Well A6
*ura4*Δ	H99	MATα, CNAG_00734::NAT	[22]	FGSC deletion set Plate 21 Well G5
*ura5*Δ	H99	MATα, *ura5*$^{-}$	[70]	F99, previously obtained on 5-FOA medium
*ura10*Δ	H99	MATα, CNAG_04961::NAT	[22]	FGSC deletion set Plate 32 Well G1
*eos1*Δ	H99	MATα, CNAG_05706::NAT	[22]	FGSC deletion set Plate 47 Well E2
*rad57*Δ	H99	MATα, CNAG_01891::NAT	[22]	FGSC deletion set Plate 16 Well A8
*CNAG_01891*Δ	A7-35-23	MATα, CNAG_01891::G418	Here	Strain number BC1508
*pcl5*Δ	H99	MATα, CNAG_02658::NAT	[22]	FGSC deletion set Plate 6 Well E7
*pcl5*Δ	A7-35-23	MATα, CNAG_02658::G418	Here	Strain number BC1496
*clc1*Δ	H99	MATα, CNAG_02702::NAT	[22]	FGSC deletion set

				Plate 12 Well E1
*clc1*Δ	A7-35-23	MATα, CNAG_02702::G418	Here	Strain number BC1498
*lhp1*Δ	H99	MATα, CNAG_04570::NAT	Here	Strain number BC1409
*lhp1*Δ	A7-35-23	MATα, CNAG_04570::G418	Here	Strain number BC1500
*CNAG_06181*Δ	H99	MATα, CNAG_06181::NAT	[22]	FGSC deletion set Plate 48 Well A1
*CNAG_06181*Δ	A7-35-23	MATα, CNAG_06181::G418	Here	Strain number BC1520
*CNAG_06529*Δ	H99	MATα, CNAG_06529::NAT	Here	Strain number BC1411
*CNAG_06529*Δ	A7-35-23	MATα, CNAG_06529::G418	Here	Strain number BC1504
*eos1*Δ	H99	MATα, CNAG_05706::NAT	[22]	FGSC deletion set Plate 47 Well E2
*rad57*Δ*clc1*Δ	H99	MATα, CNAG_01891::NAT, CNAG_02702::G418	Here	Strain number BC1799
*CNAG_06181*Δ*rad57*Δ	H99	MATα, CNAG_06181::NAT, CNAG_01891::G418	Here	Strain number BC1781
*CNAG_06181*Δeos1Δ	H99	MATα, CNAG_06181::NAT, CNAG_05706::G418	Here	Strain number BC1775

Table 5.5 – Primers Used

Primer Identifier	Sequence (5’ -> 3’)	Purpose
Linlab5643/BC	aaccaagatgatgtacgatgag	RFLP primer pair 1
Linlab5644/BC	aacgatgtcatacttcttgtcc	RFLP primer pair 1
Linlab5647/BC	cttgaaatcgcctagcataaac	RFLP primer pair 2
Linlab5648/BC	agagtcgatttgtaggttcttc	RFLP primer pair 2
Linlab5651/BC	cgtccatacatactcatcatcc	RFLP primer pair 3
Linlab5652/BC	actatgaacgagatcccatttg	RFLP primer pair 3
JOHE15629	agctgatgctgtggattgaatac	*SXI2**a*** MAta specific primer

JOHE15630	tgcaatcacagcaccttacatag	*SXI2**a*** MATa specific primer
JOHE7270	atcagagacagaggagcaagac	*STE20* MATα specific primer
JOHE7271	ctaactctactacacctcacgg	*STE20* MATα specific primer
Linlab4627/YF	ggctcaaagagcagatcaatg	gRNA-FF
Linlab4628/YF	cctctgacacatgcagctcc	gRNA-FR
Linlab4594/YF	ccatcgatttgcattagaactaaaaacaaagca	gRNA-F
Linlab4595/YF	ccgctcgagtaaaacaaaaaagcaccgac	gRNA-R
Linlab9238/BC	ctctcacacgctccttgaccaacagtataccctgccggtg	gRNA complementary CNAG_01891 – U6R
Linlab9239/BC	ggtcaaggagcgtgtgagaggttttagagctagaaatagcaagtt	gRNA CNAG_01891-ScaffoldF
Linlab9240/BC	ataggccggccatgtcatttgcctctttcccc	CNAG_01891 ORF F
Linlab9242/BC	cgcactatgataaccgtcca	CNAG_01891 ORF R
Linlab9106/BC	actttcccccatttcgccttaacagtataccctgccggtg	gRNA complementary CNAG_02658 – U6R
Linlab9107/BC	aaggcgaaatgggggaaagtgttttagagctagaaatagcaagtt	gRNA CNAG_02658-ScaffoldF
Linlab8226/BC	ataggccggcccctctttacctcctggtgca	CNAG_02658 ORF F
Linlab9117/BC	ggaccatcagttgcgaaatg	CNAG_02658 ORF R
Linlab9108/BC	agttcttccattcggcacacaacagtataccctgccggtg	gRNA complementary CNAG_02702 – U6R
Linlab9109/BC	gtgtgccgaatggaagaactgttttagagctagaaatagcaagtt	gRNA CNAG_02702-ScaffoldF
Linlab8938/BC	gatctccacagaaaacttcaaaggccggcctctatacccagcgagctacg	CNAG_02702 ORF F
Linlab9118/BC	ggtttcagatgagctggaagc	CNAG_02702 ORF R
Linlab8651/BC	atagcctccaaccctggtccaacagtataccctgccggtg	gRNA complementary

		CNAG_04570 – U6R
Linlab8652/BC	ggaccagggttggaggctatgttttagagctagaaatagcaagtt	gRNA CNAG_04570-ScaffoldF
Linlab7699/BC	attagcgatcgcctgctcatagttctctgactcctc	CNAG_04570 ORF F
Linlab7700/BC	ataggccggccatgtcgccgtctcaacaac	CNAG_04570 ORF R
Linlab8916/BC	gaaactgagggcactgctctaacagtataccctgccggtg	gRNA complementary CNAG_06181 – U6R
Linlab8917/BC	agagcagtgccctcagtttcgttttagagctagaaatagcaagtt	gRNA complementary CNAG_06181 – U6R
Linlab8184/BC	ataggccggcccgacatacacgctgcaataat	CNAG_06181 ORF F
Linlab8185/BC	ccttaattaaggatcacttcgctgtccatctg	CNAG_06181 ORF R
Linlab8655/BC	ccgtaacgcgaaagacgctcaacagtataccctgccggtg	gRNA complementary CNAG_06529 – U6R
Linlab8656/BC	gagcgtctttcgcgttacgggttttagagctagaaatagcaagtt	gRNA complementary CNAG_06529 – U6R
Linlab8180/BC	ccgtaacgcgaaagacgctcaacagtataccctgccggtg	CNAG_06529 ORF F
Linlab8181/BC	gagcgtctttcgcgttacgggttttagagctagaaatagcaagtt	CNAG_06529 ORF R

CHAPTER 6

CONCLUSIONS ON CO_2 TOLERANCE IN FUNGI AND CRYPTOCOCCUS NEOFORMANS

All organisms have a threshold for CO_2 they can tolerate before the concentration becomes lethal. In the kingdom fungi, there is an amazing variation in CO_2 tolerance among different organisms and even species. This variation in CO_2 tolerance is likely associated with the level of CO_2 fungi experience in their natural niches. Burgest et al., found that fungi isolated from the upper 5cm of soil were less tolerant to CO_2 compared with fungi isolated from soil >10cm deep [1]. For example, while a species of *penicillium* isolated from upper part of soil was greatly inhibited by 5% CO2, a species of *Zygorrhynchu* from deeper soil was able to maintain growth even at 20% CO_2. Analysis of the soil where these fungi were isolated found that CO_2 levels taken from deeper parts of soil sometimes ranged from 3.5-9.2%, while the upper part was closer to ambient levels. Interestingly, some fungi have been found to be extremely tolerant to high levels of CO_2. In one study, three species of *Pleurotus* (a common edible mushroom) were observed to have a positive growth effect in response to high CO_2, with the optimum concentration being between 16% and 22% [2]. Growth of these species was not inhibited until CO_2 levels reached 36%. The authors noted that enhanced growth in high CO_2 of *Pleurotus* was beneficial for farming, as there was not much worry for having to sterilize their media to obtain pure cultures. However, this ability to grow in high CO_2 is found in other fungi as well. *Fusarium sporotrichosis*, which produces the highly toxic mycotoxin T-2 in corn, was cultured on corn kernels in varying levels of CO_2 to test if growth and toxin production could be inhibited

[3]. The researchers found that mycotoxin production was abolished under 60% CO_2, but trace amounts were found under 40% CO_2. Furthermore, they noted that fungal growth rate was similar in the high CO_2 conditions compared with in normal air, indicating that the mycotoxin production was not correlated with growth rate here. With such high tolerance to CO_2, *F. sporotrichosis* would be an interesting model for comparative studies with low CO_2-tolerant fungi.

For fungal pathogens, the ability to tolerate host CO_2 levels is critical for survival. While the fungal pathogen *C. albicans* is a human gut commensal and already adapted for growth at host CO_2 levels, environmental fungi like *Cryptococcus neoformans* need to have some mechanism for adaptation to different CO_2 levels. Before I started my dissertation research, it was observed that many environmental isolates of *C. neoformans* are sensitive to 5% CO_2, while clinical isolates are tolerant [4,5]. While many observations have been made about the ability of different fungi to tolerate CO_2 to different degrees, the genetic basis for CO_2 tolerance was unknown.

To identify genes involved in CO_2 tolerance in *C. neoformans*, in chapter 4 of my dissertation I screened gene deletion mutants constructed in a CO_2-tolerant clinical strain. From over 5,000 gene knockout mutants screened, 96 mutants were found to be sensitive to CO_2. I noticed that many of the genes found from this screen were part of known pathways to respond to high temperature. Among these pathways include the Ras1-Cdc24, cell wall integrity (CWI), the regulator of ace2 and morphogenesis (RAM), and calcineurin pathway. I found that overexpression of the terminal kinase of the RAM pathway, Cbk1, was able to restore growth in either high temperature or CO_2 in mutants of the other pathways, indicating the RAM pathway acts downstream to contribute to CO_2 tolerance. I further identified suppressor mutations of the

*cbk1*Δ knockout mutant to further characterize unknown components in this pathway. Two genes were identified in the suppressor screen, *SSD1* and *PSC1*. Based on their protein sequence and homology, I found that both are potential mRNA binding proteins in *C. neoformans* and possibly regulating translation. Characterization of mRNA transcripts bound by these proteins will be further characterized by our lab in the future. An interesting finding from this study is that thermotolerance and CO_2 tolerance are regulated together by the RAM pathway. As *C. neoformans* is an environmental fungus that adapts to host temperatures and CO_2, this result suggests that the RAM pathway is critical for host adaptation. Additionally, the RAM pathway mutants grow as pseudohyphae instead of yeast cells, and suppressor mutations in *SSD1* or *PSC1* partially restore yeast morphology. This reflects the association between CO_2 sensing and morphology which I have described in the previous chapter. Similar to the CO_2 hypersensitivity phenotype observed in Ras1 mutants in *N. Crassa* and *C. albicans*, we also identified Ras1 in our genetic screen for being hypersensitive to CO_2 in *C. neoformans*. This emphasizes the conserved nature of Ras1 in CO_2 signaling. Whether or not the RAM pathway plays a role in CO_2 sensing in other fungi, or if it is specific to *C. neoformans*, has yet to be determined.

While the genetic screen was useful to identify genes and pathways important for CO_2 tolerance, the natural genetic variation that explains CO_2 tolerance in clinical isolates of *Cryptococcus* is unknown. In chapter 5, I utilized quantitative trait loci (QTL) mapping with 374 progeny from a cross between a CO_2-tolerant clinical isolate and a CO_2-sensitive environmental isolate to identify alleles conferring CO_2 tolerance. Backcrossing and bulk segregant analysis coupled with pooled genome sequencing of near isogenic progeny with distinct growth in CO_2 was applied for finer mapping. From my mapping results, I identified many genetic loci contributing to CO_2 tolerance. Even in the near isogenic strains, polymorphisms in over 9 genes

were found to be associated with tolerance. Interestingly, deletion of many of the candidate genes I identified from QTL mapping led to both high temperature and high CO_2 sensitivity. This result is consistent with my findings in chapter 4 that these two phenotypes are linked in *C. neoformans*. Among the candidate genes identified from QTL mapping were two uracil biosynthesis genes. This led me to test multiple uracil biosynthesis gene knockout mutants and find they have similar defects in high temperature and CO_2. Of note, disruption of uracil biosynthesis genes was also found to alter response to CO_2 in *N. crassa* and other microbes as described in the previous chapter. Because CO_2 is a substrate of carbamoyl phosphate synthetase and a precursor for pyrimidine biosynthesis, it is likely that high CO_2 further inhibits pyrimidine biosynthesis, thus interacting synergistically with knockouts of the uracil biosynthesis pathway. Using the murine model of cryptococcosis, I found that differences in CO_2 tolerance between the near isogenic strains is the main factor associated with differences in their virulence. This finding helps to confirm that CO_2 tolerance is indeed a critical virulence factor of *C. neoformans*, which was not recognized previously. Furthermore, I found that sensitive isolates may adapt *in vivo* and become tolerant to increased CO_2 levels. Adaptation to host conditions *in vivo* may offer a possible explanation for CO_2 tolerance observed in clinical isolates and not environmental isolates. It is also possible that some environmental isolates encounter and adapt to high CO_2 concentrations found in nature. In the evolved isolates I sequenced, I found mutations in the QTL on chromosome 10. The candidate gene I identified in this region is CNAG_04570, which encodes for the protein Lhp1. Lhp1 is an RNA binding protein and known downstream effector of Calcineurin. This result is consistent with identifying calcineurin in my genetic screen in chapter 4. The function of Lhp1 is currently unknown. Whether Lhp1 regulates mRNA

transcripts together with Psc1 and Ssd1, regulates different transcripts, or functions in other RNA processing events, are all possible future research questions to address.

References

1. Burges, A. & Fenton, E. The effect of carbon dioxide on the growth of certain soil fungi. *Transactions of the British Mycological Society* **36**, 104-108 (1953).
2. Zadražil, F. Influence of CO2 concentration on the mycelium growth of three pleurotus species. *European journal of applied microbiology and biotechnology* **1**, 327-335 (1975).
3. Paster, N. & Menasherov, M. Inhibition of T-2 toxin production on high-moisture corn kernels by modified atmospheres. *Appl Environ Microbiol* **54**, 540-3 (1988).
4. Litvintseva, A.P. & Mitchell, T.G. Most environmental isolates of *Cryptococcus neoformans* var. *grubii* (serotype A) are not lethal for mice. *Infect Immun* **77**, 3188-95 (2009).
5. Krysan, D.J., Zhai, B., Beattie, S.R., Misel, K.M., Wellington, M. & Lin, X. Host carbon dioxide concentration is an independent stress for *Cryptococcus neoformans* that affects virulence and antifungal susceptibility. *mBio* **10**, e01410-19 (2019).